

# THE PROCEEDINGS OF THE PHYSICAL SOCIETY

---

VOL. 61, PART 4

1 October 1948

No. 346

---

## CONTENTS

	PAGE
Dr. W. H. RAMSEY. On Schwinger's theory of nuclear forces . . . . .	297
Dr. D. E. BUNYAN, Dr. A. LUNDBY, Dr. A. H. WARD and Mr. D. WALKER. The delayed coincidence method in the study of radioactivity, with application to isomerism in $^{181}\text{Ta}$ . . . . .	300
Dr. G. D. ROCHESTER and Dr. C. C. BUTLER. The penetrating particles in cosmic-ray showers: I. Heavily-ionizing particles . . . . .	307
Mr. J. L. PUTMAN. Analysis of spurious counts in Geiger counters . . . . .	312
Dr. G. O. JONES. The mechanism of the reversible thermal after-effects in glass at ordinary temperatures . . . . .	320
Dr. J. D. CRAGGS and Prof. J. M. MEEK. The initiation of low pressure glow discharges. . . . .	327
Mr. A. R. BRYANT. The pressures exerted by an underwater explosion bubble on a circular target plate in a disc-like baffle . . . . .	341
Dr. E. G. RICHARDSON. The impact of a solid on a liquid surface . . . . .	352
Mr. J. E. CAFFYN. A correction in viscometry due to varying hydrostatic head . . . . .	367
Mr. S. K. RUNCORN. The radial variation of the earth's magnetic field. With an appendix by Prof. S. CHAPMAN . . . . .	373
Dr. A. R. STOKES. A numerical Fourier-analysis method for the correction of widths and shapes of lines on x-ray powder photographs . . . . .	382
Letters to the Editor :	
Mr. R. STREET and Mr. J. C. WOOLLEY. A note on the $\Delta E$ effect in alnico . . . . .	391

---

Price to non-members 8s. 4d. net ; 8s. 10d. inclusive of postage  
Annual subscription 63s. inclusive of postage, payable in advance

Published by  
THE PHYSICAL SOCIETY  
1 Lowther Gardens, Prince Consort Road, London S.W.7



## PROCEEDINGS OF THE PHYSICAL SOCIETY

Beginning in January 1948 (Volume 60), the *Proceedings* is now published monthly under the guidance of an Advisory Board.

### ADVISORY BOARD

*Chairman* : The President of the Physical Society (G. I. FINCH, M.B.E., D.Sc., F.R.S.).

E. N. da C. ANDRADE, Ph.D., D.Sc., F.R.S.  
Sir EDWARD APPLETON, G.B.E., K.C.B., D.Sc.,  
F.R.S.

L. F. BATES, Ph.D., D.Sc.

P. M. S. BLACKETT, M.A., F.R.S.

Sir LAWRENCE BRAGG, O.B.E., M.A., Sc.D.,  
D.Sc., F.R.S.

Sir JAMES CHADWICK, D.Sc., Ph.D., F.R.S.

Lord CHERWELL OF OXFORD, M.A., Ph.D.,  
F.R.S.

Sir JOHN COCKCROFT, C.B.E., M.A., Ph.D.,  
F.R.S.

Sir CHARLES DARWIN, K.B.E., M.C., M.A.,  
Sc.D., F.R.S.

N. FEATHER, Ph.D., F.R.S.

D. R. HARTREE, M.A., Ph.D., F.R.S.

N. F. MOTT, M.A., F.R.S.

M. L. OLIPHANT, Ph.D., D.Sc., F.R.S.

F. E. SIMON, C.B.E., M.A., D.Phil., F.R.S.

T. SMITH, M.A., F.R.S.

Sir GEORGE THOMSON, M.A., D.Sc., F.R.S.

Papers for publication in the *Proceedings* should be addressed to the Secretary-Editor, Miss A. C. STICKLAND, Ph.D., at the Office of the Physical Society, 1 Lowther Gardens, Prince Consort Road, London S.W.7. Telephone: KENSington 0048, 0049.

Detailed Instructions to Authors were included in the February issue of the *Proceedings*; separate copies can be obtained from the Secretary-Editor.

*Report of a Conference*

on

## THE STRENGTH OF SOLIDS

held at the

H. H. WILLS PHYSICAL  
LABORATORY, BRISTOL

in July 1947

162 pp. Price 25s., postage and packing 8d.

Orders, with remittances, to  
THE PHYSICAL SOCIETY  
1 Lowther Gardens, Prince Consort Road,  
London S.W.7

*Report of the*

*Gassiot Committee of the Royal Society*

on

## THE EMISSION SPECTRA OF THE NIGHT SKY AND AURORAE

Papers read at an

INTERNATIONAL CONFERENCE  
held in LONDON in JULY 1947

*To be published in the Autumn by*

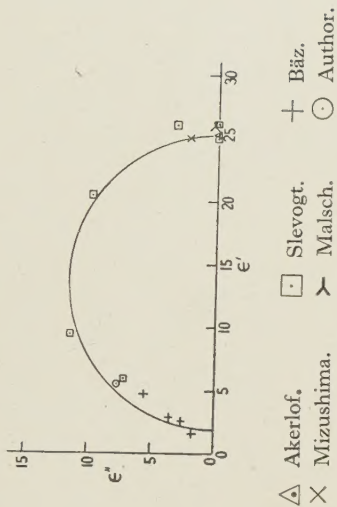
THE PHYSICAL SOCIETY  
1 Lowther Gardens, Prince Consort Road,  
London S.W.7



# CORRIGENDUM

"The Measurement of Dielectric Constant in a Waveguide", by H. C. BOLTON  
(*Proc. Phys. Soc.*, 1948, **61**, 294).

The following figure should have been inserted in the above Letter to the Editor.







**THE UNITED IMPERIAL AND AMERICAN  
PATENT SERVICE**

(Patents, Designs, Trade Mark)

I. E. J. Gheury de Bray, A.M.I.E.E., Registered  
Patent Agent (London), Chartered Electrical  
Engineer and Fellow of the Physical Society.  
J. Wittal, LL.B., Patent Attorney and Counsellor  
at Law (New York).

Booklet free on application.

Preliminary interview free by appointment.  
102 Bishopsgate, E.C.2.

Telephone: Clerkenwell 1131 — Chancery 8579  
London Wall 2121.

Telegraphic Address } IMPERATRIX CENT LONDON.

**REPORTS ON  
PROGRESS IN PHYSICS**

Volume XI (1946-1947)

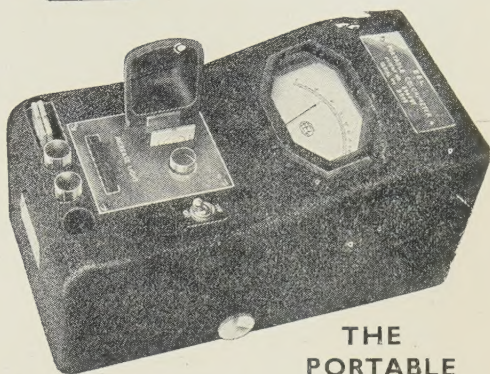
461 pp. Price £2 2s., postage and packing 1s.

Orders, with remittances, to

**THE PHYSICAL SOCIETY**  
1 Lowther Gardens, Prince Consort Road,  
London S.W.7



**PHOTOELECTRIC EQUIPMENT**



**THE  
PORTABLE  
COLORIMETER**

Combines in a robust case the Colorimeter, Microammeter and power supply. This instrument provides a simple photoelectric means of accurately assessing the colour density of a liquid. Any variations can be immediately read on the logarithmic scale of the microammeter. A scientific apparatus with many applications in medicine and chemistry.

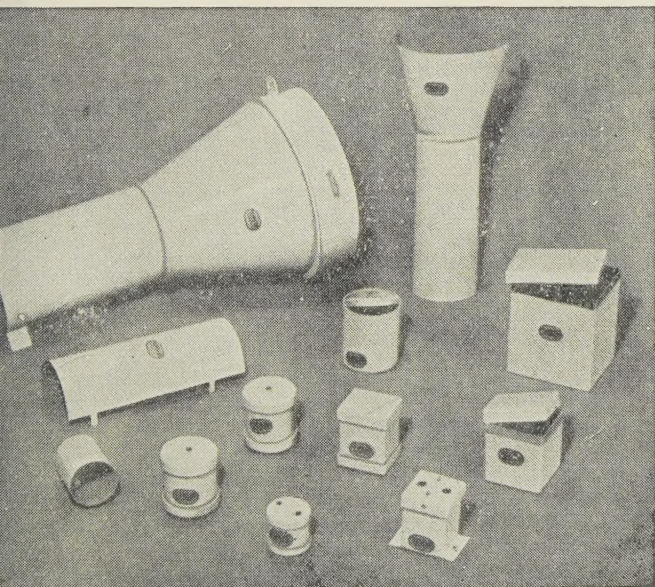
**BATTERY MODEL. Price 26 gns.**

(Complete with accumulator, matched test tubes and filters.)

**A.C. MODEL. Price 30 gns.**

(Incorporating constant voltage transformer.)

**EVANS ELECTROSELENIUM**  
Harlow LTD. Essex



**MUMETAL**  
REGD.

**MAGNETIC SCREENS**

The high permeability of MUMETAL makes it the outstanding material for the production of all types of magnetic screens. We are in a position to fabricate boxes and shields of practically any shape or size for the screening of delicate instruments and equipment from both uni-directional and alternating magnetic fluxes. A complete range of standard MUMETAL shields is available, examples of which are illustrated. Our technical experts will be pleased to assist in the solution of all screening problems. Your enquiries are invited.



**TELCON  
METALS**

**TELEGRAPH CONSTRUCTION & MAINTENANCE CO. LTD.**  
Founded 1864

Office: 22 OLD BROAD ST., LONDON, E.C.2. Tel: LONDON Wall 3141  
Wireless: TELCON WORKS, GREENWICH, S.E.10. Tel: GREENWICH 1040



# Temperature controls production



CONTROLS TEMPERATURE  
PRECISELY AND RELIABLY



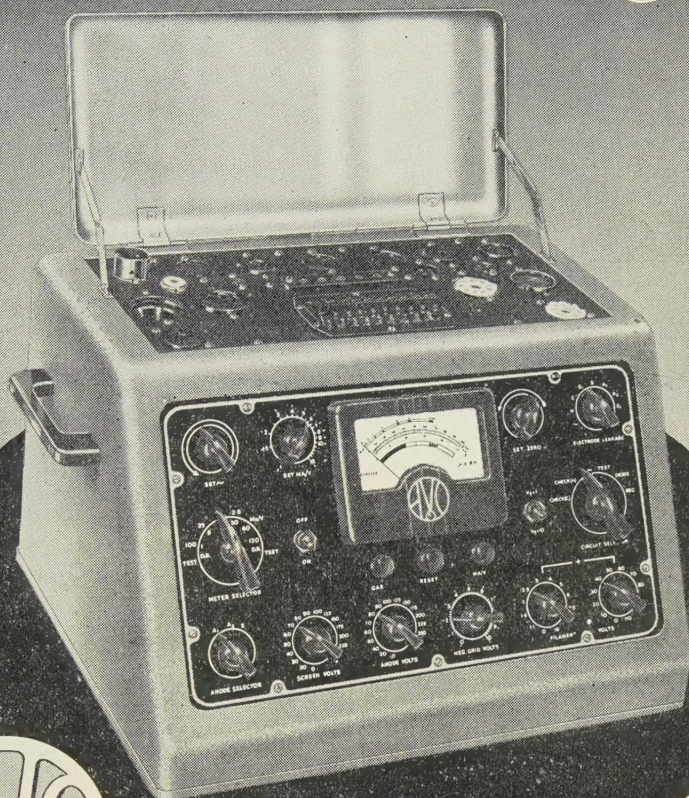
Ask us for appropriate literature

SUNVIC CONTROLS LTD, 10 ESSEX STREET, STRAND, LONDON, W.C.2

Phone: TEMple Bar 7064-8



# *Fine Limits of Accuracy*



## VALVE CHARACTERISTIC METER

A comprehensive instrument built into one compact and convenient case, which will test any standard receiving or small power transmitting valve on any of its normal characteristics under conditions corresponding to any desired set of D.C. electrode voltages. A patented method enables A.C. voltages of suitable magnitude to be used throughout the Tester, thus eliminating the costly regulation problems associated with D.C. testing methods.

A specially developed polarised relay protects the instrument against misuse or incorrect adjustment. This relay also affords a high measure of protection to the valve under test. Successive settings of the Main Selector Switch enable the following to be determined:—

Complete Valve Characteristics, including  $I_a/V_g$ ,  $I_a/V_a$ ,  $I_s/V_g$ ,  $I_s/V_a$ , Amplification Factor, Anode A.C. Resistance, 4 ranges of Mutual Conductance covering mA/V figures up to 25 mA/V at bias values up to  $-100$  V., together with "Good/Bad" comparison test on coloured scale against rated figures.

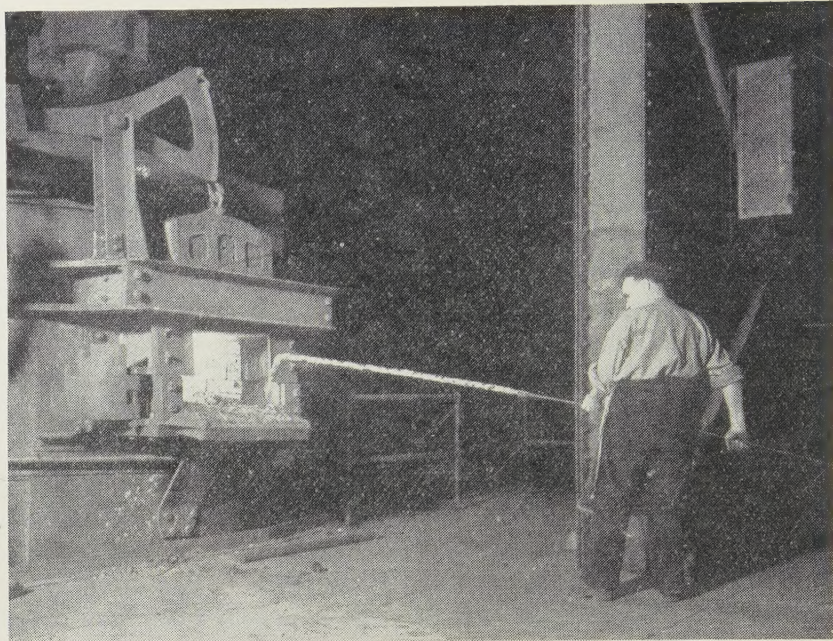
"Gas" test for indicating presence and magnitude for grid current, inter-electrode insulation hot and cold directly indicated in megohms, separate cathode-to-heater insulation with valve hot. Tests Rectifying and Signal Diode Valves under reservoir load conditions, and covers all the heater voltages up to 126 volts.

The AUTOMATIC COIL WINDER & ELECTRICAL EQUIPMENT CO. LTD.  
WINDER HOUSE, DOUGLAS STREET, LONDON, S.W.1. Telephone: VICTORIA 3404-9

*Avo Precision Electrical Testing Instruments*



Inserting a hand-operated  
pyrometer through the  
side door of a 12-ton  
electric arc furnace



# THERMOCOUPLES

*for Reliability and Long  
Life at high temperatures*

The essential requirements of a thermocouple are reproducibility of characteristics from batch to batch and reliability of calibration over a wide range of temperatures.

The success of JMC platinum:rhodium-platinum thermocouples lies in the facts that a maximum deviation from batch to batch of  $\pm 1^\circ \text{C}$ . is guaranteed over the range from 0 to  $1100^\circ \text{C}$ . and that the JMC calibration tables have long been regarded by pyrometer manufacturers and users as accepted standards.

Platinum:rhodium-platinum couples are in use throughout the steel industry as a reliable means of carrying out routine measurements of temperatures of the order of  $1600^\circ \text{C}$ . and over. Other noble metal thermocouples are available for high frequency measuring instruments, research purposes and other special applications.

One of the Specialised Products of

**Johnson**  
**Matthey**



*More comprehensive information on this subject is given in an illustrated booklet available as Publication 1550. This also includes the standard calibration tables and cold junction corrections.*



# THE PROCEEDINGS OF THE PHYSICAL SOCIETY

VOL. 61, PART 4

1 October 1948

No. 346

## On Schwinger's Theory of Nuclear Forces

By W. H. RAMSEY

Turner and Newall Research Fellow, University of Manchester

*MS. received 7 May 1948*

**ABSTRACT.** It is shown that Schwinger's generalization of the Møller-Rosenfeld theory cannot consistently be used to describe nuclear forces. It does not lead to the correct quadrupole moment of the deuteron, and it offers no hope of a detailed agreement with proton-proton scattering.

### § 1. INTRODUCTION

THE symmetrical version of the meson theory of nuclear forces proposed by Møller and Rosenfeld (1940) has been used with some success to calculate the binding energies of the very light nuclei (Frohlich, Huang and Sneddon 1947) and the features of neutron-proton scattering (Ramsey 1947). The meson mass found by the former authors from the energy levels of the hydrogen isotopes is  $210\text{--}220 m_e$ , where  $m_e$  is the mass of the electron; this mass is consistent with the results of neutron-proton scattering and it is in fair agreement with the mass of the commonest cosmic-ray meson. On the other hand, Ramsey (1948) has shown that the empirical data on proton-proton scattering set a lower limit of  $275 m_e$  to the mass of the meson which must be used in this theory. The failure of the theory can be traced to the radial dependence of the interaction. Schwinger (1942) has proposed a generalization of the Møller-Rosenfeld theory which retains the essential characteristics of the simple theory and, at the same time, the interaction has a different radial dependence. The purpose of this note is to examine the possibility of using Schwinger's theory to give a consistent description of nuclear forces.

In Schwinger's theory the static interaction between two nucleons is

$$\mathbf{V}(\mathbf{r}) = \mathbf{V}_v(\mathbf{r}) + \mathbf{V}_{ps}(\mathbf{r}), \quad \dots\dots(1)$$

where  $\mathbf{V}_v(\mathbf{r})$  is the interaction in the symmetrical vector theory

$$\mathbf{V}_v(\mathbf{r}) = (\boldsymbol{\tau}_1, \boldsymbol{\tau}_2) \{ g_1^2 + \frac{2}{3} g_2^2 (\boldsymbol{\sigma}_1, \boldsymbol{\sigma}_2) - (3\lambda^2 r^2)^{-1} g_2^2 \mathbf{S}_{12} (3 + 3\lambda r + \lambda^2 r^2) \} r^{-1} \exp(-\lambda r), \quad \dots\dots(1a)$$

and where  $\mathbf{V}_{ps}(\mathbf{r})$  is the interaction in the symmetrical pseudoscalar theory

$$\mathbf{V}_{ps}(\mathbf{r}) = (\boldsymbol{\tau}_1, \boldsymbol{\tau}_2) \{ \frac{1}{3} f_2^2 (\boldsymbol{\sigma}_1, \boldsymbol{\sigma}_2) + (3\kappa^2 r^2)^{-1} f_2^2 \mathbf{S}_{12} (3 + 3\kappa r + \kappa^2 r^2) \} r^{-1} \exp(-\kappa r). \quad \dots\dots(1b)$$

In these equations  $\mathbf{S}_{12}$  denotes the dipole-dipole operator. In order to suppress the  $r^{-3}$  singularity in (1) Schwinger imposes the subsidiary condition

$$(g_2/\lambda)^2 = (f_2/\kappa)^2. \quad \dots\dots(2)$$

The Møller-Rosenfeld theory appears as the special case in which the masses of the vector and pseudoscalar mesons are equal (that is,  $\lambda = \kappa$ ).



## § 2. PROTON-PROTON SCATTERING

The scattering of protons by protons provides a means of examining the radial dependence of the interaction in the  $^1S$  state; in this configuration the complication of non-central forces does not arise. At low energies the electrostatic repulsion prevents the close approach of the protons so that the anomalous scattering is controlled by the nuclear interaction at large distances. On the other hand, the interaction at small distances is very important in proton-proton scattering at high energies and in neutron-proton scattering. Using the Møller-Rosenfeld potential,

$$V(r) = -Gr^{-1} \exp(-\mu r), \quad \dots\dots(3)$$

Ramsey (1948) found that the empirical data on proton-proton scattering require a meson mass of at least  $275 m_e$ . There is, however, no detailed agreement with experiment for any mass of the meson. The data for energies below 2 Mev. suggest a mass of  $325 m_e$ , whilst the results at higher energies favour a mass of  $270 m_e$ . Thus, when the constants of (3) are adjusted to give a good description of the nuclear interaction at a distance  $r_0$ , the results of proton-proton scattering suggest that the value of  $\mu$  increases with  $r_0$ .

In Schwinger's theory the interaction in the  $^1S$  state is

$$V(r) = -(f_2^2 + 2g_2^2 - g_1^2)\{(1-\alpha)\exp(-\lambda r) + \alpha\exp(-\kappa r)\}r^{-1}, \quad \dots\dots(4)$$

where

$$\alpha = f_2^2 / (f_2^2 + 2g_2^2 - g_1^2).$$

If the constants of (3) are chosen to give a good agreement with (4) in the neighbourhood of  $r_0$ , then

$$\mu = \{(1-\alpha)\lambda \exp(-\lambda r_0) + \alpha\kappa \exp(-\kappa r_0)\} / \{(1-\alpha)\exp(-\lambda r_0) + \alpha\exp(-\kappa r_0)\} \quad \dots\dots(5)$$

and

$$d\mu/dr_0 = -\alpha(1-\alpha)(\lambda-\kappa)^2\{(1-\alpha)\exp(-\lambda r_0) + \alpha\exp(-\kappa r_0)\}^{-2} \exp(-(\lambda+\kappa)r_0).$$

It will be noted that the sign of  $d\mu/dr_0$  depends only on  $\alpha$ ; hence  $\mu$  is a monotonic function of  $r_0$ . The cases  $\alpha=0$  and  $\alpha=1$  are trivial as (3) and (4) become identical. The fact that (4) must be attractive rules out negative values of  $\alpha$ .

§ 3. CASE I:  $0 < \alpha < 1$ 

The range  $0 < \alpha < 1$  corresponds to the case  $2g_2^2 > g_1^2$ . When this condition is fulfilled,  $\mu$  as given by (5) is a continually decreasing function of  $r_0$ . Under these circumstances the interaction (4) may be expected to be less satisfactory than (3) when applied to proton-proton scattering.

Detailed calculations of the properties of the deuteron have been made by Jauch and Hu (1944) on the basis of Schwinger's theory with the subsidiary conditions

$$g_1^2 = 0, \quad \dots\dots(6a)$$

$$\hbar\kappa/c = 177 m_e. \quad \dots\dots(6b)$$

The charge  $f_2$  and the mass of the vector meson were determined from the  $^3S$  and  $^1S$  energy levels; the latter quantity was found to be 60% greater than (6b). The theory can then account for only one-third of the observed quadrupole moment; the ratio  $\lambda/\kappa$  would have to be increased to about 10 to give the empirical value. If  $g_1$  is assumed different from zero, the discrepancy becomes even worse.



As  $\mu = \kappa$  for large values of  $r_0$ , a pseudoscalar meson mass smaller than  $(6b)$  cannot be contemplated; it should, in fact, be increased to the neighbourhood of  $300 m_e$ . This change will exaggerate the disagreement found by Jauch and Hu. It would therefore appear that Schwinger's theory with  $0 < \alpha < 1$  is incapable of accounting for either proton-proton scattering or the properties of the deuteron.

#### § 4. CASE II: $\alpha > 1$

The case  $\alpha > 1$  corresponds to the following restrictions on the charge constants:

$$f_2^2 > g_1^2 - 2g_2^2 > 0. \quad \dots\dots(7)$$

Under these circumstances  $\mu$  is a continually increasing function of  $r_0$ , and a detailed agreement with the results of proton-proton scattering may be obtainable. The possibility that (4) becomes repulsive at large distances must be excluded as this would be at variance with the results of experiments on the scattering of very slow protons by protons; this imposes the further restriction that the mass of the vector meson must be the larger:

$$\lambda > \kappa. \quad \dots\dots(8)$$

As the maximum value of  $\mu$  is equal to  $\kappa$ , the mass of the pseudoscalar meson must be at least  $275 m_e$ .

The magnitude of the interaction constant  $G$  obtained by comparing (3) and (4) increases monotonically with  $r_0$  to the limiting value  $f_2^2$ . In order to account for the values of  $G$  determined empirically,  $f_2^2$  must be at least  $0.25 \hbar c$ . Relations (2) and (7) then set a lower limit to  $g_1^2$ :

$$g_1^2 > 0.5(\lambda/\kappa)^2 \hbar c.$$

These abnormally large charge constants, together with condition (8), prevent the theory from leading to the correct binding energy of the deuteron. The magnitude of  $g_1^2$  also renders the use of the static interaction (1a) unreliable, even as a first approximation.

#### § 5. CONCLUSION

Schwinger's generalization of the Møller-Rosenfeld theory cannot consistently be used to describe nuclear interactions. It does not lead to the correct quadrupole moment of the deuteron, and it offers no hope of a detailed agreement with proton-proton scattering.

#### ACKNOWLEDGMENT

The author would like to express his appreciation to Professor L. Rosenfeld for the interest he has shown in the work.

#### REFERENCES

- FRÖHLICH, H., KUN HUANG, and SNEDDON, I. N., 1947, *Proc. Roy. Soc. A*, **191**, 61.  
 JAUCH, J. M., and NING HU, 1944, *Phys. Rev.*, **65**, 289.  
 MÖLLER, C., and ROSENFELD, L., 1940, *Kgl. Danske Vid. Selsk. mat.-fys. Meddl.*, **17**, No. 8.  
 RAMSEY, W. H., 1947, *Proc. Roy. Soc.*, **191**, 195; 1948, *Ibid.*, in press.  
 SCHWINGER, J., 1942, *Phys. Rev.*, **61**, 387.



# The Delayed Coincidence Method in the Study of Radioactivity, with Application to Isomerism in $^{181}\text{Ta}$

By D. E. BUNYAN, A. LUNDBY, A. H. WARD AND D. WALKER

Physics Department, University of Birmingham

*Communicated by M. L. Oliphant; MS. received 19 February 1948,  
and in amended form 12 May 1948*

**ABSTRACT.** A short-lived nuclear state occurring during a series of radioactive transitions can be studied by the observation of delayed coincidences between the radiations preceding and following the state in question. The method is limited at present to transition periods lying between about  $10^{-7}$  and  $10^{-2}$  seconds. Two distinct experimental procedures are possible, one yielding the differential and the other the integrated decay curve of the short-lived state.

The method has been applied to the decay of the previously reported 22-microsecond metastable state in  $^{181}\text{Ta}$ , which is formed in the decay of the  $\beta$ -ray emitter  $^{181}\text{Hf}$ . It is shown that the isomeric transition takes place in two steps of 0.2 mev. and 0.5 mev. in instantaneous succession. The half-life of the metastable level has been redetermined as  $(20.1 \pm 0.7) \times 10^{-6}$  seconds. From a comparison of the observed and calculated internal conversion coefficients, it seems probable that the 0.2 mev. and 0.5 mev. transitions are of an electric octopole and electric quadrupole character respectively. This would mean that since the spin of the ground state of  $^{181}\text{Ta}$  is  $7/2$ , the 0.5 mev. state must also have a spin of  $7/2$  and the same parity as the ground state, while the metastable state must have a spin of  $1/2$  and opposite parity.

## § 1. INTRODUCTION

WHERE an atomic nucleus undergoes a series of radioactive transitions following rapidly upon one another, coincidence observations on the radiations emitted, using electrical counting techniques, can yield information about the time relationships of the processes involved. An obvious practical restriction is that the initial transition must be of long period.

If one transition follows another within less than about  $10^{-8}$  seconds, it is said to give rise to "instantaneous" coincidences, since experimental coincidence arrangements with the best possible resolution attainable at present\* are unable to indicate any departure from simultaneity. On the other hand, if the second transition follows the first after a mean time interval somewhat greater than  $10^{-8}$  seconds, it is possible to detect that the two radiations emitted are not wholly in coincidence. Where the mean time interval lies between about  $10^{-7}$  and  $10^{-2}$  seconds, it can be measured by delaying or lengthening the electrical pulse recording the first transition so as to bring it into coincidence with that for the second.

The procedure where the first pulse is delayed yields the differential decay curve of the intermediate short-lived state (DeBenedetti and McGowan 1946), while that where the first pulse is lengthened yields the integrated decay

\* using Geiger counters.



curve (Dunworth 1939, Rotblat 1941). The elements of a delayed coincidence recorder are illustrated in figure 1.

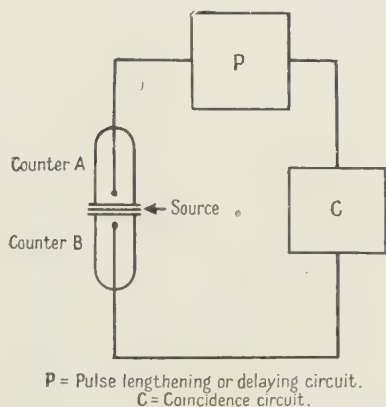


Figure 1. Elements of delayed coincidence recorder.

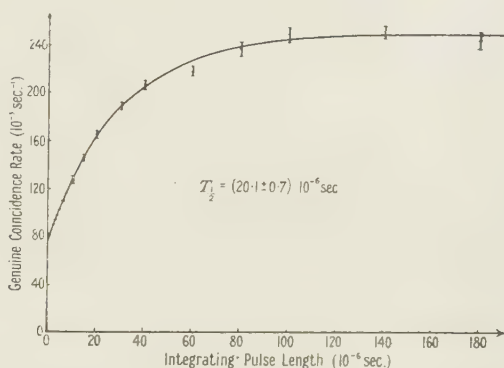


Figure 2. The integrated decay curve of the metastable (upper) level of  $^{181}\text{Ta}$ .

## § 2. COMPARISON OF THE DIFFERENTIAL AND INTEGRAL PROCEDURES

### (i) *Ratio of genuine to random coincidence rates*

Measurements with any coincidence system are limited by the presence of random coincidences. If counters A and B (figure 1) are irradiated by a source placed between them to give individual counting rates of  $N_A$  and  $N_B$  respectively and a genuine coincidence rate  $C_g$ , there will be in addition a background rate of random coincidences given by  $C_r = (N_A - C_g)(N_B - C_g)(\tau_A + \tau_B)$ , where  $\tau_A$  and  $\tau_B$  are the lengths of the pulses reaching the coincidence circuit from channel A and channel B respectively. Since in radioactive experiments  $C_g$  is in general small compared with  $N_A$  or  $N_B$ , we can write, without appreciable error,

$$C_r = N_A N_B (\tau_A + \tau_B). \quad \dots\dots (1)$$

Experimentally one finds  $C_g$  by determining the total coincidence rate, and subtracting  $C_r$ , which is computed from a knowledge of  $N_A$ ,  $N_B$ , and  $(\tau_A + \tau_B)$  using equation (1). It is clearly essential to have  $C_g/C_r$  sufficiently large.

In the integral procedure for delayed coincidences,  $\tau_A$  is increased progressively while plotting the decay curve, and it can be seen that the ratio  $C_g/C_r$  decreases for increasing  $\tau_A$  since  $C_r$  increases linearly with  $\tau_A$ , whereas  $C_g$  increases typically as  $\{1 - \exp(-\lambda\tau_A)\}$ , where  $\lambda$  is the decay constant of the short-lived state. (Any superimposed instantaneous coincidences can be suppressed by the addition of an anti-coincidence circuit.) Similarly in the differential procedure  $C_g/C_r$  decreases for increasing delay  $t_d$  in the A channel, since although  $C_r$  remains constant,  $C_g$  decreases typically as  $\exp(-\lambda t_d)$ . This decrease of  $C_g/C_r$  sets an upper limit of about  $10^{-2}$  seconds to half-lives which can be measured by the integral procedure, as has been pointed out by Rotblat (1941). The upper limit to half-lives measurable with the differential procedure is lower since it may be shown that  $C_g/C_r$  decreases more rapidly with increasing delays than is the case for the integral procedure.



(ii) *Time-scale calibration*

Time calibration in the integral procedure can be carried out simply with random coincidences using equation (1). For this purpose the two counters are irradiated by separate sources to give independent counting rates. Time calibration in the differential procedure requires accurate measurement of the time interval between pulses in the two input channels and is more complicated.

(iii) *Lower limit of measurable half-lives*

With a Geiger counter there is a variable time-lag between the entry of a particle into the counter and the detection of the output voltage pulse. Either delayed coincidence procedure fails when the half-life to be measured is rather smaller than the time-lag fluctuations exhibited by the counters. This sets a lower limit of about  $10^{-7}$  seconds to half-lives which can be measured. With extreme care the method may be pushed to half-lives of a few times  $10^{-8}$  seconds (Bittencourt and Goldhaber 1946), but any further improvement will have to await the development of satisfactory fast-response detectors for use in place of Geiger counters.

## § 3. EXPERIMENTAL DELAYED COINCIDENCE RECORDERS

Two such equipments have been constructed in this laboratory according to the principles shown in figure 1. One, the "differential recorder", employs a pulse-delay network (artificial line) in channel A giving a time delay variable from 0 to  $10 \times 10^{-6}$  seconds in steps of  $0.1 \times 10^{-6}$  seconds. The pulses reaching the coincidence circuit from either channel are fixed in length at  $0.22 \times 10^{-6}$  seconds. The other, the "integral recorder", employs a pulse-lengthening circuit (biased flip-flop) in channel A, giving pulses variable in length from  $10^{-6}$  seconds upwards. The pulse reaching the coincidence circuit from channel B is in this case fixed in length at  $0.7 \times 10^{-6}$  seconds.

During the development of the integral recorder its performance was checked by redetermining the half-life of  $\text{RaC}'$ , counter B in this case being a proportional counter. The value obtained,  $(1.47 \pm 0.07) \times 10^{-4}$  seconds, is in good agreement with previous measurements (Dunworth 1939, Rotblat 1941).

§ 4. EXPERIMENTS ON THE DECAY OF  $^{181}\text{Hf}$ (i) *Previous results*

It has been reported that  $\beta$ -emission by  $^{181}\text{Hf}$  is followed by an isomeric transition in  $^{181}\text{Ta}$ , the half-life of the metastable state being 22 microseconds (DeBenedetti and McGowan 1946). Since, however, these authors did not account for some of the radiations present, it was decided to make a closer study of the disintegration scheme. Madansky and Wiedenbeck (1947) have reported, from intensity measurements based on absorption curves of the total radiation, that there appear to be two  $\gamma$ -rays in cascade.

(ii) *Preparation of the source, and experimental arrangements*

There was available for the investigation a mixture of hafnium oxide and zirconium oxide in the proportion of 7:3 by weight. This was in the form of a fine powder with a primary grain size of  $<10^{-3}$  cm. A sample was irradiated



in the low energy pile at the Atomic Energy Research Establishment, Harwell, to give a specific activity of about 100 microcuries per gram, corresponding to a slow neutron absorption cross-section for  $^{180}\text{Hf}$  of the order of  $10^{-23}\text{ cm}^2$ . Experiments were commenced two weeks after the removal of the sample from the pile. Only one activity was detected, and this decayed over a half-life with a period of  $48.5 \pm 0.5$  days. The half-life of  $^{181}\text{Hf}$  has been given in the literature as 55 days, but Seren, Friedlander and Turkel (1947) give  $46 \pm 3$  days as the result of a recent redetermination.

The source used in the coincidence experiments described below was made by depositing some of the fine powder on one side of an aluminium foil ( $2.3\text{ mg/cm}^2$ ), the mean weight of the powder and adhesive material amounting to about  $1\text{ mg/cm}^2$ . Care was taken to eliminate grain conglomerates as much as possible. The foil was mounted between two end-window  $\beta$ -ray counters 1 cm. apart (figure 1), the source facing counter B ( $7\text{ mg/cm}^2$  window). In the delayed coincidence experiments, counter A had a  $20\text{ mg/cm}^2$  window. Thus the limiting energy of electrons which could enter counter A was about 140 kev. and that for counter B about 75 kev.

In all the measurements described below corrections have been applied to allow for the decay of the source. In the coincidence absorption measurements, back-scattering effects were found to be small.

#### (iii) *Half-life of the metastable level of $^{181}\text{Ta}$*

Figure 2, obtained using the integral recorder, shows the number of genuine coincidences between the particles detected in counter A and the particles detected in counter B as a function of the integrating pulse length. The observed genuine coincidence rate  $C_g$  can be represented by a curve of the form  $C_g = C_{\text{inst}} + C_{\text{max}}(1 - e^{-\lambda\tau})$ , where  $C_{\text{inst}}$  is the instantaneous coincidence rate and  $C_{\text{max}}$  the limiting delayed coincidence rate for increasing pulse length  $\tau$ . The best curve of this form fitting the observations was found by the method of least squares, the value of  $\tau$  corresponding to each observed point being assumed correct. This assumption is justified since, although in our experimental arrangement any individual setting of  $\tau$  is subject to an uncertainty of the order of 2%, such setting errors are random in nature and the coincidence rate for each of the fifteen observed points is the average of not less than four independent settings of the required value of  $\tau$ . The half-life of the metastable level of  $^{181}\text{Ta}$  was found to be  $(20.1 \pm 0.7) \times 10^{-6}$  seconds.

As regards the instantaneous coincidences exhibited in figure 2, it was shown, using the differential recorder, that the transitions involved followed one another within less than  $10^{-7}$  seconds.

#### (iv) *Radiation absorption curves*

*Absorption curve of the radiation preceding the isomeric transition.* While plotting this curve, and the absorption curve of the delayed radiations (see below), we used the integral recorder with the integrating pulse length set at  $30 \times 10^{-6}$  seconds. The instantaneous coincidences were suppressed by the addition of an anti-coincidence circuit of  $10^{-6}$  seconds resolving time.

The absorption curve of the radiation preceding the isomeric transition (A, figure 3) was obtained by putting aluminium foils in front of counter A.



It shows only one component, a  $\beta$ -ray of maximum energy about 0.45 mev. DeBenedetti and McGowan (1946) give the energy of the  $\beta$ -ray as 0.8 mev., which is much higher than can be justified from our results. Madansky and Wiedenbeck (1947), from an absorption curve of the total radiation, give 0.45 mev.

*Absorption curve of the delayed radiations.* The absorption curve of the delayed radiations (B, figure 3) was obtained by putting aluminium foils between the source and counter B. The absorption curve shows the presence of three components: (i) an electron component of maximum range 22 mg/cm<sup>2</sup> corresponding to 130 kev., (ii) an electron component of maximum range 150 mg/cm<sup>2</sup> corresponding to 420 kev., and (iii) a hard component ( $\gamma$ -radiation).

The delayed radiation absorption curve of DeBenedetti and McGowan (1946), as far as it goes, agrees with ours, but it has not been carried far enough

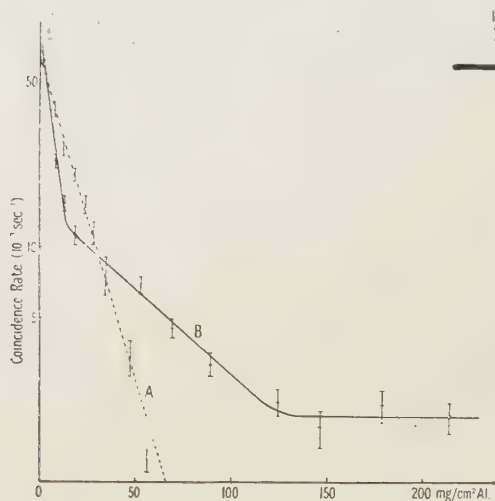


Figure 3.

A: absorption curve of radiation preceding the isomeric transition.

B: absorption curve of delayed radiation.

To obtain the total absorber thickness, the counter-window thickness must be added (20 mg/cm<sup>2</sup> for A and 7 mg/cm<sup>2</sup> for B).

to identify the end point of the harder electron component or to show the presence of the  $\gamma$ -ray component in the delayed radiation. They give an energy of 110 kev. for the softer electron component.

Allowing for the K binding energy of Ta (70 kev.), the electron components found by us correspond to the conversion of  $\gamma$ -rays of 0.2 and 0.5 mev.

*Absorption curve of the radiations in instantaneous coincidence.* An absorption curve of the radiations in instantaneous coincidence was taken with a resolving time of  $0.44 \times 10^{-6}$  seconds. Both counters had 7 mg/cm<sup>2</sup> windows in this case. This absorption curve showed the presence of the same three components as are found in the delayed radiations.

*Absorption curve in lead of the  $\gamma$ -radiation.* An extended  $\gamma$ -ray absorption curve taken on a separate counting set without coincidence and using lead absorbers

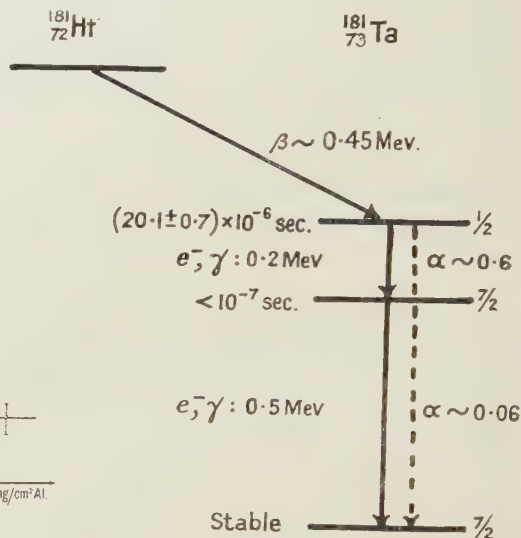


Figure 4. Decay scheme for  $^{181}\text{Hf} \rightarrow ^{181}\text{Ta}$ .



showed the presence of a  $\gamma$ -ray of 0.5 mev., which was also found in the same way by DeBenedetti and McGowan (1946). From similar measurements Madansky and Wiedenbeck (1947) give the energy as 0.52 mev., and also assign an energy of 0.30 mev. to the softer  $\gamma$ -ray.\*

#### § 5. THE DECAY SCHEME FOR $^{181}\text{Hf} \rightarrow ^{181}\text{Ta}$

Consideration of the delayed coincidence and absorption measurements leads to the following conclusions: (i) the emission of a 0.45 mev.  $\beta$ -particle by  $^{181}\text{Hf}$  leads to the 20 microsecond metastable state of  $^{181}\text{Ta}$ ; (ii) the metastable state of  $^{181}\text{Ta}$  decays to the ground state by means of two successive transitions of 0.2 and 0.5 mev. which follow one another within  $10^{-7}$  seconds. The second conclusion follows from the fact that the absorption curves of the delayed radiations and the radiations in instantaneous coincidence show the same components.

This leads to the proposed decay scheme shown in figure 4. No transitions from the metastable state direct to the ground state have been observed, and they cannot amount to more than a few per cent of the two-step transitions.

The internal conversion coefficient  $\alpha$  is defined for each transition as the ratio of the number of conversion electrons to the number of conversion electrons plus  $\gamma$ -rays. The value of  $\alpha$  for the 0.2 mev. transition (0.6) has been estimated from the ratio of the conversion electron and  $\beta$ -ray intensities obtained from a detailed absorption curve of the total radiation emitted by the Hf sample, using a counter with a 2.3 mg/cm<sup>2</sup> window. The value of  $\alpha$  for the 0.5 mev. transition (0.06) has been further estimated from the relative intensities of the two conversion electron components in curve B, figure 3.

The multipole order of the 0.2 mev. and 0.5 mev. transitions, their sequence, and the probable spins of the corresponding states in  $^{181}\text{Ta}$ , have been inferred from the theoretical considerations outlined below.

#### *Theoretical considerations*

Since both the atomic number and the transition energies involved in the decay of the metastable state of  $^{181}\text{Ta}$  are relatively high, the assumptions made in the approximate calculations of internal conversion coefficients, such as those of Hebb and Nelson (1940), are not valid in this case. However, it seems possible to make an order of magnitude estimate of the coefficients involved here from the exact calculations of Taylor and Mott (1932) which are applicable to internal conversion in RaC.

The results of Taylor and Mott are given in terms of the branching ratio  $\alpha/(1-\alpha)$ . For the 0.5 mev. transition we find our observed value of the branching ratio to be 80% greater than that calculated for an electric quadrupole transition. For an electric dipole transition the calculated ratio is four times smaller, and for a magnetic dipole transition three times larger, than the observed value. Considering the experimental uncertainties, including self-absorption, the possibility of ejection of photoelectrons from the source, and the difference in

\* Since the completion of the work described here, Cork, Shreffler and Fowler (*Phys. Rev.*, 1947, **72**, 1209) have reported from the measurement of conversion electron energies in a  $\beta$ -ray spectrograph that  $\gamma$ -rays of energies 133, 345 and 478 kev. are present in the decay of  $^{181}\text{Hf}$ . It is difficult to reconcile these energy values with the results reported here.



atomic number, there seems to be reasonable agreement between the observed value of the branching ratio and the value calculated by Taylor and Mott for electric quadrupole radiation. Thus, although there might be a small admixture of magnetic dipole radiation, the majority of the 0.5 mev. transitions would seem to give rise to electric quadrupole radiation. Since it is known that the lifetime of a state preceding such a transition is about  $10^{-12}$  seconds, the state preceding the 0.5 mev. transition cannot be metastable, but must be the lower excited state of  $^{181}\text{Ta}$ . The spin of the ground state is  $7/2$  and the multipole order of the transition is either 0 or 2. The lower excited level must therefore have the same parity as the ground state and a spin equal to  $7/2$ ,  $5/2$  or  $3/2$  units of  $\hbar$ .

As regards the 0.2 mev. radiation which is emitted in the decay of the 20-microsecond metastable state, an indication of the spin change can be obtained from the rough energy-lifetime relation which has been deduced from the liquid-drop model of the nucleus (Berthelot 1944). Taking into account the correction factor for internal conversion, we find the calculated value for the half-life is of the order of the observed value (the latter is seven times larger) if we assume electric octopole or magnetic quadrupole radiation to be emitted in the transition. The observed value of the branching ratio, 1.5 in this case, is, on the other hand, less than half the value calculated by Fisk and Taylor (1934) for magnetic quadrupole radiation ( $Z=84$ ). Although exact numerical calculations do not exist for electric multipole transitions of order higher than 2, it seems likely, from a rough estimate of the variation in the value of the branching ratio with multipole order, that most of the 0.2 mev. radiation is of an electric octopole nature. The metastable state will then have a parity opposite to that of the lower excited state, while the spins will be  $1/2$  and  $7/2$  respectively.

#### ACKNOWLEDGMENTS

The authors wish to express their appreciation to Professors M. L. Oliphant, F.R.S. and P. B. Moon, F.R.S. for their sustained interest in this work, to Dr. F. E. Whitmore for help with the experimental work, to the Director of the Atomic Energy Research Establishment for the irradiation of the hafnium sample, and to the Superintendent of the Atomic Energy Division at the Telecommunications Research Establishment for help with electronic equipment for this and other work.

#### REFERENCES

- BERTHELOT, A., 1944, *Cahiers de Physique*, No. 19, March.  
 BITTENCOURT, P. T., and GOLDBABER, M., 1946, *Phys. Rev.*, **70**, 780.  
 DEBENEDETTI, S., and MCGOWAN, F. K., 1946, *Phys. Rev.*, **70**, 569.  
 DUNWORTH, J. V., 1939, *Nature, Lond.*, **144**, 152.  
 FISK, J. B., and TAYLOR, H. M., 1934, *Proc. Roy. Soc. A*, **146**, 178.  
 HEBB, M. H., and NELSON, E., 1940, *Phys. Rev.*, **58**, 486.  
 MADANSKY, L., and WIEDENBECK, M. L., 1947, *Phys. Rev.*, **72**, 185.  
 ROTBLAT, J., 1941, *Proc. Roy. Soc. A*, **177**, 260.  
 SEREN, L., FRIEDLANDER, H. N., and TURKEL, S. H., 1947, *Phys. Rev.*, **72**, 888.  
 TAYLOR, H. M., and MOTT, N. F., 1932, *Proc. Roy. Soc. A*, **138**, 665.



# The Penetrating Particles in Cosmic-Ray Showers: I. Heavily-ionizing Particles.

BY G. D. ROCHESTER AND C. C. BUTLER

The Physical Laboratories, University of Manchester

*Communicated by P. M. S. Blackett ; MS. received 7 May 1948*

**ABSTRACT.** It is shown that whilst almost all the heavily-ionizing particles occurring in cosmic-ray showers are protons, a small number are slow mesons. Examples of the local creation of mesons in explosive-type showers are found and are identified as mainly  $\mu$ -mesons. The results are consistent with the recent discovery of Gardner and Lattes that  $\mu$ -mesons may be created directly and are not always the disintegration products of  $\pi$ -mesons as suggested by Marshak and Bethe.

## § 1. INTRODUCTION

AN account is given of an investigation of the heavily-ionizing particles which occur in cosmic-ray showers; five examples of the local creation of mesons in explosive-type showers are found (for a note on one of these showers see Rochester, Butler and Runcorn 1947). The mesons are identified as mainly  $\mu$ -mesons by the measurement of their momenta and the visual estimation of the density of ionization along their tracks; the ionization has been estimated by using the protons as a reference scale.

## § 2. THE EXPERIMENTAL ARRANGEMENT

Two arrangements, designated F and P, figures 1 and 2, were used to trigger the cloud chamber. Neither arrangement was rigidly selective for any particular type

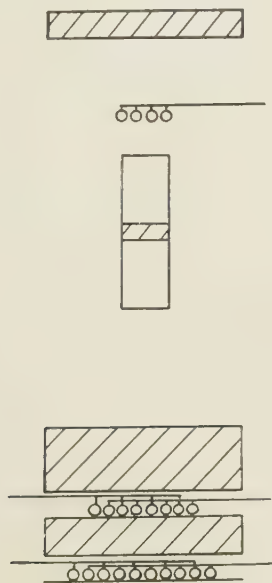


Figure 1. Arrangement F.

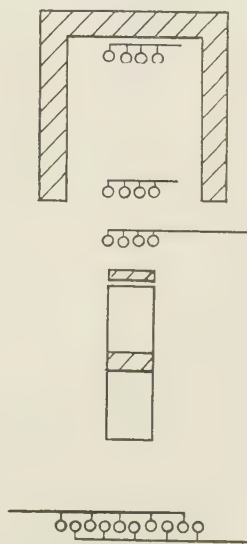


Figure 2. Arrangement P.



of shower, and even though the counters were connected in fivefold coincidence to reduce the rate of random coincidences, the cloud chamber could be set off by a shower consisting of only two particles. All the counters were 2 cm. in diameter; those above the chamber were 30 cm. long and those below 50 cm. long. In order to identify the showers in the cloud chamber associated with extensive air showers a tray of 14 counters connected in parallel, with effective area  $1700 \text{ cm}^2$ , was placed 1 m. from the chamber. An indicator lamp at the cloud chamber showed whether one or more ionizing particles crossed the extension tray within  $2 \mu\text{sec.}$  of the master pulse F or P. This tray was, unfortunately, in operation only during part of the present experiment. The running times and the rates for the different arrangements are shown in table 1. The data given under arrangement P are the combined results from several slightly different arrangements. The rate of associated extensive showers was approximately 2.5 showers per hour.

Table 1

Counter arrangement	Number of photographs	Time (hrs) *	(a)	(b)
F	745	378	41	25
P	4664	830	191	76

\* Corrected for resetting time.

(a) No. of photographs with more than 4 particles in chamber.

(b) " " " " " " " 9 " " "

The cloud chamber was 30 cm. in diameter and 9 cm. in depth. It was filled to a pressure of 1.5 atmosphere with a gas mixture consisting of 80% argon and 20% oxygen. Across the chamber was a lead plate 30.5 mm. thick, faced above and below with 1.8 mm. brass reflecting plates. Photographs were taken at field strengths of approximately 3500 gauss and 7000 gauss using the magnet built by Blackett (1936). Illumination was provided by two Siemens S.F.4 flash discharge tubes each 10 in. long by  $\frac{3}{4}$  in. wide, with a narrow guide tube inside the main tube. Each tube was triggered by a 20-kv. pulse from a magneto coil and flashed by the discharge of a bank of condensers, capacity  $200 \mu\text{F.}$ , charged to 1800 v. The pulse was delayed 0.05 sec. after the chamber expansion in order to allow the drops to increase sufficiently in size to be photographed. The best film was found to be Kodak R55, a moderately fine-grain orthochromatic recording film.

The chamber was photographed by a stereoscopic pair of corrected Taylor, Taylor, Hobson (Cooke) F/2 lenses (used at F/4), of focal lengths 35 mm.

### § 3. MEASUREMENT OF CURVATURE AND ACCURACY OF ENERGY DETERMINATION

Most of the curvatures of the tracks discussed in this paper were determined by direct measurement on a travelling microscope fitted with a Zeiss micrometer eyepiece, but some were measured on the curvature-compensating machine (Blackett 1937). The results for good tracks measured by different observers agree to within 10%. A good track is defined as one which is longer than 6 cm. in the chamber and is free from obvious distortion. A more detailed discussion of the measurement of the curvatures of the tracks of high-energy particles will be given in paper II, but it may be stated here that chamber errors, which are principally due to a gas distortion, limit the maximum detectable momentum in these experiments to  $6 \times 10^9 \text{ ev/c.}$  in a magnetic field of 7500 gauss.

The magnetic field increased by about 5% from the front to the back of the chamber and fell off by about 10% from the centre to the circumference. In most cases the correction for the variation in the field along a track was so small that it was not applied.

The exact positions of the tracks in the chamber and the magnifications were found by reprojecting the photographs through the same lenses. The momenta were derived, where possible, from measurements on both stereoscopic photographs.

#### § 4. SLOW PROTONS

On 42 of the showers 61 heavily-ionizing particles have been observed, and of these 29 have been accurately measured. The ionization density along the track of each has been estimated visually by several independent observers, and the results are plotted in figure 3, following a procedure used by Leprince-Ringuet, Lh  ritier and Richard-Foy (1946). The estimated error in the ionization is taken as the range of the independent estimates.

It has not been found possible to estimate an ionization greater than fifteen times the minimum.

The theoretical ionization curves calculated for masses of  $200 m_e$ ,  $320 m_e$  and  $1837 m_e$  are also shown, and it is at once apparent that the slow particles fall into two main groups, one around the proton curve and the other around the curve for mass  $200 m_e$ . The

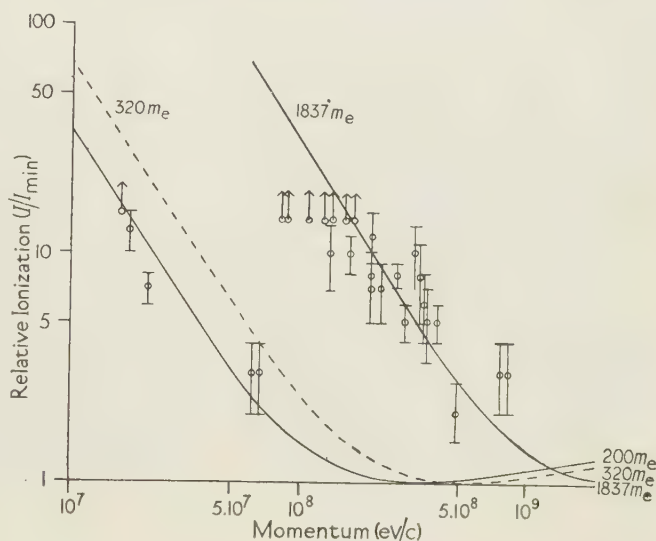


Figure 3.

spectrum of the twenty-four measured protons is given in table 2. The other slow particles which cannot be measured are probably protons of momenta  $10^8$  ev/c. or less. If they are added to the table it would appear that there is a rather rapid decrease in the number of protons with increasing momentum. With one exception all the protons are positive if coming downwards; the exception may well be a positive proton moving upwards.

Table 2. Spectrum of slow protons

Momentum range $\Delta p \times 10^8$ ev/c.	< 1	1-2	2-4	4-6	6-8
Number of protons in range $\Delta p$	2	8	10	2	2

Forty of the protons are associated with explosive-type showers (or "stars") and sixteen with electron-cascade showers. A typical star, in which most of the products of the disintegration have been projected forwards, is shown in the plate, photograph (1), and an example of a more complex shower in photograph (2). In this shower a particle (n) with a momentum of  $4.5 \times 10^8$  ev/c. produces a positive heavily-ionizing particle (p) of momentum  $3.2 \times 10^8$  ev/c. which is



probably a proton. This photograph may be an example of a nuclear explosion induced by a  $\sigma$ -meson, a process already well known from the work of Powell and Occhialini.

## § 5. SLOW MESONS

### (i) *Experimental data*

Data for four of the slow mesons obtained in these experiments are given in table 3 and photographs of these particles are reproduced in the plate, photographs (3), (4), (5) and (6). Data and a photograph of a fifth slow meson (designated meson (7)) have already been published (Rochester, Butler and Runcorn 1947).

Table 3

Photograph number in plate	(3)	(4)	(5)	(6)
Sign	Positive		Negative	Negative
Magnetic field (gauss)	7100	7100	7250	6500
Mean rad. of curvature in plane of chamber (cm.)	25.0	5.8	29.0	9.4
Calc. rad. of curvature due to scattering (a)	280	54	200	106
" " " " " (b)	140	27	100	53
Momentum (ev/c.)	$6.9 \times 10^7$	$1.7 \times 10^7$	$6.3 \times 10^7$	$2.2 \times 10^7$
Kinetic energy (ev.)	$2.4 \times 10^7$	$1.4 \times 10^6$	$2.0 \times 10^7$	$2.4 \times 10^6$
Estimated $I/I_{\min.}$	2.4	>15	2.4	10-15
Calc. $I/I_{\min.}$ : Electron ( $m_e$ )	1.5	1.4	1.3	1.4
Meson ( $100 m_e$ )	1.2	5.6	1.2	3.8
Meson ( $200 m_e$ )	2.1	16.2	2.3	10.9
Meson ( $320 m_e$ )	3.9	32.4	4.5	22.3
(a) Williams (1939)	(b) Bethe (1946).			

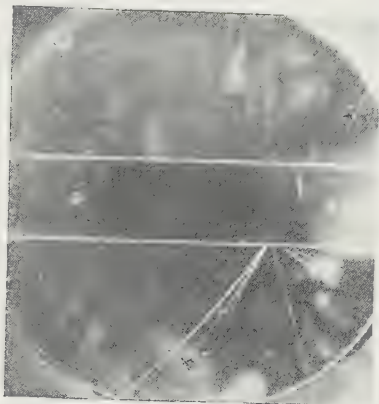
This photograph (taken with arrangement F) was a clear example of the production of a negative meson in an explosive-type shower in the lead plate. Mesons (3), (4) and (5) were all photographed with arrangement P. In the case of meson (6) there was *no* lead above the chamber and the extension was set off by the shower.

Where possible, the sign of the particle has been determined by making a reasonable assumption as to the direction of the particle, and the choice is confirmed in several cases by other evidence. All these slow particles make large angles with the vertical. In three cases, (3), (5) and (7), the mesons arise in nuclear explosions in the lead plate. The explosion associated with meson (3) cannot be seen clearly on the reproduction, for the main part is out of the light at the front of the chamber. It can, however, be seen faintly on the original negative.

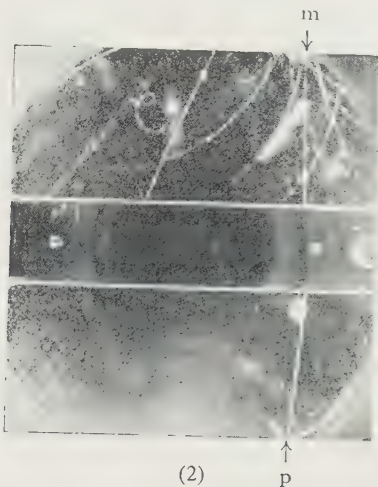
Because of the large magnetic field, the possible error in the radius of curvature of the track due to scattering is relatively small. It has been calculated both from Williams' and from Bethe's formulae, and the results are given in the table.

The estimated ionization is given in line 8, and in line 9 are given the calculated relative ionizations for particles of electronic mass ( $m_e$ ) and masses  $100 m_e$ ,  $200 m_e$  and  $320 m_e$ . It is seen from the table and from figure 3 that in most cases reasonable agreement between estimated and calculated ionizations is obtained by assuming a mass of approximately  $200 m_e$ , although in three of the cases a higher value cannot be excluded.

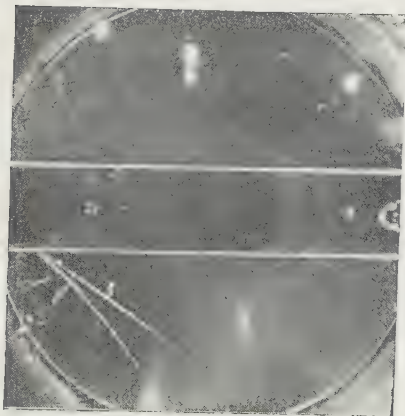
Confirmation is obtained in the case of particle (6) by the knock-on electron indicated by the arrow "k" in the photograph. Another electron, which on the reproduction appears to be a second knock-on electron, is not in the same plane as the meson. The kinetic energy of the knock-on electron estimated from



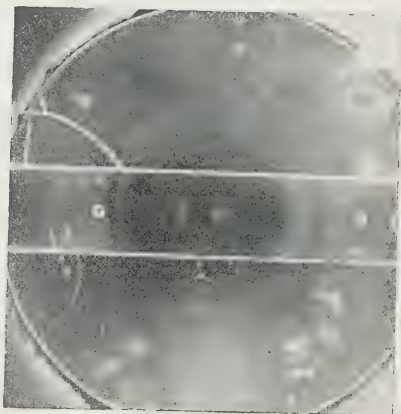
(1)



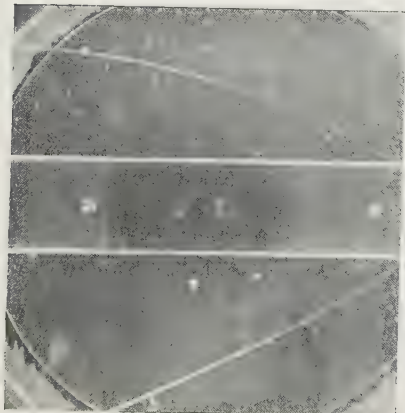
(2)



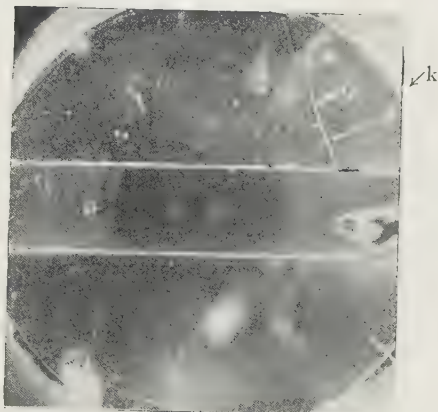
(3)



(4)



(5)



(6)

(See back of plate for description.)



## DESCRIPTION OF PLATE

*Photograph (1).* An example of a typical star created in the lead plate by non-ionizing radiation. All the observed particles are positive and they are identified as protons. The heavily-ionizing particles have kinetic energies of a few mev. and the lightly-ionizing particles kinetic energies of approximately 100 mev. The effects of gas scattering (*not* chamber distortion) can be observed at the ends of two of the proton tracks. One of these particles stops in the chamber.  
 $H=7200$  gauss.

*Photograph (2).* An example of the production of a proton (p) of momentum  $3.2 \times 10^8$  ev/c. by a positive, lightly-ionizing particle (m) of momentum  $4.5 \times 10^8$  ev/c., which is associated with an electron shower.  
 $H=7100$  gauss.

*Photograph (3).* An example of the production of two protons and a positive meson of momentum  $6.9 \times 10^7$  ev/c. in an explosive-type shower which is close to the front of the chamber.  
 $H=7100$  gauss.

*Photograph (4).* A very slow meson of momentum  $1.7 \times 10^7$  ev/c. There is slight electrostatic field doubling at the lead plate.  
 $H=7100$  gauss.

*Photograph (5).* An example of the creation in the lead plate of a negative meson of momentum  $6.3 \times 10^7$  ev/c. and a proton of  $1.3 \times 10^8$  ev/c.  
 $H=7250$  gauss.

*Photograph (6).* A slow meson associated with an extensive air shower. This meson, which is interpreted as a  $\mu$ -meson, has a momentum of  $2.2 \times 10^7$  ev/c. (kinetic energy  $2.4 \times 10^6$  ev.) and is negative if coming downwards. It comes across the chamber out of the piston and may therefore have been created locally. The direction and identification are confirmed by the knock-on electron (k). The other electron, which appears to be a second knock-on, can be seen stereoscopically to cross the meson track towards the front of the chamber.  
 $H=6500$  gauss.

its range is 60 000 ev. (Nuttall and Williams 1926). The calculated energies of knock-on electrons from particles of masses  $200 m_e$ ,  $320 m_e$  and  $1837 m_e$  for "head-on" collisions are 46000 ev., 18000 ev. and 600 ev. Thus a mass of  $200 m_e$  is consistent with the measured value of the energy of the electron although a somewhat lower mass cannot be excluded in view of the fact that the angle between the electron track and the meson track cannot be measured.

### (ii) Discussion

These results have a bearing on the important problem of the creation of the meson. Three of the mesons are observed to be created in the lead plates and in showers of the nuclear-explosive type and not in electron-cascade showers. W. E. Powell (1946) and Fretter and Hazen (1946) also found that slow mesons appeared predominantly in explosive-type showers and is consistent with the recent discovery of the artificial production of mesons by the Berkeley cyclotron (Gardner and Lattes 1948).

The relation of the mesons observed in these photographs to the new types discovered by C. F. Powell, Occhialini and their co-workers will now be discussed. It seems plausible to assume that the Powell  $\mu$ -meson is to be identified with the ordinary cosmic-ray meson found at sea-level and that the mass of the  $\pi$ -meson is approximately  $320 m_e$  (Occhialini and Powell 1948). The evidence of Powell and his co-workers is that these heavy mesons form a large fraction of all slow mesons found at moderately high altitudes and that the  $\pi$ -meson decays into a  $\mu$ -meson with a kinetic energy of 4 mev. Since some of the mesons found in the present experiment seem to have masses of approximately  $200 m_e$ , the following assumptions may be made : (a) the observed mesons are mainly  $\mu$ -mesons created directly in nuclear explosions, (b) the observed mesons are  $\mu$ -mesons arising from the disintegration of  $\pi$ -mesons within the lead plate. If the latter is the correct interpretation, the lifetime must be exceedingly small, certainly less than  $10^{-10}$  sec. Recent evidence from the artificial production of mesons, however, suggests that the lifetime of the  $\pi$ -meson is very much longer than  $10^{-10}$  sec., perhaps of the order of  $10^{-8}$  or  $10^{-9}$  sec. Again, in two of the cases the kinetic energies of the observed mesons are much greater than 4 mev.; thus these particles could not have been created by the disintegration of  $\pi$ -mesons at rest. It would appear therefore that assumption (a) represents the more likely explanation of the present photographs. This result is consistent with preliminary reports from Berkeley which indicate the direct creation of  $\mu$ -mesons.

The meson (6) is of interest because it is connected with an extensive air shower. This meson comes from the piston at the back of the chamber, and it may therefore have been created locally. The photograph was selected from some 500 photographs of extensive air showers, the data for which will be presented in a later paper. The photograph is a clear indication that ordinary cosmic-ray mesons are found in extensive air showers, but it gives no information as to whether such mesons are created locally or come from the air.

### ACKNOWLEDGMENTS

It gives us great pleasure to express our sincere thanks to Professor P. M. S. Blackett, F.R.S., for the excellent facilities which he has given us and for the keen interest he has taken in the investigation. We are also indebted to Dr. S. M. Mitra for help in taking two of the photographs used in this paper.



## REFERENCES

- BETHE, H. A., 1946, *Phys. Rev.*, **70**, 821.  
 BLACKETT, P. M. S., 1936, *Proc. Roy. Soc. A*, **154**, 564; 1937, *Ibid.*, **159**, 1.  
 FRETTER, W. B., and HAZEN, W. E., 1946, *Phys. Rev.*, **70**, 230.  
 GARDNER, E., and LATTES, C. M. G., 1948, *Science*, March 12.  
 LEPRINCÉ-RINGUET, L., LHÉRITIER, C., and RICHARD-FOY, R., 1946, *J. Phys. Radium*, sér. 8, **7**, 69.  
 MARSHAK, R. E., and BETHE, H. A., 1947, *Phys. Rev.*, **72**, 506.  
 NUTTALL, J. M., and WILLIAMS, E. J., 1926, *Phil. Mag.*, ser. 7, **2**, 1109.  
 OCCHIALINI, G. P. S., and POWELL, C. F., 1948, *Nature, Lond.*, **161**, 551.  
 POWELL, W. E., 1946, *Phys. Rev.*, **69**, 385.  
 ROCHESTER, G. D., BUTLER, C. C., and RUNCORN, S. K., 1947, *Nature, Lond.*, **159**, 227.  
 WILLIAMS, E. J., 1939, *Proc. Roy. Soc. A*, **169**, 531.

## Analysis of Spurious Counts in Geiger Counters

BY J. L. PUTMAN

Atomic Energy Research Establishment, Harwell

*Communicated by J. D. Cockcroft; MS. received 25 March 1948*

**ABSTRACT.** A method is described by which the intervals between successive pulses may be divided into size classes. The rate of arrival of intervals whose length is between  $t$  and  $(t + \delta t)$  is measured, where  $t$  is variable and  $\delta t$  is a preset period, small compared with  $t$ .

The method is applied to the study of Geiger counter pulses for argon-alcohol counters. By examining the deviation of the pulse interval distribution from random laws, the number and time distribution of spurious counts is deduced for various potentials applied to the counter. It is found that almost all the spurious counts occur during the recovery period of the counter. They may be eliminated by the use of an external quenching circuit which applies an artificial dead time of the order of 400 microseconds to the counter.

### § 1. INTRODUCTION

WHEN a Geiger counter is used to record the passage of ionizing particles, a number of pulses are delivered by the counter which do not correspond directly to the passage of particles, but which are indistinguishable from the pulses which do correspond to the particles to be counted. These are usually called spurious counts, and an allowance must be made for them in accurate measurements with a Geiger counter.

Spurious counts have been defined by Korff (1946) as those "caused by any agency whatever other than the entity which it is desired to detect, or the normal contamination, or cosmic-ray background". If we accept this definition, we must include as spurious counts those which are caused by any unwanted external agency, such as the impact of visible light on the counter.

In the present paper, we shall confine our attention to those counts which are not caused directly by any external agency, but which are generated inside the counter as a result of earlier discharges.

When a Geiger counter is used with a radioactive source of long half-life, the arrival of ionizing particles in the counter is purely random, and the time spacing between successive particles follows well-known laws (Marsden and Barratt 1911). In particular, the probability of an interval of length between  $t$  and  $(t + \delta t)$  is

$$P(t) = fe^{-ft} \cdot \delta t, \quad \dots\dots (1)$$

where  $f$  is the mean rate of arrival of particles. In the absence of spurious counts, then, we should expect the counter to deliver pulses with a similar time distribution, modified only by the absence of intervals shorter than the dead time of the counter. It is to be expected that any spurious counts, arriving as a result of earlier counts, will not be randomly distributed, but that their times of occurrence will be related systematically to those of the pulses which caused them. Thus the presence of spurious counts gives rise to an excess in the number of intervals of a particular range of lengths. From a comparison of the measured distribution of pulse intervals with that of equation (1), the number of spurious counts can be found, and also the time delays which separate them from the pulses which cause them.

The distribution of time intervals between Geiger counter pulses has already been used as an indication of the time delays of spurious counts, notably by Medicus (1936). Interval selectors have also been designed by Roberts (1940)

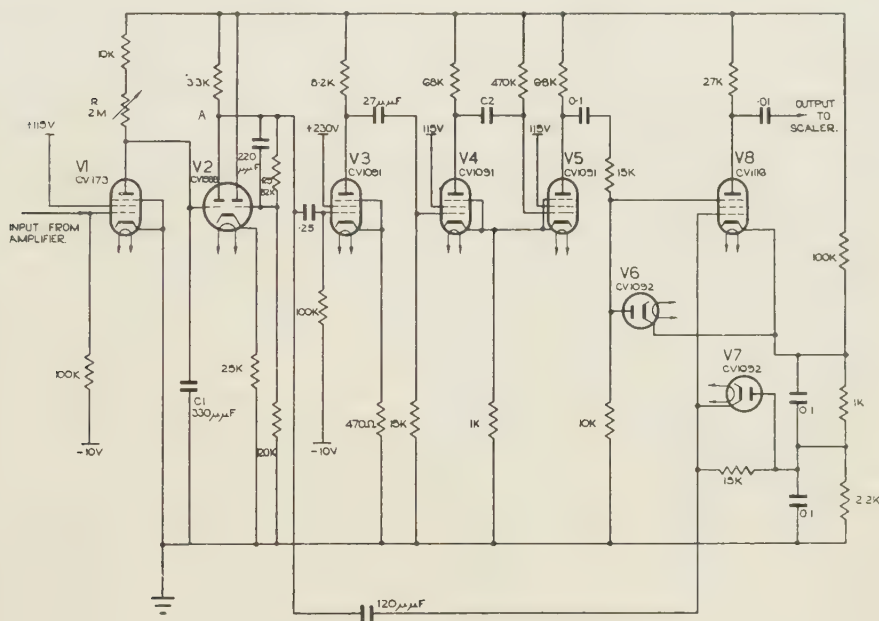


Figure 1. Pulse interval analyser.

and by Driscoll, Hodge and Ruark (1940), which record the arrival of intervals less than  $t$  and greater than  $t$  respectively, where  $t$  is a controllable time interval. These instruments, however, are less applicable to the analysis of spurious counts than one which selects intervals of discrete lengths, as was pointed out by Driscoll, Hodge and Ruark (1940).

Curran and Rae (1947) used a system of delayed coincidences to determine the rate of arrival of pulse-spacings of discrete lengths. It should be noted, however, that the spacings they measure are not necessarily between successive pulses. Consequently the rate of arrival of intervals of a given length, as measured by this method, is a function which depends on the dead-time of the counter and can only be expressed in a simple form when certain approximations are made.

The equipment to be described measures the rate of arrival of pulse intervals between  $t$  and  $(t + \delta t)$ , where  $t$  is variable at will and  $\delta t$  remains constant and is



small compared with  $t$ . With this equipment, the distribution of spacings between successive pulses is analysed. This distribution is directly comparable with equation (1), and the effects of dead-time and of spurious counts upon the random distribution can be shown explicitly.

## § 2. THE PULSE INTERVAL ANALYSER

A simplified form of the circuit used in the pulse interval analyser is shown in figure 1. Pulses from the Geiger counter which is to be examined are fed through an amplifier and limited so that a positive pulse of fixed size and short duration is fed to the grid of  $V_1$  for each pulse delivered by the Geiger counter.

This pulse causes  $V_1$  to conduct and to discharge the condenser  $C_1$ . At the same time the left-hand side of  $V_2$  stops conducting and the potential of the left-hand anode A rises sharply.

The condenser  $C_1$  then recharges through the leak R, and at a time  $t$  after the arrival of the pulse, the left-hand grid of  $V_2$  rises to a conductive level and the potential of A falls sharply to its original level. If a subsequent pulse is delivered by the Geiger counter before the time  $t$  has elapsed,  $C_1$  is again discharged and the recovery process begins again. The potential of the point A cannot fall to its original value until a pulse-free interval  $t$  has elapsed. Figure 2(a), (b) and (c) shows the sequence of events. In figure 2(c) the trailing edge of a square wave at A marks a time  $t$  after the arrival of the last pulse. The leading edge corresponds to the first pulse to arrive after a pulse-free interval  $t$  has elapsed.

The output from A is reversed in phase by  $V_3$ , the output from which is then differentiated and fed to the grid of  $V_4$  (figure 2(d)). Thus a positive pulse, corresponding to the trailing edge of the square wave at A, is used to trigger the flip-flop  $V_4V_5$  which delivers a short positive pulse of length  $\delta t$  to the suppressor  $V_8$  (figure 2(e)).

The suppressor of  $V_8$  is thus raised to a conductive level for the period  $\delta t$  immediately after a pulse-free interval  $t$  has elapsed.

At the same time the output from A is differentiated and applied to the control grid of  $V_8$ , so that the leading edges of the square waves at A give rise to positive pulses (figure 2(f)) which raise the grid of  $V_8$  to a conductive level. If this happens during the period  $\delta t$  in which the suppressor potential is also raised,  $V_8$  conducts and registers an output pulse (figure 2(g)).

Thus an output pulse is only obtained when a pulse occurs in the period between  $t$  and  $(t + \delta t)$  after the previous one, i.e. when a pulse-free interval between  $t$  and  $(t + \delta t)$  occurs. The output pulse is fed to a scaler and recorder unit.

The time  $t$  is adjustable by means of the potentiometer R, and can be set at from 4 to 670  $\mu\text{sec}$ . The short period  $\delta t$  has one of a number of values from 1 to 20  $\mu\text{sec}$ . selected by switching the condenser  $C_2$  in the flip-flop.

We would mention that the pulse interval analyser has a wider application than the study of Geiger counter pulses. It could be used, for example, to determine the random or systematic nature of electronic noise pulses, or for the determination of short radioactive half-lives.

## § 3. PULSE INTERVAL DISTRIBUTIONS

It was found convenient to measure the rate of arrival of periods of given lengths, using the pulse interval analyser, and to compare these with the distribution for random events :

$$r(t) = f^2 e^{-ft} \delta t, \quad \dots\dots(2)$$

which is derivable from equation (1) by multiplying by  $f$ , the mean rate of arrival of particles.

A few counters of different types were used for this analysis. All were of the self-quenching type, being filled with a 9 : 1 mixture of argon and alcohol.

The interval tolerance  $\delta t$  was kept constant at a value of  $8.3 \mu\text{sec.}$  whilst  $t$  was set (in the analyser) at a series of values from  $50$  to  $650 \mu\text{sec.}$  The rate of arrival of pulse intervals was recorded for each setting of  $t$ , to a statistical accuracy of  $3\%$ . This rate was plotted against the lower length  $t$  of the intervals. The total counting rate was also recorded with a rate-of-count meter of an integrating type. The experiments were repeated using a number of applied potentials to each counter.

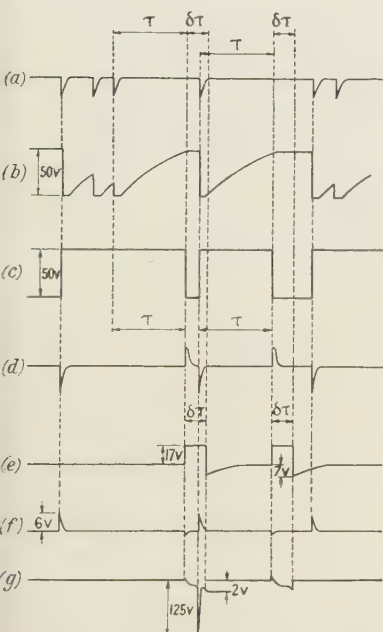


Figure 2.

Waveforms from pulse interval analyser for "Analysis of spurious counts in Geiger counters".

- (a) Geiger counter pulses.
- (b) Anode of V1. (See figure 1)
- (c) Anode A of V2. (See figure 1)
- (d) Control of V4. (See figure 1)
- (e) Suppressor of V8. (See figure 1)
- (f) Control of V8. (See figure 1)
- (g) Output anode of V8. (See figure 1)

Figure 3 shows the distributions of intervals measured for a commercial end-window type beta counter. The rate of arrival of intervals of lengths between  $t$  and  $(t + \delta t)$  is plotted on a logarithmic scale against a linear scale of interval lengths  $t$ .

For the lower applied potentials, the rate of arrival rose steeply with increasing  $t$  to a maximum value, from which it fell exponentially as  $t$  was further increased. The dead time of the counter, which was measured separately, is indicated in figure 3 for two applied potentials. The occurrence of some intervals which were

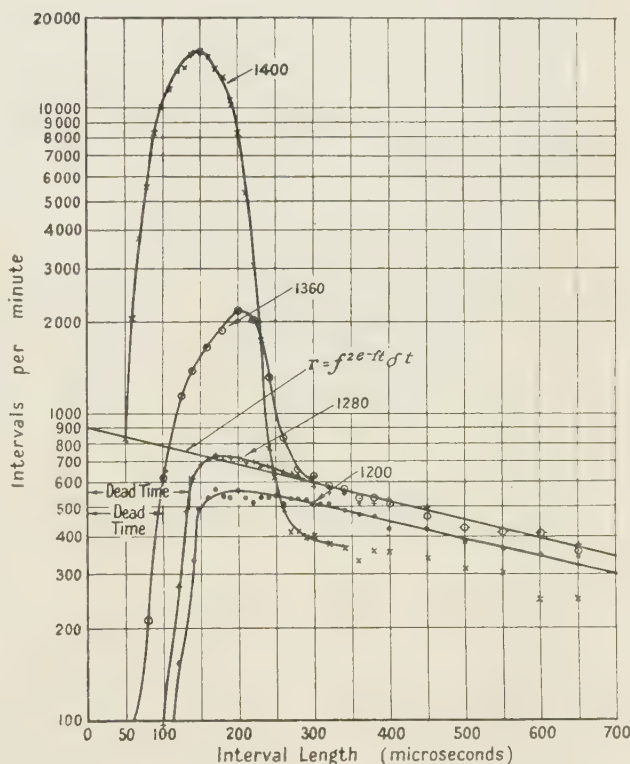


Figure 3. Distribution of intervals between Geiger counter pulses.

Note: The rate of arrival of pulse intervals whose length is between  $t$  and  $(t + \delta t)$  is plotted as a function of  $t$ .  $\delta t = 8.3$  microseconds throughout.



shorter than the normal dead-time corresponds to pulses arriving after the shorter dead-times which followed pulses in a partially recovered counter. (A separate investigation showed that counts occurring during the recovery time were in fact followed by dead-times shorter than normal, a result which was to be expected since the partially recovered pulses are accompanied by space charges smaller than normal.)

Since the interval rate rose to its maximum very shortly after the dead-time, it would appear that very few, if any, counts were lost by recombination of primary electrons with the outward moving positive ions in the space charge.

The exponential fall in the interval rate, as  $t$  was increased, was in conformity with equation (2). Thus for the lower applied potentials the pulse distribution was purely random except where it was limited by the dead-time of the counter. The true distribution of intervals between particles passing through the counter was deduced by extrapolating the distribution from longer intervals back to  $t=0$ . The process is analogous to the dead-time correction normally made in counting experiments. The time  $\delta t$  was also deduced accurately by comparing the intercept on the axis ( $t=0$ ) with the measured total counting rate  $f$ .

For higher applied potentials (see figure 3) a peak appeared in the distribution curve near  $t=200\ \mu\text{sec}$ . Here the rate of arrival of intervals was greater than that to be expected from a random distribution of pulses. Excessive rates were found to extend from the dead-time to the recovery time of the counter. These critical times were measured separately. For values of  $t$  greater than the recovery time the interval rates decreased exponentially as  $t$  was increased, and the interval distribution followed closely that measured at lower operating potentials.

Evidently the additional intervals in excess of the random number corresponded to spurious counts generated internally in the counter on the arrival of positive ions at the cathode. The mechanism has been described by Korff and Present (1944). The increase in the number of spurious counts of this kind accounted very largely for the slope in the plateau of the counter. Good correlation was obtained between the total number of counts, as integrated under the distribution curve, and the total measured counting rate.

A further contribution to plateau slope arose from the slight increase of general level of the random count rates as the applied potential was increased over the lower ranges. This was considered to be due to end effects in the short counter used, which resulted in an increase in the sensitive volume of the counter as the applied potential was raised. The effect disappeared when a long thin counter was used, so that end effects became negligible. When the long counter was used, the distribution of pulse intervals became independent of applied potential for values of  $t$  greater than the recovery time for the counter, i.e. all the distribution curves coincided for the higher values of  $t$ .

At very high potentials, the general level of random intervals fell below the normal level because of the increased loss in dead times associated with the large number of spurious counts. This is shown in the curve for 1400 volts in figure 3. The counter was then operating well above the plateau level, a condition not likely to be met in practice.

#### § 4. SUPPRESSION OF SPURIOUS COUNTS

Since all the spurious counts observed in the above experiments occurred within the recovery time, it was decided to render the counter inoperative after

each count for a period slightly greater than the recovery time, in order to examine the flattening of the plateau produced by this means.

This was achieved by the use of an improved form of Gettings's (1938) quenching circuit designed by Cooke-Yarborough. This constituted a flip-flop which was triggered by incoming pulses and which caused the potential applied to the counter to fall by some 270 volts for a period of the order of  $400\ \mu\text{sec.}$  and then to revert quickly to its normal level. Thus any electrons produced in the counter during the  $400\ \mu\text{sec.}$  period would find the counter reduced in amplification factor below the Geiger-Müller region and would produce pulses too small to be recorded. An artificial dead-time was thus applied to the counter.

When the choice of the applied dead-time was made, an allowance was made for the increase in recovery time due to the reduced potential.

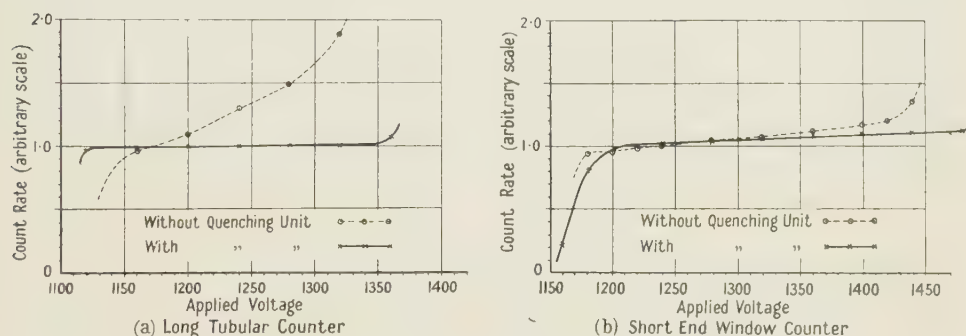


Figure 4. Effects of quenching circuit on the plateau.

The results of applying the quenching circuit are shown in figures 4(a) and 4(b) which are for long and short counters respectively. It can be seen that, with the long counter, an initially rather bad plateau became perfectly flat when the quenching circuit was used. This shows that the initial slope was almost entirely due to spurious counts. Great improvement in plateau slope was also obtained with the short counter, but a small residual slope persisted, which could be attributed to the end effects mentioned above.

The use of a quenching circuit of this kind with a self-quenched counter to remove spurious counts has a practical significance where accurate counting is required. It was found to be of particular value in eliminating variations of counting rate with temperature, which were traced to a bodily shifting of the plateau towards high operating potentials as the temperature was increased. When the plateau was flattened with an external quenching circuit of the form just described, the counting rate became largely independent of temperature.

## § 5. DISCUSSION OF RESULTS

The position of the peak in the distribution curve of figure 3 indicates very strongly that the spurious counts were mainly due to secondary electrons liberated from the cathode on the arrival of positive ions. This explanation is strengthened by the limitation of the intervals preceding spurious counts to a period equal to the recovery time of the counter.

Another possible source of spurious counts lies in the formation of negative ions, as, for example, when electrons are captured by neutral oxygen atoms (Rose and Ramsey 1941, Montgomery and Montgomery 1941a). These heavy ions



move much more slowly towards the anode of the counter than do free electrons in the avalanche process. The captured electrons are released in the high fields near the anode wire of the counter and give rise to delayed spurious counts. The time delays involved are of the same order as those for spurious counts caused by cathode secondaries. The presence of a large number of spurious counts due to electron capture, as well as those due to cathode secondaries, would be expected to cause a double maximum in the distribution curve for pulse intervals. One counter which was suspected of having an air leak was tested and some indication of a double maximum was found. The results, however, were inconclusive.

The spurious counts shown in figure 3 are distributed over a wide range of pulse intervals  $t$  from the dead-time to the recovery time of the counter. This result indicates that positive ions are arriving in large numbers at the cathode throughout this period. The positive space charge is therefore quite diffuse by the time it reaches the cathode and not concentrated in a thin shell as has been assumed (Montgomery and Montgomery 1941 b, Stever 1942). The result is not surprising, since the forces of mutual repulsion acting on such a shell would be of the same order as the applied fields in the counter, so that spreading would take place as the space charge moved outwards towards the cathode.

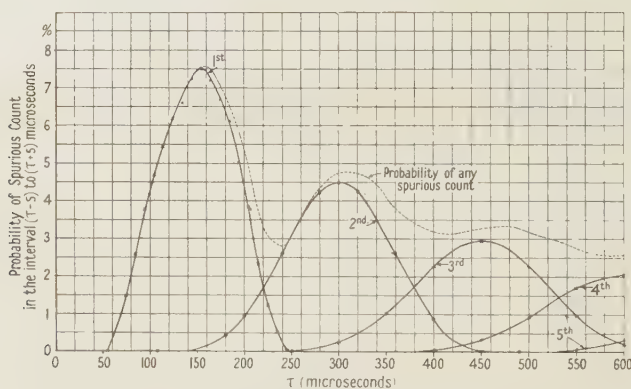


Figure 5. Spurious counts of higher orders.  
(Deduced from distribution of figure 3 for 1400 volts.)

These results, which were obtained in 1946\*, are in good agreement with subsequent measurements by Curran and Rae (1947) using a different method.

It should be noted that a spurious count is almost as likely to produce a further spurious count as is a true count. A second spurious count would be related to the first by a time delay of the same magnitude as though it followed a true count. Hence in figure 3 the excess rates recorded correspond to spurious counts of the first, second, third order, and so on.

If the probability of a count being followed by a spurious count is  $P_1$ , then if the true count rate is  $f$ , the rate of arrival of first spurious count is  $S_1 = fP_1$ . Now, if spurious counts are assumed for simplicity to have the same chance as true counts of being followed by spurious counts, then the rate of arrival of second spurious counts is  $S_2 = S_1P_1 = fP_1^2$ , and proceeding thus, the rate of arrival of  $n$ th spurious

\* The Pulse Interval Analyser described in § 2 was used to demonstrate these results at the Physical Society Exhibition of Scientific Instruments and Apparatus, April 1947.

counts is  $S_n = fp_1^n$ . Thus, if  $p$  is the total probability of a spurious count, we have  $p = \sum_{n=1}^{\infty} p_1^n = p_1/(1 - p_1)$ , so that the total spurious count rate is  $s = fp = fp_1/(1 - p_1)$ .

Using this relation, the distributions of spurious counts up to the 5th order was deduced from the curve for 1400 volts in figure 3. These distributions are shown in figure 5. A curve is superimposed which shows the total probability of occurrence of a spurious count at a given time after a true count.

The assumption of equal probability for all spurious counts is not strictly justified, since those spurious counts which occur after the dead-time are associated with smaller space charges than normal and consequently have a reduced chance of producing a further spurious count. However, the method of assessing the distribution of figure 5 is probably justified as a first approximation.

It is certainly true that when the number of spurious counts becomes large, the probability of higher order counts becomes appreciable. For this reason a quenching circuit of the form described in §4 is to be preferred to an artificial paralysis in the recording circuits as a method of removing spurious counts. The quenching circuit eliminates all the spurious counts by preventing the occurrence of those of the first order. The paralysis method rejects the first-order spurious counts but allows those of higher order to be recorded.

#### § 6. CONCLUSIONS

We conclude that the major cause of plateau slope in argon-alcohol filled counters is the occurrence of spurious counts during the recovery period. These are almost certainly due to secondary electrons liberated by positive ions arriving at the cathode of the counter. By the use of an external quenching circuit which applies an artificial dead-time greater than the recovery time of the counter, very flat plateaux can be obtained, especially for long thin counters.

#### ACKNOWLEDGMENTS

The author wishes to thank Mr. E. H. Cooke-Yarborough of A.E.R.E. for his interest in the work and for his help in the design of electronic circuits. The work was a part of the research programme of A.E.R.E. Harwell and the results were published as an official memorandum in February 1947. Acknowledgment is made to the Director, A.E.R.E. and the Ministry of Supply for permission to publish this paper.

#### REFERENCES

- CURRAN, S. C., and RAE, E. R., 1947, *Rev. Sci. Instrum.*, **18**, 871.  
 DRISCOLL, R. L., HODGE, M. W., and RUARK, A., 1940, *Rev. Sci. Instrum.*, **11**, 241.  
 GETTING, I. A., 1938, *Phys. Rev.*, **53**, 103.  
 KORFF, S. A., 1946, *Electron and Nuclear Counters* (New York: Van Nostrand), p. 16.  
 KORFF, S. A., and PRESENT, R. D., 1944, *Phys. Rev.*, **65**, 274.  
 MARSDEN, E., and BARRATT, T., 1911, *Proc. Phys. Soc.*, **23**, 367.  
 MEDICUS, A., 1936, *Z. Phys.*, **103**, 76.  
 MONTGOMERY, C. G., and MONTGOMERY, D. D., 1941 a, *Phys. Rev.*, **59**, 1045; 1941 b, *J. Franklin Inst.*, **231**, 509.  
 ROBERTS, A., 1940, *Phys. Rev.*, **57**, 564.  
 ROSE, M. E., and RAMSEY, W. E., 1941, *Phys. Rev.*, **59**, 691.  
 STEVER, H. G., 1942, *Phys. Rev.*, **61**, 38.



## The Mechanism of the Reversible Thermal After-effects in Glass at Ordinary Temperatures

By G. O. JONES

The Clarendon Laboratory, Oxford

*MS. received 6 February 1948*

**ABSTRACT.** An explanation is suggested for the reversible thermal after-effects shown by glass, which are responsible for the zero-depression in mercury-in-glass thermometers. A rough relation is established between these effects and the delayed elastic effects shown under ordinary mechanical stress. It is assumed that the thermal after-effects are delayed elastic strains resulting from stresses between regions of slightly differing composition, the origin of the stresses being the differing contractions of these regions during cooling from the annealing temperature. The model offers explanations for some detailed features of the behaviour, requiring inhomogeneities corresponding to differences of only a few per cent in the proportions of the main constituents to account for the observed effects.

### § 1. INTRODUCTION

IT was shown by Weidmann that there was a connection between the delayed elastic effects (or elastic after-effects) and the thermal after-effects in glasses at room temperature, a glass which was "good elastically", that is, having a small after-effect, being also "good thermally". As far as is known to the writer, no closer connection than this has been established, and the actual mechanism of the reversible thermal after-effects is still unexplained. They must be connected with an interchange of energy between different parts of the structure, and it is this which makes the phenomena of interest as it implies a degree of atomic or group mobility. Three main types of atomic movements have to be considered, namely, those corresponding to the very gradual contraction of the structure as a whole towards the equilibrium supercooled liquid condition (often known as "stabilization"), those corresponding to viscous flow under the action of external or "frozen-in" mechanical stresses, and those corresponding to delayed elastic strains and recoveries. At ordinary temperatures only the latter movements have relatively short equilibrium or relaxation times, so it is reasonable to look to them for the explanation of the thermal after-effects.

This paper suggests a possible phenomenological relationship between the thermal and mechanical after-effects which, since the mechanical after-effects are familiar and relatively well understood, we can regard as an explanation of the thermal after-effects.

It should be mentioned that some of the earlier workers (e.g. Crafts 1882) suggested explanations in terms of the relaxation of "strains" in the glass, in general without specifying what type of "strain" was being considered or accounting for their presence. With the data then available it would not have been possible to estimate what degree of mobility could be expected in the glass.

### § 2. THE THERMAL AND ELASTIC AFTER-EFFECTS

The thermal after-effects under consideration are the reversible effects which are responsible for the temporary zero-depression in a mercury-in-glass thermometer rapidly cooled to the ice-point, and for the slowness of the approach to an

equilibrium reading when rapidly heated to a higher temperature. In both cases the effect is entirely due to the glass, which when heated or cooled does not immediately reach its new volume. The larger part of the total change in volume occurs instantaneously, but the last small fraction of the change occurs only slowly, with an equilibrium time of minutes, hours or days according to circumstances. In all reported cases the instantaneous and the delayed change in volume appear to have the same sign. The expansion of the mercury is wholly instantaneous, however, so that when rapidly cooled to  $0^{\circ}$  the mercury level passes the  $0^{\circ}$  reading and slowly rises to it; when rapidly heated to a higher temperature the mercury again passes the equilibrium reading and slowly (but not as slowly as in the former case) falls back to it. The magnitude of the delayed effect at any temperature reaches a maximum if the glass has been held at the other temperature for a long period, and this maximum is greater for large temperature differences. It will be convenient to mention here that a "depression constant" is defined for mercury-in-glass thermometers as the immediate apparent depression of the zero which occurs when the thermometer is rapidly cooled to  $0^{\circ}$  after being maintained for a long period at  $100^{\circ}$ . It varies between  $0.01^{\circ}$  and  $1^{\circ}$  for different glasses and is generally in the region of  $0.05^{\circ}$ . More detailed accounts of the effect have been given by Dickinson (1906) and by Guillaume (1889).

These short-term reversible effects are quite distinguishable from the very gradual "secular rise" in the zero which also occurs over a period of years as a result of the slow contraction of the glass towards a final volume.

The delayed elastic effects consist of a somewhat analogous slowly developing elastic strain additional to the instantaneous elastic strain which occurs on application of a mechanical stress. On removal of the stress both parts of the strain are recovered, the delayed part again being recovered only slowly with an equilibrium time of minutes or hours which does not apparently vary significantly with temperature. The total magnitudes of these effects, defined as the ratio  $R$  of the delayed strain to the instantaneous strain for a given stress, vary between 0.1% and 3% for different glasses at room temperature, and increase with increasing temperature. If sufficient time is not allowed for the full development of the delayed strain under load, the delayed recovery is correspondingly reduced. The mechanisms of these effects are fairly well understood; they can occur, for instance, in structures where regions of true solid matter enclose true liquid regions, and they probably occur in all liquids, including glass, in which regions of different relaxation times or viscosity occur in conjunction. In structures of the latter type true irreversible viscous flow also occurs under stress, but the viscosity is so high in the case of glass that we need not consider this in the explanation of these short-term effects. A fuller account of the delayed elastic effects has been given by the author elsewhere (Jones 1944).

### § 3. RELATION BETWEEN THE TWO TYPES OF AFTER-EFFECT

The basis for the establishment of a relation between the two kinds of after-effect is the assumption that the slow changes in volume represent the net result of a number of delayed elastic strains of differing magnitudes which occur in adjacent regions of the glass at different temperatures. The stresses which give rise to these delayed strains are the result of the differing degrees of contraction of these regions during cooling from the transformation or annealing



region. (We are not concerned with the temporary stresses which are introduced as a result of temperature gradients in the glass during rapid heating or cooling in the working range. Some authors (see for instance Hovestadt 1902) have considered that these temporary stresses might be responsible for the thermal after-effects, but Young (1890) and others have shown this to be incorrect.)

We consider an idealized structure in which the glass is equally divided into uniformly distributed small regions of two types, the physical properties within one type being uniform. Adjacent small regions are assumed to be in full mechanical and cohesive touch with each other. The "instantaneous" coefficients of linear expansion  $\alpha$ , the magnitudes of the ratio  $R$  (as already defined), and the variation of this quantity with temperature are, however, assumed to differ for the two types.

We need not consider the variation with temperature of the instantaneous coefficient of expansion, nor of the instantaneous value of Young's modulus  $Y$ , assumed the same for both types of region. Employing appropriate superscripts to denote the values of  $R$  at temperatures  $T$  and  $T'$ , and subscripts 1 and 2 to denote the two types of region, the following quantities are defined:  $\alpha_1, \alpha_2, R_1, R_2, R'_1, R'_2$ .

For convenience we consider a system in one dimension, and the elementary model can then consist of two thin strips of glass of types 1 and 2 of unit length, stuck together along their lengths, or simply clamped together at their ends. This clamping must be imagined performed at the lowest temperature  $T_g^*$  at which ordinary mechanical stresses can be relaxed quickly in either of the two glasses, and the combination then cooled suddenly to the temperature  $T$  with no development of delayed strains of magnitudes corresponding to any intermediate temperature. (As already stated, we do not consider effects due to temporary temperature gradients. Neither need we consider the bending that would occur if such a single elementary model were cooled on its own.)

Now if  $-\Delta$  is the instantaneous contraction when cooled from  $T_g$  to  $T$ , there will be compression stresses in 1 and 2 of  $Y\{-\Delta - \alpha_1(T_g - T)\}$  and  $Y\{-\Delta - \alpha_2(T_g - T)\}$  respectively. Since the actual stresses must be equal and opposite, we have  $Y\{-2\Delta - (\alpha_1 + \alpha_2)(T_g - T)\} = 0$ , so that

$$-\Delta = (\alpha_1 + \alpha_2)(T_g - T)/2. \quad \dots\dots(1)$$

The delayed elastic effects may be most conveniently considered by defining "final" values of Young's modulus as  $Y/(1 + R_1)$  and  $Y/(1 + R_2)$  for the two glasses at temperature  $T$ .

Then if  $-\delta\Delta$  is the additional delayed contraction we find, by a similar argument,

$$-(\Delta + \delta\Delta) = (\alpha_1 + \alpha_2 + \alpha_1 R_2 + \alpha_2 R_1)(T_g - T)/(2 + R_1 + R_2). \quad \dots\dots(2)$$

Subtracting and rearranging, equations (1) and (2) lead to

$$\delta\Delta = (\alpha_1 - \alpha_2)(R_1 - R_2)(T_g - T)/2(2 + R_1 + R_2). \quad \dots\dots(3)$$

If  $-\Delta'$  and  $-(\Delta' + \delta\Delta')$  are the instantaneous and delayed contractions corresponding to a rapid cooling from  $T_g$  to  $T'$ , we have by a similar argument

$$-\Delta' = (\alpha_1 + \alpha_2)(T_g - T')/2, \quad \dots\dots(4)$$

$$\text{and} \quad \delta\Delta' = (\alpha_1 - \alpha_2)(R'_1 - R'_2)(T_g - T')/2(2 + R'_1 + R'_2). \quad \dots\dots(5)$$

\*  $T_g$  is of course the conventional symbol for the transformation temperature, which is the temperature at which the equilibrium times for the relaxation of mechanical stresses under constant strain are of the order of seconds or minutes.

It is reasonable to suppose that in a rapid change from equilibrium at  $T$  to the temperature  $T'$ , the instantaneous and delayed expansions are given by  $(\Delta' - \Delta)$  and  $(\delta\Delta' - \delta\Delta)$  respectively. Defining instantaneous and final expansion coefficients  $\bar{\alpha}$  and  $(\bar{\alpha} + \delta\bar{\alpha})$  for the combination, we have  $\bar{\alpha}(T' - T) = \Delta' - \Delta$  and  $\delta\bar{\alpha}(T' - T) = \delta\Delta' - \delta\Delta$ .

Evaluating these, we find from equations (1), (3), (4) and (5),

$$\bar{\alpha} = (\alpha_1 + \alpha_2)/2, \quad \dots\dots(6)$$

and (neglecting second powers of  $R$  in the numerator and first powers in the denominator)

$$\frac{\delta\bar{\alpha}}{\bar{\alpha}} = \frac{(\alpha_1 - \alpha_2)[(T_g - T')(R'_1 - R'_2) - (T_g - T)(R_1 - R_2)]}{2(\alpha_1 + \alpha_2)(T' - T)}. \quad \dots\dots(7)$$

It is also convenient to express this in another form, by multiplying out and refactorizing:

$$\frac{\delta\bar{\alpha}}{\bar{\alpha}} = \frac{(\alpha_1 - \alpha_2)[(T_g - T)(R'_1 - R'_2) - (T_g - T')(R_1 - R_2) - (T' - T)(R_1 - R_2 + R'_1 - R'_2)]}{2(\alpha_1 + \alpha_2)(T' - T)}. \quad \dots\dots(8)$$

We can now see under what conditions a thermal after-effect of the ordinary sign, that is, one for which  $\delta\bar{\alpha}/\alpha > 0$  is to be expected.

If we consider two glasses of differing composition, and take the case  $T' > T$ , then since  $R$  increases with temperature we have  $R'_1 > R_1$  and  $R'_2 > R_2$ . Also if  $\alpha_1 > \alpha_2$  it is usually the case that  $R_1 > R_2$  and  $R'_1 \gg R'_2$  (the sign  $\gg$  is here used to denote a greater, though not necessarily very great, inequality). The correctness of the signs of these inequalities can be checked by considering pure silica as glass 2, when  $\alpha_2$ ,  $R_2$  and  $R'_2$  would be very small.

In normal use, also,  $T_g \gg T$  and  $T_g \gg T'$ . The sign of  $\delta\bar{\alpha}/\alpha$  is the same as the sign of the quantity inside square brackets in equations (7) and (8), and it can now be seen at once from equation (7) that this is positive.

By considering equation (8) we can see that there are in fact two effects acting in opposite directions. The first two products within the square brackets may be regarded as representing the fact that at the average stress acting between  $T$  and  $T'$ , the delayed elasticity of glass 1 preponderates increasingly as the temperature is raised. The difference between these products as written is always positive, and this is actually the main effect. The third product within the square brackets is also always positive and as it is prefaced by a minus sign, it represents a tendency towards a thermal after-effect in the reverse direction, which is due to the fact that when the combination is heated the stresses present are actually reduced. However, since  $(T - T') \ll T_g$  this effect is relatively small; if the effect of increasing  $R_1$  over-rides this reduction we have an after-effect of the usual sign.

#### §4. ESTIMATE OF THE DEPRESSION CONSTANT OF A MERCURY-IN-GLASS THERMOMETER

It may easily be shown that the depression constant  $k$  of a mercury-in-glass thermometer, as already defined, is given by

$$k = 300 \delta\bar{\alpha}/(\beta - 3\bar{\alpha}), \quad \dots\dots(9)$$

where  $\beta$  is the absolute coefficient of expansion of mercury, and  $\bar{\alpha}$  and  $\delta\bar{\alpha}$  now



refer to the material of the bulb between  $0^\circ$  and  $100^\circ$ . (There does not seem to be any objection to an extension of the foregoing argument to three dimensions.)

We have also  $T = 0^\circ$ ,  $T' = 100^\circ$ ,  $T_g = 500^\circ$  approximately, for ordinary glasses. In order to substitute values of  $\alpha$  and  $R$  we take average values as would be measured in the ordinary way for glasses of slightly differing compositions; the following would be reasonable values for, say, two soda-potash-lime-silica glasses of compositions differing by about 3–5% in the proportions of the main constituents:  $\alpha_1 = 1 \times 10^{-5}$ ,  $\alpha_2 = 0.8 \times 10^{-5}$ ,  $R_1 = 0.01$ ,  $R'_1 = 0.03$ ,  $R_2 = 0.005$ ,  $R'_2 = 0.01$ . (Existing data do not permit of exact estimates, but the sense of the variation is correct, and the variation with temperature is of the right order). Also we have  $\beta = 1.8 \times 10^{-4}$ . Using the above numerical values in equations (6), (7), (9), we find  $k \sim 0.05^\circ$ . Choosing the following values to represent a case where the delayed elastic effect is only slightly greater for glass 1 and increases by only the same ratio at the higher temperature, also with a smaller difference between the coefficients of expansion:  $\alpha_1 = 1 \times 10^{-5}$ ,  $\alpha_2 = 0.9 \times 10^{-5}$ ,  $R_1 = 0.01$ ,  $R'_1 = 0.02$ ,  $R_2 = 0.008$ ,  $R'_2 = 0.016$ , we find  $k \sim 0.003^\circ$  and still of the correct sign. On the other hand, if we take values corresponding to pure silica for glass 2, and typical values for glass 1, the estimate of  $k$  becomes about  $0.3^\circ$ .

#### § 5. EFFECT OF PRESSURE

It is worth considering whether the effects of changes in pressure on the volume of the bulb can play a part in the after-effects in mercury-in-glass thermometers, since they must always include delayed parts corresponding to the development of delayed elastic strains.

In ordinary use the most important change in pressure is that due to the increased height of the mercury column above the bulb when the thermometer is used vertically; this can amount to about 200 mm. of mercury at  $100^\circ$  in a thermometer calibrated from  $0^\circ$  to  $100^\circ$ . However, the "internal pressure coefficient" of such a thermometer is only about  $0.0001^\circ/\text{mm. Hg}$  (Guillaume 1889), so that the effect of increasing pressure is only to lower the reading by about  $0.02^\circ$  at  $100^\circ$ . An additional delayed expansion of about 1–3% of this is to be expected, that is, corresponding to not more than about  $0.0005^\circ$ . It is easily seen that this would lead to "thermal after-effects" in the usual direction in the case of a thermometer used vertically, but of too small magnitude to be important. In gas-filled thermometers used to higher temperatures the effect would of course be greater. It is probably significant that reports have not been made of differences between the after-effects shown in the horizontal and vertical positions.

#### § 6. CONCLUSION

We have thus accounted for the order of magnitude of the thermal after-effects by postulating a distribution of local composition corresponding to differences of only a few per cent in the relative proportions of the main constituents. Since large coefficients of expansion and large delayed elastic effects are usually found together—in glasses containing a high proportion of soda, potash, or both, for instance—it is to be expected that the effect will be in the direction usually noted. However, it is clear from equation (8) that effects in the reverse direction are not excluded by this explanation; they might also occur in glasses where the relationship between expansivities and delayed elastic effects is not as assumed here. It should be realized that the division of the material into two types of region which are present in equal abundance is no more than a mathematical

device, and the values of  $R$  must then be regarded as average values for a given type of region. If one assumed differing relative proportions of two types of region it would probably be justifiable to assume greater differences in the corresponding values of  $R$  so that the result would again be of the same order.

It seems probable that the effective structural variations are in fact inhomogeneities of composition. There is no need to justify this assumption of local variations in composition, which may perhaps be of colloidal dimensions; their existence can easily be demonstrated (see for instance Tooley and Tiede 1944), and repeated grinding and melting is actually necessary in the preparation of a glass required, say, for phase-equilibrium studies, where a higher degree of homogeneity is required than normally. It should be remembered, however, that variations in local structure are themselves ultimately responsible for the delayed elastic effects. A very clear picture of the thermal after-effects is possible if we attribute them to the presence of larger inhomogeneities than those which give rise to the delayed elastic effects, as assumed in the foregoing analysis. The general argument is, however, probably still valid if inhomogeneities of the same kind, possibly of very small dimensions, are actually responsible for both effects. These "inhomogeneities" might in fact simply be the irregular or amorphous atomic structure of the glass; it should be noted that the sizes of the regions do not appear in the analysis. It is not impossible that specially prepared homogeneous glass might show smaller after-effects of both kinds; as far as is known no experimental evidence yet exists on this point. (It should perhaps be stressed that we do not in any case consider the different regions as being separately composed of the individual chemical constituents—of silica and soda in a soda-silica glass for instance—but have considered the possibility of the mixture or solution of these constituents varying in composition from place to place.)

The relation described between the two after-effects offers a satisfactory explanation for the fact that a certain time is required at the higher temperature for the full zero-depression to be shown on subsequent cooling; in the recovery of delayed strains after removal of an ordinary mechanical stress only that part of the total is recovered which has had time to develop during the period of application of the stress. It also explains satisfactorily the fact that the effects increase with increasing temperature changes, though not always according to simple laws. There is a further point of interest, namely, that the zero-depression is much more persistent than, say, the "steam-point elevation", which usually disappears in about ten minutes and is generally not noticed. Similarly, the time required at the steam-point for full subsequent development of the zero-depression is also of this order. An explanation is possible if we realize that the glass cooled to  $0^\circ$  is actually compelled to recover delayed strains of magnitude greater than those normally corresponding to that temperature. It is not surprising that a long time is required, though as far as is known the direct mechanical counterpart of this behaviour has not been investigated in experiment. There is, however, a somewhat related phenomenon, known as "thermo-recovery", shown by some organic polymers, including polystyrene. After deformation this material recovers only partially, but on heating to a higher temperature further recovery occurs.

The reversible thermal after-effects might be expected to appear in polycrystalline metallic specimens in which crystallites of differing expansivities



occur together. However, the mercury-in-glass thermometer provides a very sensitive test for these changes, and this is probably the reason why they have been especially noted in glass. A somewhat related effect has of course been described for metals, known as "thermal fatigue", in which repeated changes of temperature can result in a permanent change in density.

The irreversible secular rise in the zero of a mercury-in-glass thermometer can be practically cured by heating the glass for a long period at a temperature rather lower than the normal annealing temperature, during which time the whole structure has an opportunity of approaching closer to its equilibrium condition at that temperature and the tendency to slow change at lower temperatures is thereby reduced or slowed down. This heating does not eliminate the reversible effects, however. The only ways in which it might be expected to reduce them would be by causing a slight reduction in the effective value of  $T_g$ , and by reducing the values of  $R$  on account of the closer approach to equilibrium conditions.

Finally, a word must be said about the somewhat analogous "thermal after-effect" shown by glass in the transformation region, where the equilibrium time of the process of stabilization is only of the order of minutes or hours. On rapidly raising or lowering the temperature of a specimen of glass maintained within this temperature region, there is an immediate change in volume, followed by a slow additional change in the same sense due to the slow configurational adjustments which are required in order to reach the degree of local order appropriate to the new temperature. (The values of  $\delta\bar{\alpha}/\bar{\alpha}$  due to this cause in the transformation region would be much larger than those of the thermal after-effects at ordinary temperatures.) In the present paper we have considered the thermal after-effects only in relation to the delayed elastic effects, because their equilibrium times are of the same order, and short, while the equilibrium time of the stabilization process at ordinary temperatures is probably at least of the order of hundreds of years. However, the distinction is not fundamental, and in the transformation region, where the equilibrium times of the stabilization process and the delayed elastic effects are of the same order, the two phenomena can probably be quite closely related, as suggested by Frenkel (1946). All the effects which we have considered are macroscopic manifestations of atomic migratory processes analogous to those occurring during ordinary viscous flow. In the absence of a more complete quantitative picture, the foregoing analysis is sufficient to explain how a material which shows a delayed elastic effect may also show a thermal after-effect.

#### ACKNOWLEDGMENT

The author wishes to acknowledge the helpful comments of Dr. E. Orowan, who read this paper before it was submitted for publication.

#### REFERENCES

- CRAFTS, J. M., 1882, *C.R. Acad. Sci. Paris*, **94**, 1298.
- DICKINSON, H. C., 1906, *Bull. Bur. Stand. Wash.*, **2**, 189.
- FRENKEL, J., 1946, *Kinetic Theory of Liquids* (Oxford: University Press).
- GUILLAUME, C. E., 1889, *Traité pratique de la thermométrie de précision*.
- HOVESTADT, H., 1902, *Jena Glass* (New York: Macmillan).
- JONES, G. O., 1944, *J. Soc. Glass Tech.*, **28**, 432.
- TOOLEY, F. V., and TIEDE, R. L., 1944, *J. Amer. Ceram. Soc.*, **27**, 42.
- WEIDMANN, G., 1886, *Ann. Chim. (Phys.)*, **29**, 214.
- YOUNG, S., 1890, *Nature, Lond.*, **41**, 488.

# The Initiation of Low Pressure Glow Discharges

By J. D. CRAGGS\* AND J. M. MEEK†

\* Research Department, Metropolitan-Vickers Electrical Co. Ltd.

† Department of Electrical Engineering (Electronics), University of Liverpool

*MS. received 14 January 1948*

**ABSTRACT.** Oscillographic studies of some transient low pressure gaseous discharges have been made, with particular attention to the intermittent discharges occurring before stable self-maintained glow discharges are established. The nature of these pre-glow discharges varies considerably with the nature of the gas, and attempts are made to interpret them in relation to Weissler's corona work.

## § 1. INTRODUCTION

NUMEROUS studies have been made by various investigators of the breakdown voltage/pressure relation in gases at low pressures. Huxley, Penning, Bruce and Boulind, among others, have studied He, Ne, N<sub>2</sub>, A, H<sub>2</sub>, O<sub>2</sub>, CO<sub>2</sub> and air. In their measurements the criterion for breakdown has been the sharp increase in current, as measured by a galvanometer, which occurs when breakdown commences. The increase is so abrupt (Druyvesteyn and Penning 1940) that the onset voltage is clearly defined within a narrow range, usually smaller than the accuracy of measurement. None of the above investigators reported the current-time fluctuations in the low-pressure discharge; this appears to have been first studied by Bennett (1914). Sloane (1937) investigated the discharge characteristics oscillographically for point/point breakdown in hydrogen. Extensive studies at higher pressures (~1 atmosphere) have been made by Loeb and his collaborators with oscillographs.

In the present experiments the onset of glow discharges in various gases at pressures less than 30 mm. Hg has been investigated and the results are presented in the form of oscillograms. The use of A.C. (50 c/s.) is unusual in work of this kind, though some qualitative measurements have been made in similar ways by Bennett (1914) and Tykociner *et al.* (1935), mostly for higher pressures.

The use of A.C. has some important advantages in the oscillographic measurements, but care must be taken in the interpretation of the results to distinguish between effects caused by the discharge characteristics and those which might be attributed to the alternating character of the voltage. The A.C. results have therefore been frequently checked with D.C. and, with the exception of wire/cylinder discharges in argon, it is unlikely that any but very minor effects are due to the use of A.C.

The D.C. breakdown measurements of other authors have been repeated with close agreement, as a further check on the experimental methods.

## § 2. BREAKDOWN VOLTAGES

The circuit used for the determination of breakdown voltage, and also for the later observations of the discharge characteristics, is shown in figure 1. The



breakdown voltages (figures 3-7) were measured with an accurate electrostatic voltmeter  $V$  and a potential divider  $R_2$ , and are considered accurate to  $\pm 2\%$ . After breakdown, these measurements do not give an accurate record of the gap voltage, and this was obtained oscillographically, as shown in figure 1. The

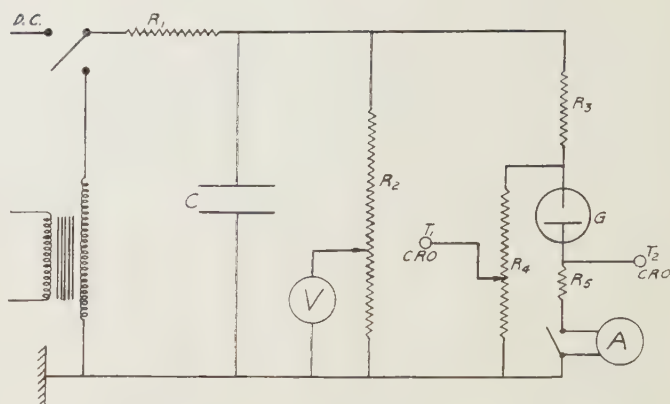


Figure 1. Circuit used for observation of onset of glow discharge at low pressures.

presence of the capacitance  $C$  ensured that the total A.C. voltage across  $R_3$  and the discharge tube was not affected by the discharge current. Currents were measured oscillographically by observation of the voltage developed across  $R_5$ . In the D.C. measurements the average discharge current was measured with the microammeter  $A$ .

The explanation of the results is facilitated by reference to the general diagram (figure 2) of voltage/current relations in a discharge (Penning and Druyvesteyn 1940). As the voltage is raised breakdown occurs at  $B$  with a sudden increase in current up to  $10^{-6}$  amp. or more;  $V_B$  is referred to as the breakdown voltage for the discharge. With further increase of current there is a region of transition

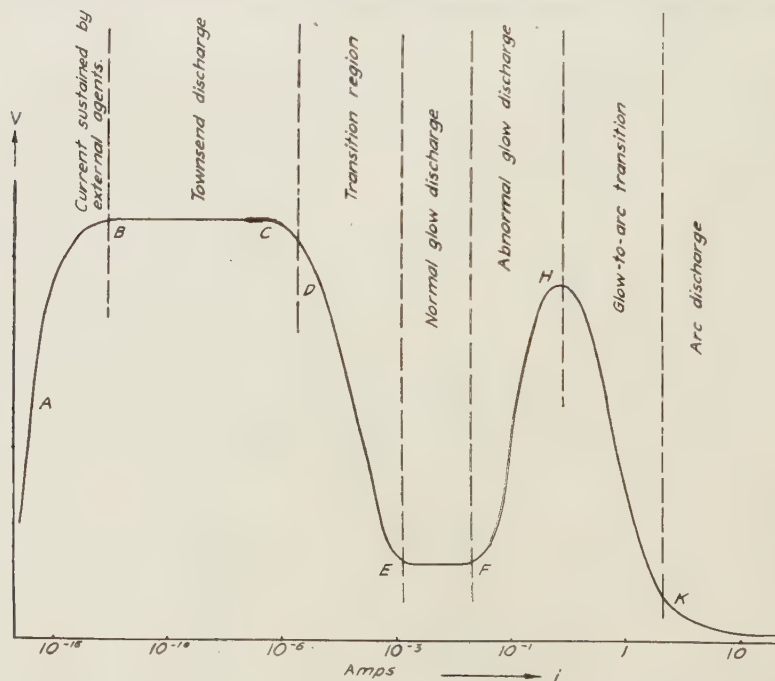


Figure 2. Representative characteristic curve of gaseous discharge.

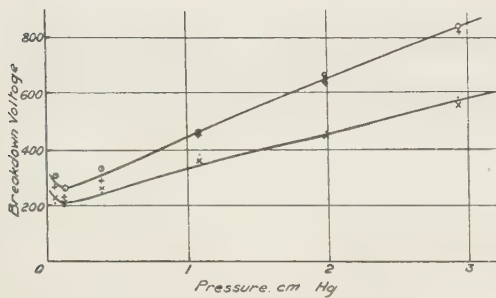


Figure 3. Breakdown voltage/pressure for argon (1/16 in. diameter round point/plane.)

- D.C. +ve.
- × D.C. -ve.
- + A.C. +ve.
- A.C. -ve.

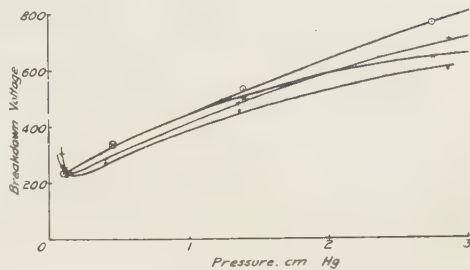


Figure 4. Breakdown voltage/pressure for argon (wire/cylinder).

- D.C. +ve.
- × D.C. -ve.
- + A.C. +ve.
- A.C. -ve.

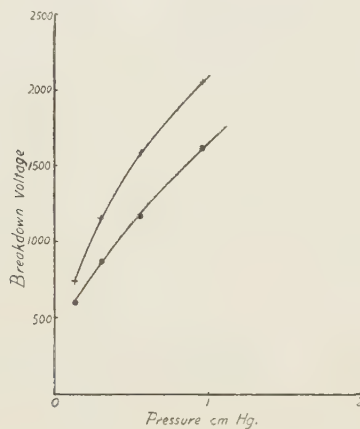


Figure 5. Breakdown voltage/pressure for  $\text{CCl}_2\text{F}_2$  (freon) (wire/cylinder).

- + A.C. +ve.
- A.C. -ve.

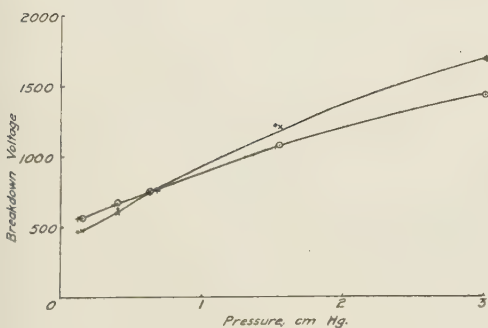


Figure 6. Breakdown voltage/pressure for oxygen (wire/cylinder).

- D.C. +ve.
- × D.C. -ve.
- + A.C. +ve.
- A.C. -ve.

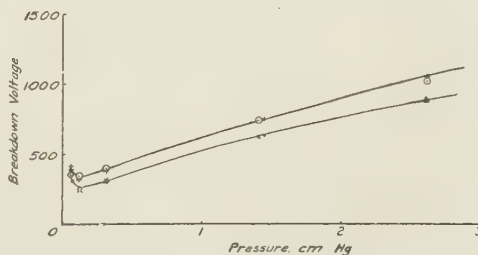


Figure 7. Breakdown voltage/pressure for hydrogen (wire/cylinder).

- D.C. +ve.
- × D.C. -ve.
- + A.C. +ve.
- A.C. -ve.



DE and a region EF of fully established glow discharge. In the present experiments the region CDE is of major interest.

Various forms of discharge gaps (point plane and wire/cylinder) were studied, but in most of the experiments the electrodes consisted of a tungsten wire 0.126 cm. in diameter surrounded by a coaxial copper cylinder of 2.5 cm. internal diameter mounted in a glass tube. The discharge space was about 12 cm. in length. The electrodes were chemically clean, but no precautions were taken to free the apparatus from impurities by continued evacuation at high temperatures. The composition of the gases used was such that, with the exception of methane which was not analysed, a purity of at least 99.5% was obtained. Some of the argon included 2% of nitrogen, but spectroscopically pure argon behaved similarly. An Apiezon oil manometer was used to avoid mercury vapour contamination.

Curves showing the variation of breakdown voltage with pressure for different gases (A.C. and D.C.) are given in figures 3–7. The point/plane gap of figure 3 was 1 cm. in length and the point was ground roughly spherical and of radius approximately 1 mm. In all the gases used, with the exception of argon, there is no detectable difference between the positive D.C. breakdown voltage and the A.C. peak voltage which causes discharge onset on the positive half-cycle. Similarly no difference is observed between the negative D.C. and A.C. breakdown voltages. This indicates that the time between the crests of successive half-cycles is sufficient to allow the clearance of ions from the gas and so to prevent the influence of space charge created on one half-cycle from affecting the subsequent half-cycle. In argon, however, the A.C. breakdown voltage is appreciably lower than the D.C. value, when the wire/cylinder arrangement is used.

It was also observed in argon that small currents flow during the positive half-cycles if appreciable currents are established during the preceding negative half-cycles. These effects, we suggest, may be attributed to the persistence of metastable atoms in argon, but no similar effects were detected in the other gases used, some of which ( $N_2$ , He and Ne) are known also to possess metastable states. In these latter cases it would therefore appear that the lifetimes of the metastable atoms are short although the selective ionization of suitable impurities (Penning effect) may also have been greater in argon than in the other gases mentioned.

The values of the breakdown voltages measured agree closely with those of other workers. Direct comparison of the  $V$ - $p$  curves is not possible because of the different electrode diameters used, but it is convenient to compare curves relating  $rX$  and  $rp$  where  $r$  is the wire radius and  $X$  is the voltage gradient at breakdown at the wire surface. In the latter curves, provided the diameter of the outer cylinder is large compared with the wire diameter, measurements of breakdown voltage as a function of pressure give values lying on the same curve for any given gas. The validity of this method of comparison of breakdown gradients is discussed by Huxley (1928).

Figures 8–11 show curves of this type and include similar curves obtained by other investigators (Penning 1931, Huxley 1928, 1930, Boulind 1934, 1935). In argon (figure 8) the curve for a positive wire is in close agreement with that obtained by Penning, but there is an appreciable difference between the two curves for a negative wire, probably on account of the difference in wire materials used. The latter difference will not affect the breakdown for a positive

wire (Loeb 1939, p. 511) for which the criterion for discharge onset is governed, at these pressures, by photo-ionization in the gas or by electron emission at the cylindrical cathode, and is given by

$$\eta \theta g / \bar{\alpha} \exp \left( \int_r^R \alpha dx \right) = 1. \quad \dots\dots(1)$$

Here  $\alpha$  is the ionization coefficient for collision by electrons in the gas,  $\bar{\alpha}$  is the mean value of  $\alpha$  near the wire,  $\theta$  is the number of photons produced by an electron

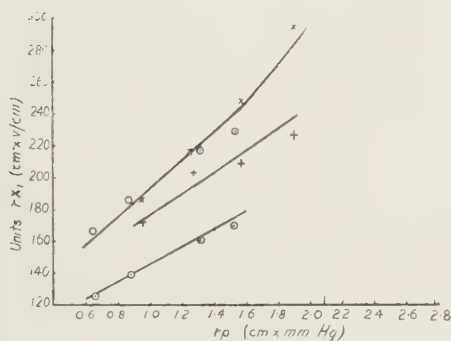


Figure 8. Breakdown characteristics for argon (wire/cylinder).

+ve {  $\circ$  Penning Ni wire.  
 $\times$  present work W wire.  
 -ve {  $\circ$  Penning.  
 $\times$  present work.

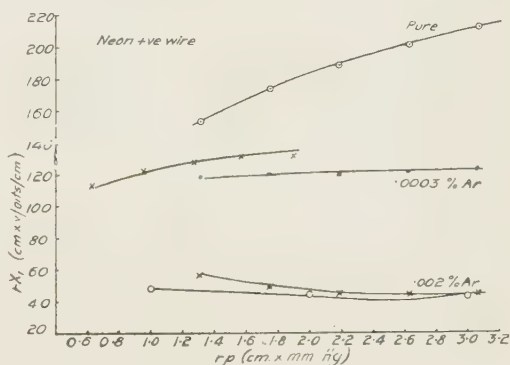


Figure 9. Breakdown characteristics for neon (+ve wire/cylinder).

{  $\circ$  Penning's results.  
 $\bullet$  Present work.  
 $\circ$  Huxley.

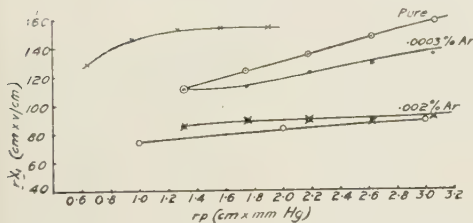


Figure 10. Breakdown characteristics for neon (-ve wire/cylinder).

{  $\circ$  Penning's results.  
 $\bullet$  Present work.  
 $\circ$  Huxley.

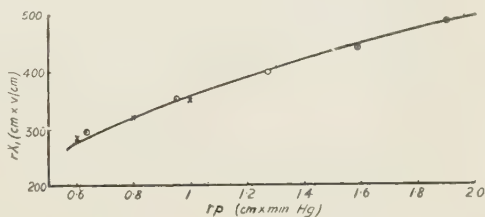


Figure 11. Breakdown characteristics for oxygen (+ve wire/cylinder).

$\circ$  Present work.  
 $\times$  Boulind's results.

per cm. of path in the direction of the field,  $\eta$  is the fraction of photons which produce electrons that succeeds in leaving the cathode, and  $g$  is a geometrical factor. The wire material has therefore no effect on the onset of the positive discharge, but will have considerable influence on the negative wire breakdown because of the resultant change in the secondary ionization coefficient which largely governs the onset of the negative discharge. The criterion for onset at the negative wire is generally taken as

$$\exp \left( \int_r^R \alpha dx \right) = 1 + (1/\gamma). \quad \dots\dots(2)$$

$\gamma$  is the number of secondary electrons leaving the cathode per incident particle or quantum.



It is clear that the lower the value of  $\gamma$  for the wire cathode the higher will be the voltage gradient required to cause breakdown of a given gas at a given pressure. Such considerations probably explain the difference between the curve obtained by Penning, who used a nickel wire, and that of the present authors, whose wire was of tungsten. No measurements comparing the value of  $\gamma$  for these materials in argon appear to be given in the literature.

Similar considerations apply to the other gases, where there is also closer agreement between the positive breakdown values than between those for negative breakdown. Additional interest is attached to the neon results because of Penning's experiments on the effects of contamination of this gas with small amounts of argon. As shown in figure 9, which gives some of the curves obtained by Penning, an amount of only 0.0003% of argon in the neon alters appreciably the breakdown voltage curve. The effect is attributed to the presence of metastable neon atoms, whose excitation potential is in excess of the ionization potential of argon, and which consequently exert an important influence on the breakdown voltage for the gas. Penning's results indicate that Huxley's measurements must have been made in neon which probably contained argon. In the present experiments it would appear that the neon used was comparatively pure, with less than 0.0003% argon, as shown by comparison of the curves for the positive wire. The results for the negative wire are again difficult to compare, as explained above, on account of the use of tungsten rather than nickel wire, but tend to confirm the purity of the gas and the lower value of  $\gamma$  for tungsten.

Figure 11 shows the extremely close agreement between Boulind's results and those of the present experiments for positive discharges in oxygen. The hydrogen results also show the same satisfactory agreement. In these tests minor impurities are apparently not important.

In agreement with the results of other workers (Loeb 1939, p. 513) breakdown at the reduced pressures used in these experiments generally occurs at a lower voltage when the smaller electrode is negative than when it is positive. This is true for all the gases used except oxygen (see figure 6) and air, as Boulind (1934) and others had previously shown. The reason for these exceptions is not altogether clear, but it is probably not entirely due to the high electron attachment coefficient in oxygen as suggested by previous authors because, in the case of partially dissociated freon,\* where the attachment coefficient is also high because of the presence of free halogens, the negative breakdown curve lies below the positive curve (figure 5). It is possible, however, that the work function of the cathode may be appreciably affected in the presence of oxygen, either by an absorbed oxygen layer or by oxidation, and calculations based on these experiments indicate that the value of  $\gamma$  at onset of the negative breakdown is much lower in oxygen than for the other gases. In these calculations the usual criterion  $\exp\left(\int_r^R \alpha dx\right) = 1$ † is assumed to define the negative breakdown, and the value of  $\int_r^R \alpha dx$  has been determined for the various gases in the negative breakdown field at 30 mm. Hg pressure. The resultant calculated values of  $\gamma$  are given in table 1, using breakdown voltages from figures 3–11. The values of  $\alpha/p(f(X/p))$  for hydrogen, argon, nitrogen and oxygen respectively, which were used in the calculations of  $\gamma$  given in table 1, were taken from the papers of Hale

\*  $\text{CCl}_2\text{F}_2$ , known commercially as a refrigerant, "Freon 12".

† In practice, see table 1,  $\gamma \ll 1$ .

(1938, 1939), Kruithof and Penning (1936, 1937), Bowls (1938), and Posin (1936) for nitrogen, and Masch (1932).

Table 1

Gas	$X/p$ (v/cm/mm.)	$\gamma$	$\gamma$ (Loeb)
Hydrogen	173	$25 \times 10^{-3}$	$25 \times 10^{-3}$
Argon	120	$4.5 \times 10^{-3}$	$15 \times 10^{-3}$
Nitrogen	285	$2.5 \times 10^{-3}$	$20 \times 10^{-3}$
Oxygen	295	$2 \times 10^{-5}$	—

The breakdown voltage for nitrogen at 26 mm. Hg pressure was 1400.

The last column gives results from Loeb (1939, pp. 392 *et seq.*) for  $\gamma$  with a Pt surface. The above values of  $\gamma$  may be considered as correct in order of magnitude and indicate a very much lower value of  $\gamma$  in oxygen than in the other gases. The relevance of this result does not seem to have been appreciated in earlier work. Some confirmation of it is obtained by the authors' calculations based on the results of Huxley (1928, 1930) and Boulind (1934, 1935) who found that the negative breakdown potentials in  $N_2$  and  $O_2$  at 6 mm. Hg for a nickel wire (1.65 mm. in diameter) in a cylinder 46 mm. in diameter were 515 and 960 volts respectively. The calculated values of  $\gamma$  are  $0.18$  and  $2.8 \times 10^{-4}$ . A full discussion of the significance of  $\gamma$  and its interpretation when used in the conventional breakdown formula (given above) for low pressure gaseous conduction is given by Druyvesteyn and Penning (1940) and Loeb (1939).\*

### §3. NATURE OF CORONA EFFECTS

The main purpose of the present experiments was to examine the discontinuities occurring in the region CDE of figure 2. The oscillographic technique was not suitable for investigation of the Townsend discharge, region BC of figure 2, which may also be expected to exhibit discontinuities (electron avalanches). Currents in the region BC are  $1 \mu a.$  or less, whereas currents in the discontinuous region of the glow discharge onset may be  $10$ – $100 \mu a.$

Earlier investigators, e.g. Bruce (1930), Boulind (1934) and Penning (1931), used galvanometers of sensitivity approximately  $6 \times 10^{-11}$  amp mm. to detect breakdown and did not observe the current wave-forms. Sloane (1937) obtained results in hydrogen which showed the presence of certain regions in the  $i/v$  curves where static characteristics could not be obtained, and oscillographic measurements were made.

In this section is described the nature of the current variations observed with the circuit of figure 1 when the voltage is above that defined as the breakdown voltage in §2. Current values are  $5$ – $500 \mu a.$

The types of current variation may be briefly summarized. (a) The current varies smoothly with voltage from  $1$ – $5 \mu a.$  (not measurable) to a value occurring at the peak of the applied A.C. voltage wave: see for example the negative current of figure 16(c), and the positive current of figure 15(c). With D.C. the same

\* The authors are greatly indebted to Professor L. B. Loeb for pointing out that the calculation of  $\gamma$  in high fields may sometimes be uncertain unless Morton's (1946) work on  $\alpha$  in fields where  $X$  varies appreciably over one electron mean free path ( $L_e$ ) is considered. Morton shows that if  $\phi = (L_e/X)(dX/dx) < 2.5\%$ , then the error introduced when the Townsend  $\alpha$  is used  $< 25\%$ . For the field at the wire in the present arrangement  $\phi$  varies from about 1% to 4% for the various gases, so that the error introduced in the integrated values of  $\alpha$  from wire to cylinder used for the calculation of  $\gamma$  (see equation (2)) will not be significant. The  $\gamma$  values in table 1 should only be taken as accurate to one significant figure.



effect is observed. (b) The current records often show time variations of the relaxation oscillation type, similar in general appearance to the Trichel pulses (Trichel 1938, 1939) observed in high pressure negative corona and to those observed with the flashing neon lamp (resistance/capacitance circuit). Figure 15(d) shows a D.C. record with a ripple due to the rectifier circuit; with A.C. it is sometimes observed, as in figure 17 (positive), that with increased voltages the extinction current is higher than when lower voltages are used. Sometimes (figure 21(c), positive) several modes of this type of current variation occur. Current oscillations may also be observed at low currents, whilst at higher currents for the same

Table 2. Details of oscillograms shown in figures 12-15

Figure	Gas	Pressure (cm. Hg)	$V_p$ (v.)	$V_c$ (v.)	$I$ (ma/cm.)	$R_5$ ( $\Omega \times 10^5$ )	$t$ (sec.)
12(a)	Argon	2.84	1020	+ 700 - 620	0.70	1.02	1/100
12(b)	"	1.37	520	+ 485 - 445	"	"	1/25
12(c)	"	"	570		"	"	"
12(d)	"	"	780		"	"	"
13(a)	Argon	0.40	337	+ 285 - 270	0.098	7.3	1/25
13(b)	"	"	457		"	"	"
13(c)	"	"	521		0.70	1.02	"
13(d)	"	"	594		"	"	1/100
14(a)	Argon	0.13	315	+ 240 - 240	0.052	1.38	1/25
14(b)	"	"	322		"	"	"
14(c)	"	"	343		"	"	"
15(a)	Hydrogen	2.66	1140	+1060 - 890	0.70	1.02	1/100
15(b)	"	"	1200		"	"	"
15(c)	"	"	1530		"	"	"
15(d)	"	"	1097		"	"	D.C.
15(e)	"	"	1138		"	"	D.C.

$V_p$ =peak voltage applied to ( $R_5$ +tube);  $V_c$ =corona onset (or breakdown) voltage;  
 $I$ =current sensitivity on records;  $t$ =total c.r.o. sweep time.

Positive currents are above the centre line on the oscillograms. Reference to figures 22 and 23 will aid in an understanding of figures 12-15. The latter are 3/5 full size.

records they are not seen, even when the current falls towards zero after passing the peak. (c) A discontinuity in a current wave of type (a) or (b) is observed, after which a smooth current variation is observed, see figure 19(c) (positive). Type (c) may be safely interpreted as showing a transition to a stable glow discharge. It is likely that case (b) often corresponds to a relaxation oscillation caused by a falling discharge characteristic and a negative total circuit resistance (Schulze 1932 and references there cited). The current discontinuities may be due to space charges the result of which is to choke off the discharge, which subsequently re-starts, as the work of Kip and Trichel has shown. It is not easy to separate these effects with certainty because, while circuit constants may have an effect on the frequency of relaxation oscillations caused by the

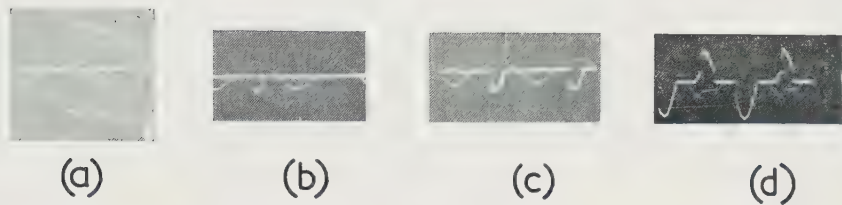


Fig. 12.

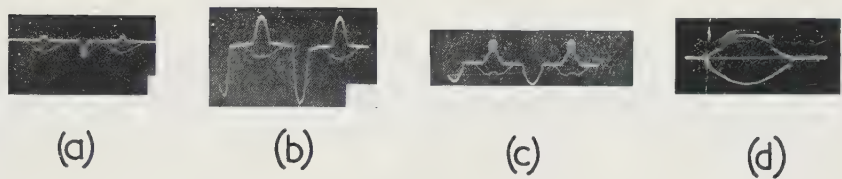


Fig. 13.

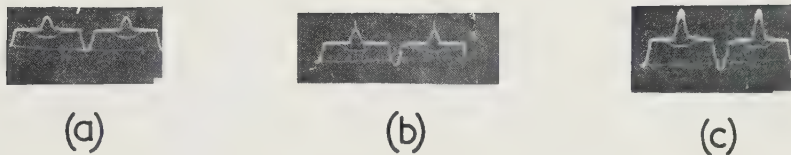


Fig. 14.

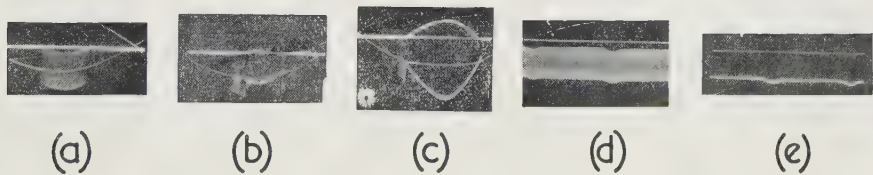


Fig. 15.



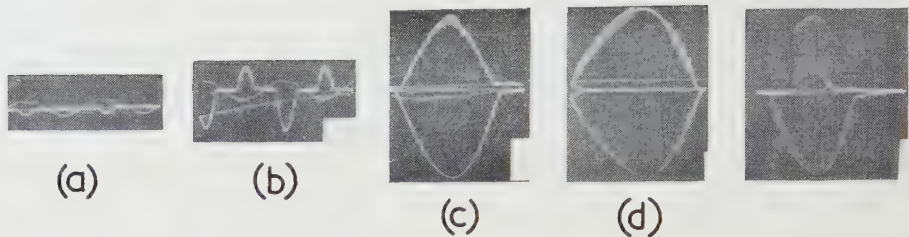


Fig. 16.

Fig. 17.

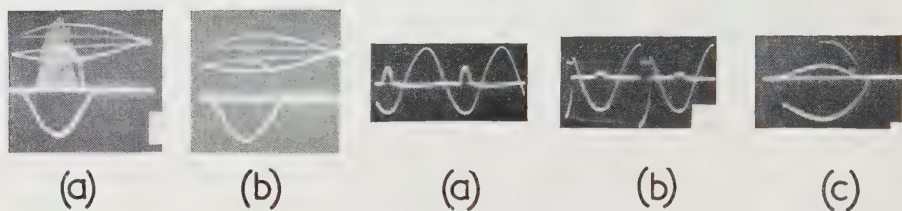


Fig. 18.

Fig. 19.



Fig. 20.

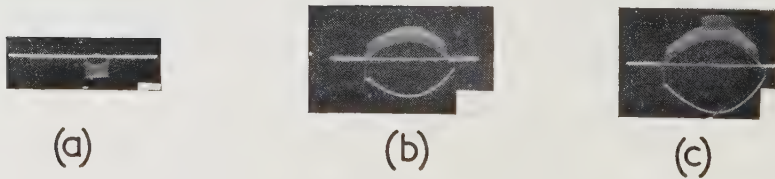


Fig. 21.

difference between striking and extinction voltages and the existence of a negative circuit resistance, these same constants may also affect the space charge phenomena. It is hoped in later work with much longer gaps and correspondingly low circuit resistances to distinguish clearly between these effects, and to assess the effect of circuit parameters in general on the observed nature of the oscillations.

It is difficult to account for case (a). The finite resolving power of the oscillograph may not allow rapidly varying currents to be accurately observed, so that only a mean current is measured. It is possible in some cases that a Townsend current is being observed (see for instance Druyvesteyn and Penning

Table 3. Details of oscillograms shown in figures 16-21

Figure	Gas	Pressure (cm. Hg)	$V_p$ (v.)	$V_c$ (v.)	$I$ (ma/cm.)	$R_s$ ( $\Omega \times 10^5$ )	$t$ (sec.)
16 (a)	Hydrogen	0.14	382	+ 340 - 260	0.098	7.3	1/25
16 (b)	"	"	485		"	"	"
16 (c)	"	"	688		"	"	1/100
16 (d)	"	"	1732		0.70	1.02	"
17	Methane	0.20	770	+ 960 - 678	0.098	7.3	1/100
18 (a)*	Freon	0.70	1570	+ 1760	0.22	3.28	1/100
18 (b)†	"	"	"	- 1350	"	"	"
19 (a)	Oxygen	1.54	1340	+ 1070 - 1170	0.098	7.3	1/25
19 (b)	"	"	1370		0.70	1.02	"
19 (c)	"	"	1800		0.15	4.8	1/100
20 (a)	Oxygen	0.68	870	+ 770 - 770	0.098	7.3	1/25
20 (b)	"	"	960		0.70	1.02	1/100
20 (c)	"	"	1158		"	"	"
20 (d)	"	"	2020		0.15	4.8	"
21 (a)	Oxygen	0.38	744	+ 660 - 600	0.70	1.02	1/100
21 (b)	"	"	1057		"	"	"
21 (c)	"	"	1200		"	"	"

$V_p$ =peak voltage applied to ( $R_s$ +tube) ;  $V_c$ =corona onset (or breakdown) voltage ;  
 $I$ =current sensitivity on records ;  $t$ =total c.r.o. sweep time.

Positive currents are above the centre line on the oscillogram.

\* Without radium } Note that measurements of the positive corona onset voltage are  
 † With radium } unsatisfactory owing to the strong effect of the radium.

1940, p. 104), but the magnitudes of currents of type (a) are often too great, as in figure 16(c), for this explanation to be tenable.

The oscillographic results for wire/cylinder gaps having the electrode sizes given in §2 show the following characteristics: (a) with argon (figures 12-14) only disruptive discharges are noticed at the higher pressures (10-30 mm. Hg), as in figure 12(a). The positive discharges often start smoothly. At the lower pressures, oscillatory discharges occur (figure 14(c)) usually superimposed on the smooth discharges. Neon and helium tend to favour the production of oscillatory discharges in preference to the disruptive or continuous types.

(b) Hydrogen (figures 15 and 16) gives oscillatory currents at all but the lowest pressures, i.e. below the Paschen minimum. At 30 mm. Hg and with a sharp point, smooth discharges are noticed at low currents. The correlation between A.C. and D.C. records is shown by figures 15(d) and 15(e). Some of the records also show oscillograms of tube voltage, e.g. figure 15(b). (c) Oxygen (figures 19–21) gave oscillations at all but the lowest pressures, but the negative discharges were smooth at the higher pressures. The unusual effect shown in figure 23(c) was most prominent; there appear to be three modes of discharge, of a similar nature, which occur one by one as the current is increased. Discharges in air also show these features. Figure 22 shows an enlargement of figure 19(b) taken with oxygen. The oxygen results also show, figure 19(a), that positive

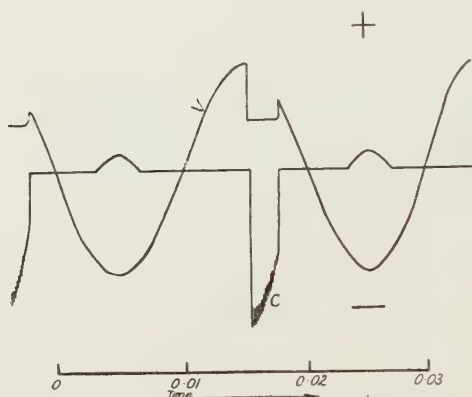


Figure 22. Current/time and voltage/time A.C. oscillogram for oxygen (wire/cylinder). Enlargement of figure 19(b), see table 3 for data.  
V, voltage curve; C, current curve.

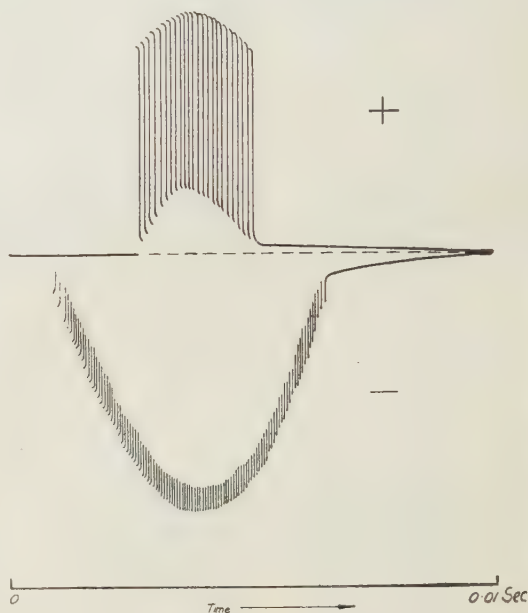


Figure 23. Current/time A.C. oscillograph for methane (wire/cylinder). Enlargement of figure 17, see table 3 for data.

breakdown may occur at lower voltages than negative breakdown, which is a characteristic property of oxygen (figure 6). Disruptive discharges are noticed in oxygen at the higher pressures (figure 19(c)). Boulind (1934) detected disruptive discharges by observation, not with an oscillograph but by the less satisfactory method of detecting the large voltage drop introduced into the circuit by such discharges. It was stated (Boulind 1934) that negative discharges in oxygen were always disruptive, but the present investigation does not confirm this conclusion for pressures below about 2 mm. Hg (figure 21(a)). (d) Nitrogen gave oscillations at all pressures observed. The wire cylinder gap gave smooth positive and negative discharges only at the highest currents and pressures. (e) Freon ( $\text{CCl}_2\text{F}_2$ ) (figure 18) was studied because of the general interest in this gas as an insulator. Disruptive or continuous discharges were prominent and the oscillatory types were usually observed only at the lower pressures. The great effect of irradiation with radium gamma-rays is shown in figures (18 a)



and 18(b), taken respectively with and without irradiation. (In the other gases, for the conditions of current etc. obtaining in these experiments, such irradiation had negligible effect on the records. However, 0.2 mg. of radium was placed a few millimetres from the tube for all the experiments described in this paper). There would appear to be such a shortage of free electrons, presumably because of the high attachment coefficient in dissociated freon, that gamma-rays give rise to observable effects even in the presence of intermittent positive discharges (figures 18(a) and 18(b)) of  $\sim 0.2$  ma. and stable negative discharges also of  $\sim 0.2$  ma. It is to be expected that irradiation would affect the positive discharges because of the relatively large cathode area (the cylinder), while for the negative wire discharges the field at the wire will be high enough to prevent attachment from being effective. (f) Methane (figure 17) was studied as an example of a complex molecular gas. Oscillatory discharges were noticed, except at the highest pressures, when continuous positive discharges, becoming disruptive, and disruptive negative discharges were observed. Figure 17 is shown enlarged as a particularly good example of the oscillatory type of discharge (figure 23).

Experiments, using several of the above gases, were made with D.C. Invariably the same sequence of events was observed, showing that the use of A.C. had no important effect on the nature of the phenomena observed, as discussed in previous communications (Craggs and Meek 1943 a and 1943 b). The lowered A.C. breakdown with argon has been discussed in §2.

As the use of A.C. renders the presentation of results easier, the use of D.C. was discontinued except for purposes of checking the A.C. results.

#### §4. DISCUSSION OF RESULTS

Figure 24 shows drawings, not to scale, of some of the D.C. discharges. A point/plane gap was used, for convenience in observation, as there seemed to be no significant differences in the character of discharges in wire/cylinder and point/plane gaps. It seems clear from figure 24(i) that the disruptive discharges are normal glows, but that the oscillatory discharges show in general a fairly uniform illumination of the whole gap. Both kinds of discharge often occur together. The spinning discharges are probably caused by time variations of  $\gamma$  at the cathode surface due to bombardment. It seems that none of the discharges observed in these experiments were of Townsend type since the currents would then be less than  $1 \mu\text{a}$ . Such discharges, if observable visually, would presumably show continuous illumination in the gap.

Valle (1926) and others have pointed out that intermittent discharges may be expected for the falling part (CDE) of figure 2 if the total circuit resistance is negative (Cobine 1931, pp. 207–209), i.e. if

$$de/di + R < 0, \quad \dots\dots(3)$$

where  $de/di$  is the slope of the discharge characteristic at the point of its intersection with the voltage/current line for the circuit resistance  $R$ . This is not in itself an explanation of the oscillatory discharges, since it is necessary to show how such a negative characteristic is produced and to explain its variation with different gases in terms of the movements of ions and electrons. Schulze's (1932) description of the discharge path as having a natural impedance, i.e. reactance and resistance, seems inadequate.

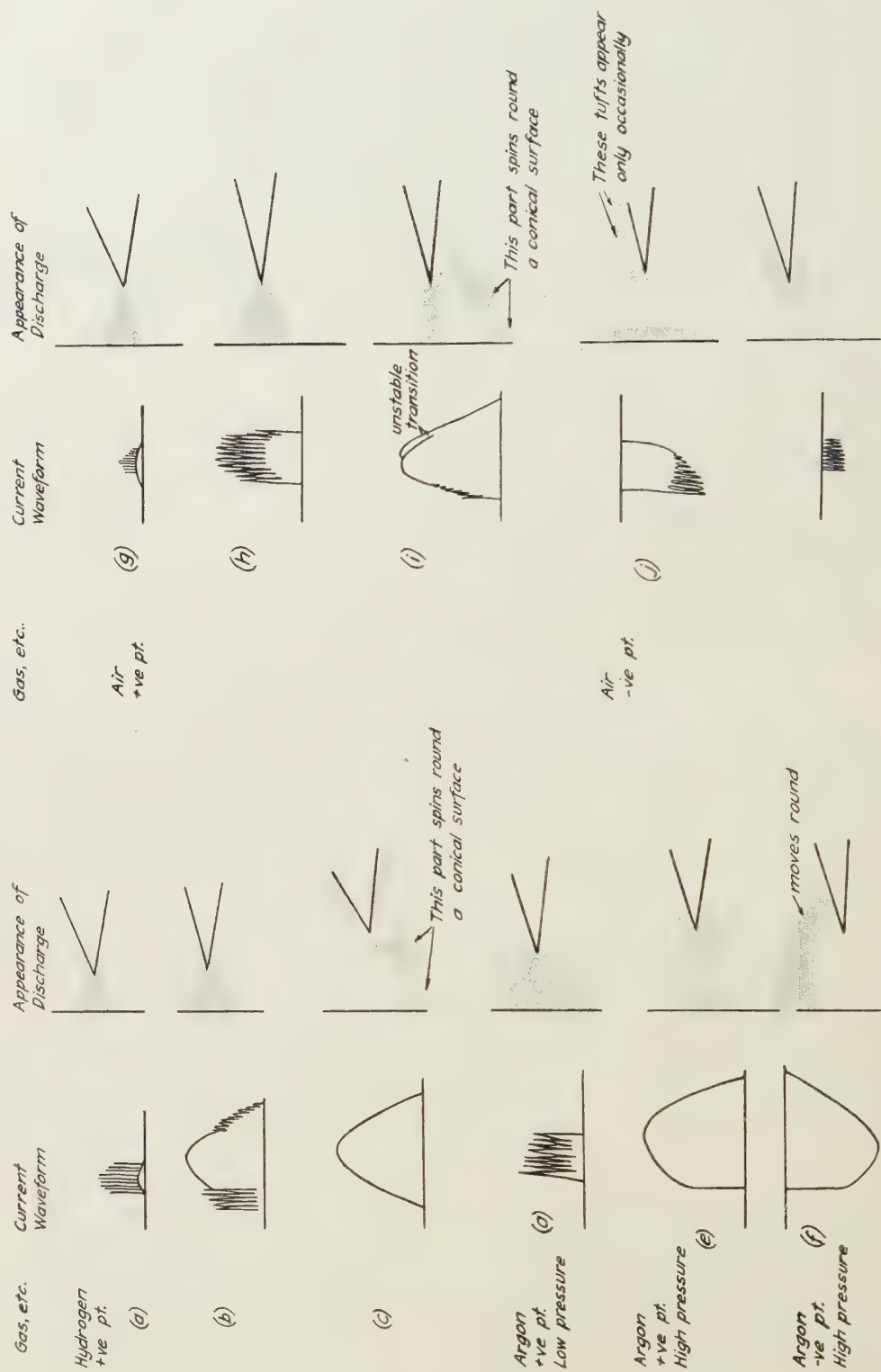


Figure 24. Appearance of discharges in argon and hydrogen for different types of current wave-form.

Penning (1931) and Penning, Moubis and Addink (1933) have studied argon discharges in a wire/cylinder gap in which the radii of wire and cylinder were respectively 0.087 cm. (nickel) and 2.3 cm. (iron). For a positive wire the effect of space charges became apparent, when the pressure was 12.7–197 mm. Hg, at 1–10  $\mu$ a. and the characteristic became positive. For lower pressures the characteristic was negative. (In the Townsend régime space charge effects are not encountered.) These and other effects are explained as follows (Druyvesteyn and Penning 1940).

For positive corona, an increasing current leads to accumulation of positive space charge round the wire where the field is thus weakened. So long as the field  $X$  at the cathode is too low for the Townsend coefficient  $\alpha$  to be appreciable, it follows that an increase in the voltage  $V$  is necessary for maintenance of the increased current. If  $X$  becomes appreciable at the cathode, the space charge augments the total ionization in the gap and  $V$  passes through a maximum, and the characteristic becomes negative so that a glow discharge is obtained.

Continuing the arguments of Druyvesteyn and Penning (1940, p. 124), it follows that in electron-attaching gases such as oxygen, air, Freon etc. at fairly high pressures, so that  $X/p$  at the cylinder is too low to ensure detachment, the negative corona has a positive characteristic. Corona may for the present purpose be defined as a discharge lying between the Townsend and glow discharges. For non-attaching gases, e.g. argon, negative corona has a negative characteristic at the higher pressures, from the above discussion. Penning's results for argon, quoted above for positive corona, showed that the negative corona had a negative characteristic for pressures greater than 1 mm. Hg with transitions to intermittent discharges, and a positive characteristic for pressures less than 1 mm. Hg.

These conclusions for argon are supported by the results given above (figures 12–14) which show immediate transitions to a glow discharge, i.e. disruptive discharges, for a negative wire at higher pressures, while the positive discharge is stable up to large currents as shown in figures 12(a) and 12(c).

The positive corona in hydrogen is continuous, at the higher pressures, to greater currents than in argon, in agreement with Weissler's (1943) conclusion that complete breakdown to a spark at pressures  $\sim 1$  atmosphere (or, as in the present case, to a glow at low pressures) took place much more readily in argon, where the presence of metastable atoms leads to more efficient photo-ionization than in relatively photon-transparent gases such as hydrogen.

Negative discharges in hydrogen are also seen to be more continuous than in argon, for the same general reasons as those given above, although the discontinuous type of negative discharge in hydrogen replaces the disruptive negative discharges in argon. Photo-ionization, discussed by Weissler, is more important at higher pressures, say about 1 atmosphere; at lower pressures, such as those used in the present work, mechanisms at the cathode are more important. Weissler found that positive and negative breakdown occurred at approximately the same voltage in argon, but not in hydrogen, at 1 atmosphere, since electron generation in the gas is the controlling process for both negative and positive discharges at these pressures. The present results, taken at much lower pressures than Weissler used, do not show this effect (see figures 4 and 7).

The oxygen discharges do not show, except at the lowest pressures, the continuous positive discharge shown at high pressures ( $\sim 3$  cm. Hg) by hydrogen or argon. This is possibly because the formation of negative ions by attachment



does not allow positive space charges to build up round the wire and so produce the positive characteristic in the manner explained above.

#### § 5. CONCLUSIONS

The use of low frequency A.C. for the oscillographic observation of low pressure breakdown effects in gases has been shown to lead to simplifications of technique.

The method described has also shown that such breakdown processes differ considerably with the nature of the gas investigated. In certain gases, e.g. argon, breakdown usually leads to the formation of a fully established glow discharge without intermediate intermittent discharges. In other gases, e.g. hydrogen, a great variety of intermittent discharges are observed. Some of these are qualitatively explicable and their connection with negative discharge characteristics is indicated. Photo-ionization is probably an important mechanism in argon discharges, and in this connection the results of Weissler seem to be confirmed.

#### ACKNOWLEDGMENTS

The authors are greatly indebted to Professor L. B. Loeb for many searching criticisms and comments, and also for his kind encouragement. They also wish to thank Mr. F. R. Perry for his support of the work and Sir Arthur Fleming, Director, and Mr. B. G. Churcher, Manager, of Metropolitan-Vickers Research Department, for permission to publish the paper.

#### REFERENCES

- BENNETT, E., 1914, *Trans. Amer. Inst. Elect. Engrs.*, **33**, 571.  
 BOULIND, H. F., 1934, *Phil. Mag.*, **18**, 909 ; 1935, *Ibid.*, **20**, 68.  
 BOWLS, W. E., 1938, *Phys. Rev.*, **53**, 293.  
 BRUCE, J. H., 1930, *Phil. Mag.*, **10**, 476.  
 COBINE, J. D., 1941, *Gaseous Conductors* (New York : McGraw-Hill).  
 CRAGGS, J. D., and MEEK, J. M., 1943 a, *Nature, Lond.*, **152**, 386 ; 1943 b, *Phys. Rev.*, **64**, 249.  
 DRUYVESTEYN, M. J., and PENNING, F. M., 1940, *Rev. Mod. Phys.*, **12**, 87.  
 HALE, D. H., 1938, *Phys. Rev.*, **54**, 241 ; 1939, *Ibid.*, **56**, 815.  
 HUXLEY, L. G. H., 1928, *Phil. Mag.*, **5**, 721 ; 1930, *Ibid.*, **10**, 185.  
 KIP, A. F., 1938, *Phys. Rev.*, **54**, 139 ; 1939, *Ibid.*, **55**, 549.  
 KRUTHOF, A. A., and PENNING, F. M., 1936, *Physica*, **3**, 515 ; 1937, *Ibid.*, **4**, 430.  
 LOEB, L. B., 1939, *Fundamental Processes of Electrical Discharge in Gases* (New York : John Wiley).  
 MASCH, K., 1932, *Arch. Elektrotech.*, **32**, 589.  
 MORTON, P. L., 1946, *Phys. Rev.*, **70**, 358.  
 PENNING, F. M., 1931, *Phil. Mag.*, **11**, 961.  
 PENNING, F. M., MOUBIS, J., and ADDINK, C. C. J., 1933, *Physica*, **13**, 209.  
 POSIN, D. Q., 1936, *Phys. Rev.*, **50**, 650.  
 SCHULZE, W., 1932, *Z. Phys.*, **78**, 92.  
 SLOANE, R. W., 1937, *Phil. Mag.*, **23**, 534.  
 TRICHEL, G. W., 1938, *Phys. Rev.*, **54**, 1078 ; 1939, *Ibid.*, **55**, 382.  
 TYKOCINER, J. T., TARPLEY, R. E., and PAINE, E. B., 1935, *Bulletin* 278, *Illinois Univ. Engng. Exptl. Station*.  
 VALLE, G., 1926, *Phys. Z.*, **27**, 473.  
 WEISSLER, G. L., 1943, *Phys. Rev.*, **63**, 96.

# The Pressures Exerted by an Underwater Explosion Bubble on a Circular Target Plate in a Disc-like Baffle

By A. R. BRYANT

Admiralty

*MS. received 18 December 1947*

**ABSTRACT.** The general equations of motion are derived for a target plate in a finite rigid baffle under the influence of pressures due to a "point source" on the axis of the target. The fluid is assumed incompressible so that the theory should be a fair approximation in the case where the pressures are due to the oscillation of the gaseous products of an underwater explosion.

The effect of the water loading on the target plate due to its own motion appears in the equation of motion as an increase in the inertia of the target. A formula for this added mass is derived for a circular target plate dishing "proportionally". The added mass is calculated for a target radius half that of the baffle in both the "piston" and "paraboloid" types of proportionally constrained motion, and it is found that it differs from the corresponding value when the baffle is infinite by not more than 15% in both cases.

The pressure distribution over a rigid disc-like baffle is computed for various distances of the explosive source. Except when the source distance is small compared to the baffle radius, the pressures are considerably lower than in the case of an infinite baffle.

## § 1. INTRODUCTION

EXPERIMENTAL studies of the damaging effect of underwater explosions frequently make use of a circular air-backed target plate mounted in a rigid annular baffle. Under the impact of the primary shock-wave sent out by the explosion the target is dished, drawing energy from the incident wave, and the waves diffracted from the baffle, in a complicated manner. The length of the pressure pulse and the distance of the explosive charge from the target are commonly of the same order as the radius of the target plate or baffle, and the extremely difficult diffraction problem has so far only been tackled by very approximate methods.

It is known that under certain circumstances a second pressure pulse is generated by the oscillating bubble formed by the gaseous products of the explosion, which can also contribute in marked degree to the dishing of the target plate. This secondary pulse is not shock-fronted, the rise and fall of pressure being much more gradual than in the primary shock-wave. The pulse length is often several times the linear dimensions of the target, so that an incompressible treatment is likely to be a fair approximation. In the following note the problem is simplified to the consideration of a hydrodynamic point source situated on the axis of a rigid disc. The solution obtained is thought to be of wider interest as a limiting case in acoustical problems involving rigid discs or circular vibrating membranes.

## § 2. STATEMENT OF PROBLEM

Figure 1 shows diagrammatically the rigid disc or baffle AB, centre O, and the explosion centre E. The dotted portion CD represents the light air-backed target plate which acquires a velocity normal to the plane AB under the influence

of the explosion pressures. In practical targets there must always be some rigid structure behind the central portion CD to keep the fluid pressures from the back of the target plate. For the present purpose this is simplified by the assumption that the normal fluid velocity must be zero over the whole of the rear face (uppermost in figure 1) of the disc, and over the portion of the front face outside the target area COD. Complete symmetry about the axis  $Ox$  of the disc is assumed. As usual in such problems

the case of "proportional motion" of the target plate is assumed in which each point in the target plate moves with a normal velocity bearing a ratio to the velocity of its centre which is independent of time. The special case of a piston-like target plate in which all points move at the same velocity will be considered in detail.

When steel target plates dish under explosive loading the energy absorbed in the plastic stretching of the steel is usually large compared to the elastic energy involved, and may be taken as proportional to the square of the central deflection. This central deflection will be denoted by  $z$ .

Figure 1 also shows the two coordinate systems used. Cylindrical coordinates  $x, \rho$  are taken with the origin at the centre of the disc and the positive  $x$  direction is the line OE;  $\rho$  denotes the distance of any point from this axis.

Oblate spheroidal coordinates  $r, s$  are also used, chosen so that the system of ellipsoids  $r = \text{constant}$  varies between the limiting case  $r = 0$  which reduces to the disc AOB, and  $r = \infty$  which is a sphere at infinity. The surfaces  $s = \text{constant}$  are hyperboloids of one sheet and vary from  $s = -1$  which is the negative  $Ox$  axis, through  $s = 0$  which is the plane of the disc, to  $s = +1$  which is the positive  $Ox$  axis. Both the  $r$  and  $s$  coordinates are therefore continuous in the space lying outside the disc, i.e. in the fluid, negative values of  $s$  corresponding to the region behind the disc. A point source of strength  $4\pi$  is situated at E, which has spheroidal coordinates  $(r_0, 1)$  and cylindrical coordinates  $(x_0, 0)$ . The radius of the disc is  $C$ , while the radius of the target plate need not for the moment be specified.

The relation between the two systems of coordinates is

$$x = Crs; \quad \rho = C(r^2 + 1)^{\frac{1}{2}}(1 - s^2)^{\frac{1}{2}}. \quad \dots\dots(1)$$

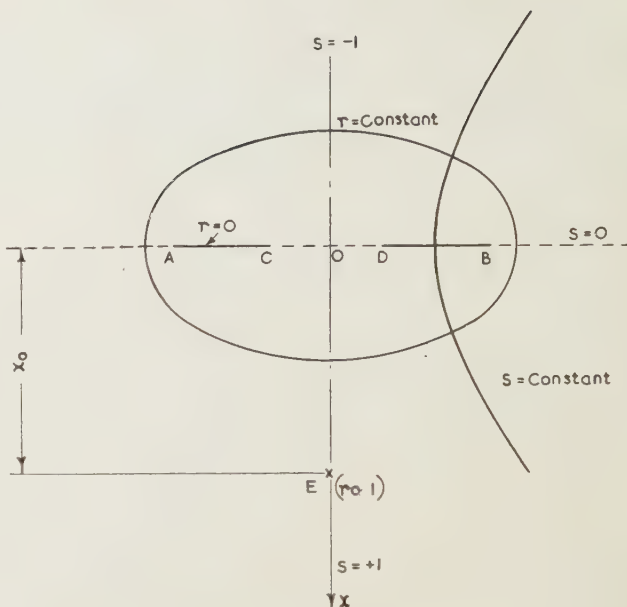


Figure 1. Spheroidal coordinates.



## § 3. VELOCITY POTENTIALS

Let  $\phi_1$  be the velocity potential due to a point source of strength  $4\pi$  at E, in the presence of the rigid disc. Thus  $\phi_1$  reduces to the reciprocal of the distance at points very close to the source, and produces zero normal velocity over the whole of the disc. Let  $\phi_2$  be the velocity potential which would arise if the point source were absent, due to the motion of the target plate with unit central velocity in the direction of  $z$  increasing; i.e. away from the explosion centre.

The velocity potential due to an explosion bubble of radius  $a$  at E will approximate very closely to  $a^2\dot{a}\phi_1$  provided that  $a$  is small compared to the dimensions and distance of the disc, and this assumption will be made in what follows.

Thus the complete velocity potential for the explosion bubble and the moving target plate is

$$\phi = a^2\dot{a}\phi_1 + \dot{z}\phi_2, \quad \dots\dots(2)$$

## § 4. LAGRANGIAN ANALYSIS

The system comprising the target plate and the fluid will now be treated by the Lagrangian method of generalized coordinates; the two coordinates necessary to specify the motion of the system are here  $z$  and  $a$ . Then if  $T$  be the kinetic energy of the system, the Lagrangian equations of motion yield

$$d(\partial T/\partial \dot{z})/dt - \partial T/\partial z = Q, \quad \dots\dots(3)$$

and a similar equation for the variable  $a$ , which is here irrelevant.  $Q$  is the "generalized force" corresponding to the displacement  $z$ . It is defined so that if the target plate suffers a small deflection  $dz$  the potential energy of the system decreases by  $Q dz$ . In this case  $Q$  is equal to  $-kz$ , where the constant  $k$  may be evaluated from the relation between energy absorbed and deflection  $z$  for a particular type of target plate.

By a theorem in hydrodynamics the kinetic energy of the fluid is given by the expression  $-\frac{1}{2}\sigma \int \phi \frac{\partial \phi}{\partial n} ds$ , where  $\sigma$  is the fluid density taken over all the boundaries of the fluid, i.e. over the disc and bubble surface; the integral vanishes over the boundary at infinity.  $\partial \phi/\partial n$  is the gradient of  $\phi$  along a normal drawn inwards towards the fluid, and is therefore the velocity along the outward drawn normal.

To this must be added the kinetic energy of the target plate  $\frac{1}{2}m\dot{z}^2$ . For a piston,  $m$  is its actual mass, while for any other case of proportional motion  $m$  may be readily obtained by integration. The total kinetic energy  $T$  is therefore given by the expression

$$T = \frac{1}{2}m\dot{z}^2 - \frac{1}{2}\sigma \left\{ a^2\dot{a}^2 \int \phi_1 \frac{\partial \phi_1}{\partial n} ds + a^2\dot{a}\dot{z} \int \phi_1 \frac{\partial \phi_2}{\partial n} ds + a^2\dot{a}\dot{z} \int \phi_2 \frac{\partial \phi_1}{\partial n} ds + \dot{z}^2 \int \phi_2 \frac{\partial \phi_2}{\partial n} ds \right\}, \quad \dots\dots(4)$$

in which the integrals are to be taken over the disc and the bubble. Equation (4) may be simplified by the following considerations:

(i)  $\partial \phi_1/\partial n$  vanishes over the disc. Over the bubble the first integral reduces to  $-4\pi a$ .

(ii) Since  $\phi_1$  and  $\phi_2$  are potentials satisfying Laplace's equation, by Green's theorem the second and third integrals are equal.

(iii) The second and fourth integrals vanish over the bubble surface since  $\partial\phi_2/\partial n$  has equal and opposite values at corresponding points on opposite sides of the bubble, while  $\phi_1$  and  $\phi_2$  are substantially constant over the bubble surface.\*

Equation (4) now becomes

$$T = \frac{1}{2}m\dot{z}^2 + 2\pi\sigma a^3\dot{a}^2 - \frac{1}{2}\sigma\dot{z}^2 \int \phi_2 \frac{\partial\phi_2}{\partial n} ds - \sigma a^2\dot{a}\dot{z} \int \phi_1 \frac{\partial\phi_2}{\partial n} ds, \quad \dots\dots(5)$$

in which the integrals are taken over the target only.

The Lagrangian equation (3) now gives the equation of motion of the target

$$\dot{z}[m + M] + kz = \sigma Pd(a^2\dot{a})/dt, \quad \dots\dots(6)$$

where  $M = -\sigma \int \phi_2 \frac{\partial\phi_2}{\partial n} ds$  and  $P = \int \phi_1 \frac{\partial\phi_2}{\partial n} ds$  over the target.  $\dots\dots(7)$

It may be remarked at this stage that equation (6) would be obtained for any shaped target and rigid baffle, the only difference being in the form of the two potential functions  $\phi_1$  and  $\phi_2$ . The quantity  $M$  is usually called the "added mass" or "virtual mass", and is the increase of the effective inertia  $m$  of the target due to the mass of fluid which is set in motion by it. This added mass is independent of the system of sources which ultimately causes the motion of the plates, but it does depend on the shape and size of the rigid baffle.

In the special case of a piston-like target the two quantities  $M$  and  $P$  become

$$M' = -\sigma \int \phi_2 ds; \quad P' = \int \phi_1 ds \text{ over the piston.} \quad \dots\dots(7a)$$

In this case it can be seen that the right-hand side of (6) is simply the total load which would be exerted by the source over the region of the disc occupied by the target if the target were not moving.

Equation (6) is similar to the simple equation for the behaviour of a piston on a spring subjected to a pressure varying in a known way with the time. In order to make it of practical use the potentials  $\phi_1$  and  $\phi_2$  must now be considered in detail and the quantities  $M$  and  $P$  evaluated.

## § 5. POTENTIAL DUE TO POINT SOURCE AND DISC

Consider the potential

$$\phi = \sum_{m=0}^{\infty} \frac{i}{C} (2m+1) P_m(ir) Q_m(ir_0) P_m(s), \quad \dots\dots(8)$$

for  $r < r_0$  where  $P_m$  and  $Q_m$  are Legendre functions of the first and second kind respectively, which may be shown to satisfy Laplace's equation when expressed in terms of the spheroidal coordinates. Along the axis of the disc, which is the line  $s = +1$ , it reduces to

$$\phi = \sum_{m=0}^{\infty} \frac{i}{C} (2m+1) P_m(ir) Q_m(ir_0) = \frac{1}{C(r_0 - r)} = \frac{1}{x_0 - x},$$

this being Heine's expansion. Consequently (8) is the potential of a point source of strength  $4\pi$  situated at  $(r_0, 1)$  in an infinite fluid expressed in the spheroidal coordinates.

\* In the limiting case when  $a$  tends to zero,  $\phi_1$  and  $\phi_2$  may be removed from the integrals; the integrals then become the flux of fluid due to the target's motion through the volume occupied by the bubble, and this clearly tends to zero as  $a$  tends to zero.

It follows that the velocity potential due to the point source in the presence of the rigid disc is

$$\phi_1 = \sum_{m=0}^{\infty} \left\{ \frac{i}{C} (2m+1) Q_m(ir_0) P_m(ir) P_m(s) + \frac{2}{\pi C} (4m+3) Q_{2m+1}(ir_0) Q_{2m+1}(ir) P_{2m+1}(s) \right\} \dots\dots (9)$$

for  $r < r_0$ ,

since  $\phi_1$  in (9) has a zero derivative with respect to  $r$  at  $r=0$ , i.e. at points on the surface of the disc, and tends to the reciprocal of the distance in the neighbourhood of the source.

The case where  $r > r_0$  is not required here. The value of  $\phi_1$  is required in (7) and (7a) for points on the disc, i.e. for  $r=0$ . It is shown in the Appendix that this expression may be put into finite terms, and the value of  $\phi_1$  at points on the disc is given by the expression

$$\phi_1 = \frac{1}{C(r_0^2 - s^2 + 1)^{\frac{1}{2}}} \left[ 1 + \frac{2}{\pi} \cot^{-1} \frac{(r_0^2 - s^2 + 1)^{\frac{1}{2}}}{s} \right], \dots\dots (9a)$$

where the angle  $\cot^{-1}[(r_0^2 - s^2 + 1)^{\frac{1}{2}}/s]$  is numerically less than  $\pi/2$  and is positive for  $s$  positive, i.e. for points in the front of the disc, and negative for points behind the disc where  $s$  is negative.

#### § 6. POTENTIAL DUE TO MOTION OF THE TARGET PLATE

It will be assumed that the motion of the target plate is axially symmetrical. Let the normal velocity  $v$  of a point on the target plate be related to its spheroidal coordinate  $s$  by the expression

$$v = \dot{z} \partial \phi_2 / \partial n = f(s) \cdot \dot{z}; \dots\dots (10)$$

$f(s)$  will, of course, be zero for values of  $s$  corresponding to points on the disc but outside the target area. For any physically reasonable distribution of target plate velocity the following expansion will be possible:

$$f(s) = s^{-1} \sum_{n=0}^{\infty} a_n P_n(s), \dots\dots (11)$$

where the coefficients  $a_n$  are given by

$$a_n = \frac{1}{2} (2n+1) \int_{-1}^{+1} s f(s) P_n(s) ds. \dots\dots (12)$$

The velocity potential  $\phi_2$  due to the motion of the target plate will then be

$$\phi_2 = -iC \sum_{n=0}^{\infty} \frac{a_n Q_n(ir) P_n(s)}{Q'_n(i0)}, \dots\dots (13)$$

since the normal velocity at the surface of the disc  $r=0$  is  $(1/Cs)(\partial \phi_2 / \partial r)_{r=0}$ . If the target plate moves as a piston, so that the normal velocity is a constant over the central region of the disc or baffle up to some radius, say  $R$ , and is zero outside this radius, we have

$$f(s) = 1, \quad S < s < 1; \quad f(s) = 0, \quad -1 < s < S$$

where  $S = (1 - R^2/C^2)^{\frac{1}{2}}$ ,

$$\text{so that} \quad a_n = \frac{1}{2} (2n+1) \int_S^1 s P_n(s) ds. \dots\dots (14)$$



### § 7. DISTRIBUTION OF POTENTIAL $\phi_1$ AND PRESSURE OVER DISC

The expression (9a) for  $\phi_1$  also gives the spatial distribution of pressure over the rigid disc. For a source of strength  $A$  at a distance  $x_0$  from the disc the pressure distribution over the disc is given by

$$p = \frac{\sigma \dot{A}}{4\pi(x_0^2 + \rho^2)^{\frac{1}{2}}} \left[ 1 + \frac{2}{\pi} \cot^{-1} \left( \frac{x_0^2 + \rho^2}{C^2 - \rho^2} \right)^{\frac{1}{2}} \right] = \frac{\sigma \dot{A}}{4\pi} \phi_1. \quad \dots (15)$$

If the disc caused no alteration in the flow the pressure at its centre would be  $\sigma \dot{A}/4\pi x_0$ , and this may be likened to the "incident pressure" in the acoustic case. In figure 2 the pressure  $p$  is divided by this "incident pressure" and

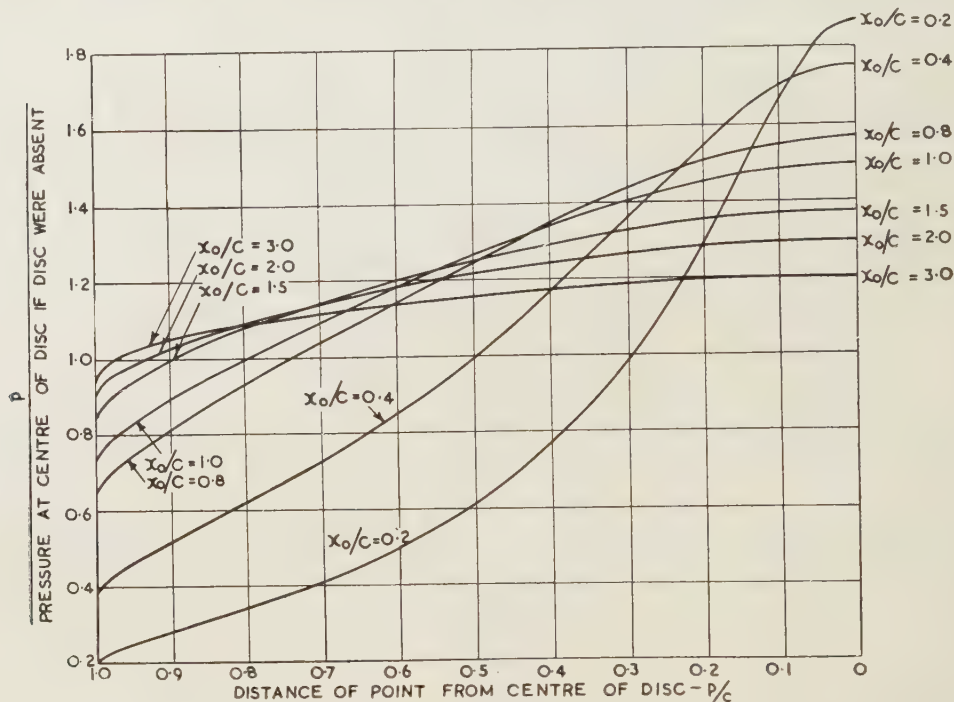


Figure 2. Total pressure  $p$  at a point on a rigid disc radius  $C$ . Distance of point source along axis of disc  $= x_0$ .

plotted as a function of distance  $\rho$  from the centre of the disc. This quantity can be seen to be equal to  $x_0 \phi_1$ , which is tabulated in table 1. For points in the

Table 1. The quantity  $x_0 \phi_1$  for a point on the surface of a rigid disc

$\rho/C$	$x_0/C \rightarrow 0.2$	0.4	0.8	1.0	1.5	2.0	3.0
0.0	1.874	1.758	1.571	1.500	1.374	1.295	1.205
0.1409	1.508	1.643	1.539	1.479	1.364	1.289	1.201
0.2431	1.144	1.464	1.480	1.439	1.344	1.276	1.195
0.3122	0.951	1.330	1.427	1.402	1.325	1.264	1.188
0.4359	0.704	1.102	1.314	1.319	1.280	1.235	1.171
0.600	0.498	0.850	1.144	1.186	1.200	1.181	1.140
0.7141	0.400	0.709	1.021	1.082	1.132	1.133	1.111
0.800	0.340	0.615	0.927	0.999	1.073	1.089	1.084
0.9165	0.268	0.497	0.791	0.872	0.975	1.013	1.034
0.9798	0.225	0.423	0.696	0.779	0.897	0.949	0.989
1.0	0.196	0.371	0.625	0.707	0.832	0.894	0.949

rear of the disc the second term in the square brackets of (15) should be given a negative sign.

### § 8. EVALUATION OF THE PRESSURE FUNCTION $P$

When the distribution of velocity over the target plate  $\partial\phi_2/\partial n$  is known, the pressure function  $P$  appearing in the equation of motion is obtained from equations (9a) and (10):

$$P = \int \phi_1 \frac{\partial\phi_2}{\partial n} ds = 2\pi C \int \frac{sf(s)}{(r_0^2 - s^2 + 1)^{\frac{1}{2}}} \left[ 1 + \frac{2}{\pi} \cot^{-1} \frac{(r_0^2 - s^2 + 1)^{\frac{1}{2}}}{s} \right] ds, \quad \dots\dots (16)$$

the integral to be taken over the target plate. In the case of a target plate of radius  $R$ , which has a constant velocity of unity over its surface, the value of  $P$  is

$$P' = 2\pi \left[ (x_0^2 + R^2)^{\frac{1}{2}} - x_0 \right] - 4(x_0^2 + C^2)^{\frac{1}{2}} \left[ \sin \theta - \theta \cos \theta \right]_{\theta_1}^{\theta_2} \quad \dots\dots (17)$$

where  $\theta_1 = \cot^{-1} x_0/C$ ,  $\theta_2 = \cot^{-1} [(x_0^2 + R^2)/(C^2 - R^2)]^{\frac{1}{2}}$ ,  $C$  being the disc or baffle radius, and  $x_0$  the distance of the point source. The ratio of the average driving pressure over the piston (i.e. the right-hand side of (6)) to the so-called "incident pressure" is seen to be  $x_0 P'/\pi R^2$ ; this quantity is plotted in figure 3 and given in table 2 for a range of values of  $x_0/C$  and  $R/C$ .

Table 2. The quantity  $x_0 P'/\pi R^2$  for a piston-like target

$x_0/C \rightarrow$	0.2	0.4	0.8	1.0	1.5	2.0	4.0
$R/C$							
↓							
0.0	1.874	1.758	1.570	1.500	1.374	1.295	1.156
0.1409	1.676	1.704	1.556	1.488	1.369	1.295	1.156
0.2431	1.427	1.600	1.532	1.469	1.359	1.285	1.153
0.3122	1.275	1.515	1.497	1.450	1.350	1.280	1.151
0.4359	1.049	1.367	1.434	1.406	1.325	1.265	1.145
0.6000	0.831	1.177	1.336	1.333	1.286	1.238	1.134
0.7141	0.718	1.059	1.261	1.274	1.250	1.214	1.125
0.9165	0.565	0.877	1.121	1.157	1.174	1.160	1.101
1.0	0.513	0.808	1.057	1.102	1.134	1.130	1.087

Figures 2 and 3 show that the principal factor in determining the increase in pressure over the target area is the ratio of the baffle radius to the source distance. Increasing the baffle round a given target plate makes an appreciable increase in the pressures over the target only when the baffle radius becomes comparable with the source distance. The pressures over the target only approach the value obtained with an infinite baffle when the baffle radius is large compared with the source distance.

### § 9. EVALUATION OF THE ADDED MASS $M$

Using equations (7), (10), (11) and (13), the added mass becomes

$$\begin{aligned} M &= \sigma \int \phi_2 \frac{\partial\phi_2}{\partial n} ds = \sigma \int_{-1}^1 iC^3 \sum_{n=0}^{\infty} \frac{a_n Q_n(i0) P_n(s)}{Q'_n(i0)} f(s) 2\pi s ds \\ &= 4\pi\sigma iC^3 \sum_{n=0}^{\infty} \frac{a_n^2 Q_n(i0)}{(2n+1)Q'_n(i0)}. \quad \dots\dots (18) \end{aligned}$$

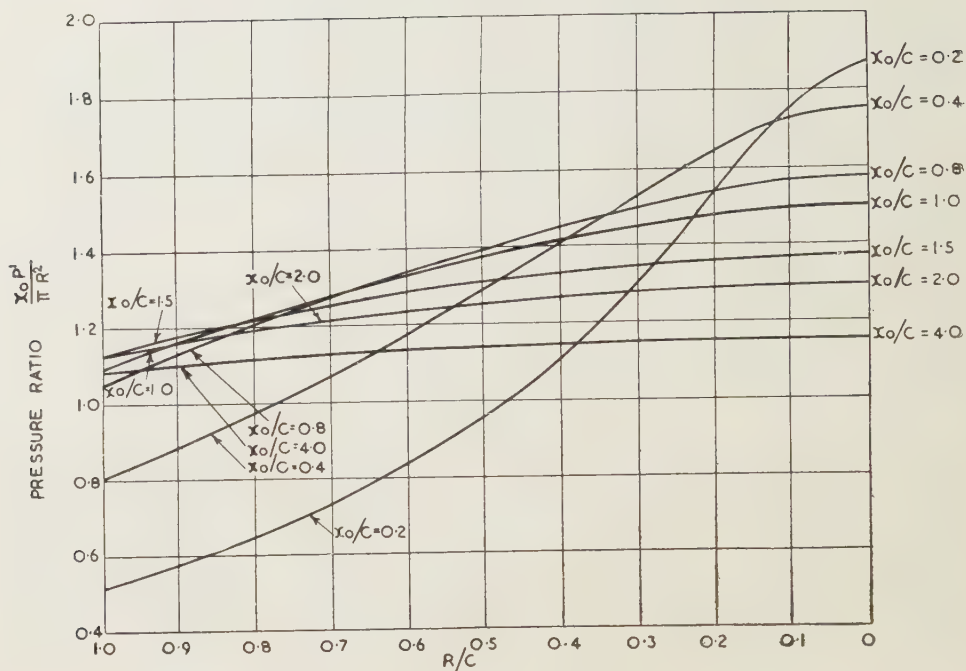


Figure 3. Average pressure over piston radius  $R$  in baffle radius  $C$  divided by pressure produced by charge at piston centre in absence of piston.

#### § 10. ADDED MASS FOR PISTON-LIKE TARGET

As a numerical example consider a piston-like target whose radius  $R$  is one half the radius of the baffle  $C$ . The coefficients  $a_n$  have been computed as far as  $a_9$ . Though the series is rather slowly convergent, the sum to nine terms is estimated to be within two or three per cent of the sum to infinity and yields for the added mass  $M'$  the value  $2.36\sigma R^3$ . This should be compared with a piston in an infinite baffle when the added mass is  $2.667\sigma R^3$ , i.e. about 12% greater.

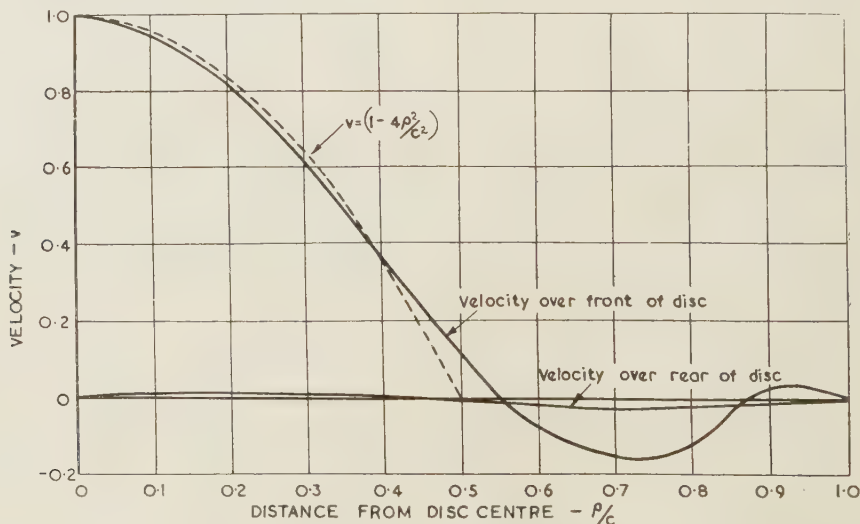


Figure 4. Approximation to parabolic distribution of velocity over target used in "added mass" calculation.



# § 11. ADDED MASS FOR PARABOLOIDAL VELOCITY DISTRIBUTION

The full line in figure 4 represents an assumed velocity distribution using only the seven coefficients  $a_0$  to  $a_6$  which were determined by a numerical method. The velocity distribution is a fair approximation to a parabola for a target plate whose radius is half that of the baffle—the exact parabola is shown dotted in figure 4 for comparison.

Using this assumed velocity distribution, the added mass is calculated to be  $0.707\sigma R^3$ . This is to be compared with the figure  $0.813\sigma R^3$  for a parabolic distribution in an infinite baffle.

It appears, therefore, that for target plates whose radius is not greater than half the baffle radius, the added mass for both the "piston" and "paraboloid" types of dishing is within 10 to 15% of the added masses in the case where the baffle is infinite.

## ACKNOWLEDGMENT

The work described above was carried out at the Road Research Laboratory of the Department of Scientific and Industrial Research, under the direction of the Director of Road Research.

## APPENDIX

### *Reduction of the potential expression to finite terms*

The first term in equation (9) for  $\phi_1$ , the potential due to the point source and rigid disc, is simply the reciprocal of the distance between the point  $(r, s)$  and the source at  $(r_0, 1)$ , and may be written down in finite terms at once. This relation is used as the starting point for the reduction of the second term in (9). Thus using (1):

$$i \sum_{m=0}^{\infty} (2m+1) Q_m(ir_0) P_m(ir) P_m(s) = [(r_0 - rs)^2 + (1 + r^2)(1 - s^2)]^{-\frac{1}{2}} \dots\dots (i)$$

$$= (r_0 s + i\alpha - r)^{-\frac{1}{2}} (r_0 s - i\alpha - r)^{-\frac{1}{2}} \dots\dots (ii)$$

In (i) and (ii)  $-1 < s < 1$ ,  $s$  real, and  $\alpha$  is the positive root of  $(r_0^2 + 1)^{\frac{1}{2}}(1 - s^2)^{\frac{1}{2}}$ . The left-hand side of (i) is uniformly convergent with respect to  $r$  for all  $r_0$  except  $r_0$  imaginary and between  $\pm 1$  and for all  $r$  lying within an ellipse in the Argand diagram having its foci at  $\pm 1$  and passing through the point  $r_0$ . In particular it is convergent for all real  $r_0$  if  $r$  is imaginary and between  $\pm i$ .

Now if  $z$  and  $r$  be any complex numbers ( $z$  not real and between  $\pm 1$ ) Neumann's expression for  $Q_m(z)$  is

$$Q_m(z) = \frac{1}{2} \int_{-1}^1 \frac{P_m(r) dr}{z - r} \dots\dots (iii)$$

Putting  $ir' = r$  and  $iz' = z$ , and then omitting primes, we get

$$Q_m(z) = \frac{1}{2} \int_i^{-i} \frac{P_m(ir) dr}{z - r} \dots\dots (iv)$$

provided now that  $z$  is not a pure imaginary between  $\pm i$ .

Now multiply both sides of (ii) by  $\frac{1}{2}(z-r)^{-1}$  and integrate with respect to  $r$  from  $i$  to  $-i$ . Reversal of the order of summation and integration in order to integrate term by term is justified because of the uniformity of convergence, and this gives, with (iv),

$$i \sum_{m=0}^{\infty} (2m+1) Q_m(ir_0) Q_m(iz) P_m(s) = \frac{1}{2} \int_i^{-i} \frac{dr}{(z-r)(\lambda-r)^{\frac{1}{2}}(\lambda'-r)^{\frac{1}{2}}}, \quad \dots\dots (v)$$

where  $\lambda = r_0 s + i\alpha$ ,  $\lambda' = r_0 s - i\alpha$ .

By changing the variable in the integral in (v) to  $x = z - r$ , the integration may be performed and (v) becomes

$$i\Sigma = \frac{1}{2(\lambda-z)^{\frac{1}{2}}(\lambda'-z)^{\frac{1}{2}}} \left\{ \sinh^{-1} \left[ \frac{r_0 s - z}{\alpha} + \frac{(\lambda-z)(\lambda'-z)z}{\alpha(z^2+1)} - \frac{i(\lambda-z)(\lambda'-z)}{\alpha(z^2+1)} \right] \right. \\ \left. - \sinh^{-1} \left[ \frac{r_0 s - z}{\alpha} + \frac{(\lambda-z)(\lambda'-z)z}{\alpha(z^2+1)} + \frac{i(\lambda-z)(\lambda'-z)}{\alpha(z^2+1)} \right] \right\}. \quad \dots\dots (vi)$$

The expression on the right of (vi) is thus of the form

$$\frac{1}{2X} \{ \sinh^{-1}(A-iB) - \sinh^{-1}(A+iB) \},$$

where  $X$ ,  $A$ , and  $B$  are all positive and real for  $r_0$ ,  $s$ ,  $z$ , positive and real and  $z < r_0 s$ . Now rewrite equation (vi) with  $-s$  in place of  $s$ . Since the  $P_m$  functions are even or odd as  $m$  is even or odd the effect of this is to reverse the sign of all the odd order terms in the summation and to leave the even order terms unaffected. If now this modified expression be subtracted from (vi) the even order terms will disappear and each odd order term will appear twice. Hence

$$2i \sum_{m=0}^{\infty} (4m+3) Q_{2m+1}(ir_0) Q_{2m+1}(iz) P_{2m+1}(s) \\ = \frac{1}{2X} \{ \sinh^{-1}(A-iB) - \sinh^{-1}(A+iB) \} \\ - \frac{1}{2X'} \{ \sinh^{-1}(A'-iB') - \sinh^{-1}(A'+iB') \}, \quad \dots\dots (vii)$$

where  $X'$ ,  $A'$  and  $B'$  are the expressions obtained by reversing the sign of  $s$  in  $X$ ,  $A$  and  $B$  respectively. We now require the limit of (vii) as  $z$  tends to zero. This is

$$i \sum_{m=0}^{\infty} (4m+3) Q_{2m+1}(ir_0) Q_{2m+1}(i0) P_{2m+1}(s) \\ = \frac{1}{4F} \{ \sinh^{-1}(D-iE) - \sinh^{-1}(D+iE) \} \\ - \{ \sinh^{-1}(-D-iE) - \sinh^{-1}(-D+iE) \}, \quad \dots\dots (viii)$$

where  $D = r_0 s / \alpha$ ;  $E = (r_0^2 + 1 - s^2) / \alpha$ ;  $F = (r_0^2 + 1 - s^2)^{\frac{1}{2}}$ .  $D$ ,  $E$  and  $F$  are thus real and positive for  $s$  positive.

The expression on the left of (viii) is  $C\pi i/2$  times the second term in the expression for the pressure on the disc—it represents the increase in the pressure

due to the source caused by the alteration of the flow round the rigid disc. Since this solution must correspond to physical reality the following two statements may be made:

(a) The right-hand side of (viii) must be a pure imaginary, positive when  $s$  is positive.

(b) The term within the second square brackets in (viii) must not be *numerically equal* to the first term. For if it were equal in magnitude and sign the expression on the right-hand side of (viii) would vanish, which is physically impossible. If, on the other hand, it were equal in magnitude, but of opposite sign, then the expression as a whole would be an even function of  $s$ , implying that the added pressure due to the presence of the disc is of the same sign on both sides of the disc, which is again physically incorrect, since the effect of any rigid obstacle is, in general, to increase the pressure on the side facing the source, and to decrease it on the other side.

It will be observed that the many-valued functions  $\sinh^{-1}$  and  $Q_m$  appear in equation (viii) and in the expression (9) for the potential. It is clear, therefore, that the particular branch of each function must be chosen so that the solution corresponds with the physical reality. In particular conditions (a) and (b) above enable one to choose the branch of the  $\sinh^{-1}$  function according to the following rule. Let  $\mu$  be a positive number between zero and infinity, and let  $\eta$  be a real angle between 0 and  $\pi/2$ . We choose that branch of the  $\sinh^{-1}$  function in which the real part is always positive, and the imaginary part always lies between  $-\pi$  and  $+\pi$ . If then  $\mu + i\eta = \sinh^{-1}(D + iE)$  where  $D$  and  $E$  are real and positive, the following scheme covers all possible cases and gives the correct value for the branch we have chosen.

$$\begin{aligned}\sinh^{-1}(D + iE) &= \mu + i\eta; & \sinh^{-1}(-D + iE) &= \mu - i\eta + i\pi, \\ \sinh^{-1}(D - iE) &= \mu - i\eta; & \sinh^{-1}(-D - iE) &= \mu + i\eta - i\pi.\end{aligned}$$

It follows that

$$\sum_{m=0}^{\infty} (4m+3)Q_{2m+1}(ir_0)Q_{2m+1}(i0)P_{2m+1}(s) = \frac{1}{(r_0^2 - s^2 + 1)^{\frac{1}{2}}} \left[ \frac{\pi}{2} - \theta \right], \quad \dots\dots (ix)$$

where  $\theta$  is the angle between 0 and  $\pi/2$  which is the imaginary part of

$$\sinh^{-1}(r_0 s / \alpha + i(r_0^2 + 1 - s^2) / \alpha).$$

On evaluating this imaginary part it is found to be the angle  $\tan^{-1}[(r_0^2 + 1 - s^2)^{\frac{1}{2}}/s]$ . Thus finally the potential at the point (0,  $s$ ) on the disc is

$$\phi_1 = \frac{1}{C(r_0^2 + 1 - s^2)^{\frac{1}{2}}} \left[ 1 + \frac{2}{\pi} \cot^{-1} \frac{(r_0^2 + 1 - s^2)^{\frac{1}{2}}}{s} \right], \quad \dots\dots (x)$$

where the angle  $\cot^{-1}[(r_0^2 + 1 - s^2)^{\frac{1}{2}}/s]$  is numerically less than  $\pi/2$  and is positive or negative as  $s$  is positive or negative, i.e. for points in front of or behind the disc respectively.



## The Impact of a Solid on a Liquid Surface

By E. G. RICHARDSON

King's College, Newcastle upon Tyne

*MS. received 17 February 1948*

**ABSTRACT.** Part I consists of a study of the motion of a solid sphere when it strikes a liquid surface vertically. The shape of the air cavity formed is delineated and explained in terms of potential flow and the resistance experienced by the sphere in this stage is measured. These factors are found to scale on the basis of a Froude parameter. The pressure developed in the cavity is also measured and found to involve reverberations in the cavity of large amplitude.

In Part II the impact forces on the sphere and other forms of projectile on entry into the liquid are studied and compared with theory. The mechanism and forces involved when a sphere ricochets after entry at oblique angles are also discussed.

---

### GENERAL INTRODUCTION

EXPERIMENTAL work on the impact of solids on water has been in the past carried out with two objects in view: (i) to study the form of the cavity and splash and, in one instance, the sounds associated with the collapse of the cavity; (ii) to measure the force of impact. During the late war interest became centred on the matter from the point of view of the behaviour of projectiles entering water, and from this aspect the author carried out the research here described at the Royal Aircraft Establishment in the period 1942–1946. Though this work was concerned with applications to water-entry ballistics and, to a lesser extent, to the impact of seaplanes on landing, it was planned as a piece of fundamental research using the sphere as basic form of solid.

The work is divided into two parts, in accordance with the classification made above.

## PART I. CAVITY FORMATION

### § 1. INTRODUCTION

The pioneer work of Worthington (1897), which surely deserves the epithet of “classical”, was done with steel spheres dropped or shot from an air-gun into water. Mallock (1918), whose paper is entitled “Sounds produced by drops falling on water” (but seems to contain no reference to sound), repeated some of these and gave a tentative explanation of the shapes of the cavities produced. Bell (1924) used other liquids, such as glycerine, but with the ball entering at such low speeds that scarcely any cavity was formed. Ramsauer (1927) shot a pellet into the side of a thin-walled tank and photographed the cavity formed, under somewhat special conditions, since the water surface was not open to the air until the wall was punctured.

All these investigators took single photographs under spark illumination.

The improvement in high-speed ciné-photography permits of a series of photographs being taken at one shot and so of the resistance to motion in the cavity stage being investigated. This, and a study of the evolution of the cavity form, was the main object of the author's experiments.

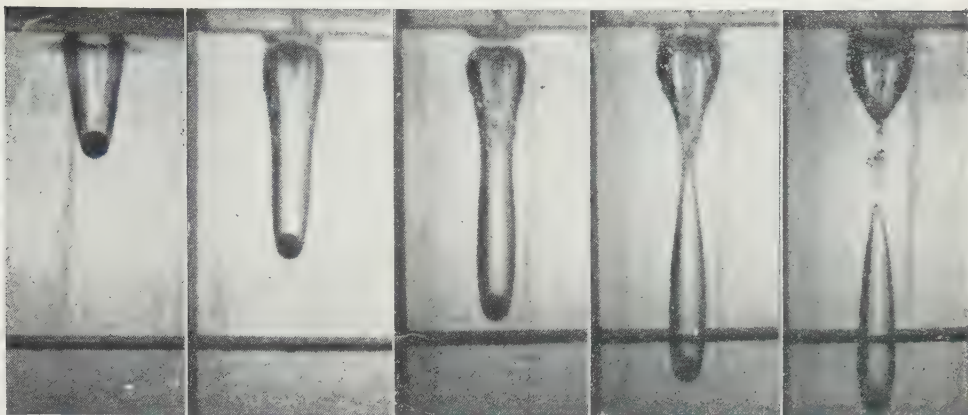


Figure 1. Entry of sphere to water under atmospheric pressure.

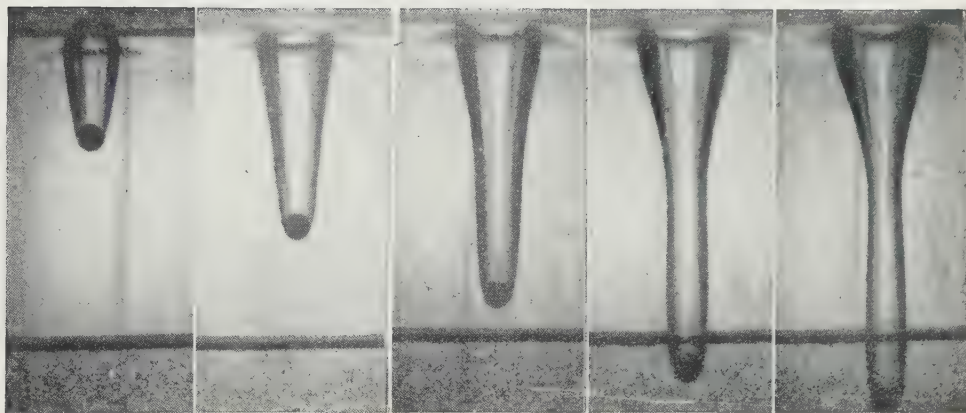


Figure 2. Entry of sphere to water under one-fifth atmospheric pressure.



Figure 10. Twenty-inch diameter hemisphere for impact force measurements.

PLATE I.

*To face page 352*



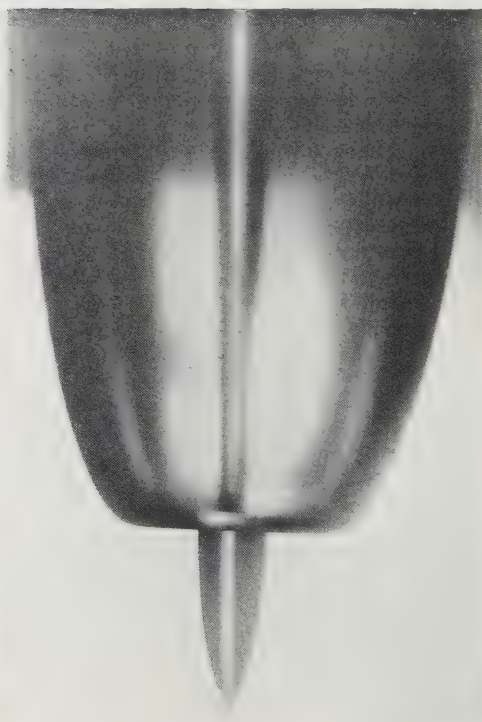
Figure 3. Details of cavity and splash due to water entry of sphere.



Figure 5. Cavity pressure recorder.



(a)



(b)

Figure 7. Cavity forms behind disc at entry to water (a); in cavitation tunnel (b).



## § 2. EXPERIMENTS

The shots were standard ball bearings, of diameters  $\frac{1}{16}$ " to 1", which were projected vertically into the liquid contained in a glass-sided tank. In some instances an air-gun was used, but as it was felt that the expulsion of air following the ball might affect the cavity, the majority of the experiments were done with the projectile falling freely. To get a sufficient fall indoors, a lift-shaft at Farnborough was used and, for greater impact speeds, the interior of the Kew pagoda, which had at the time holes cut in the wooden floors, giving a total drop of 126 ft.

The photography was done with a ciné-camera at 200 frames per sec. Typical prints are shown on plates I (figures 1, 2) and II (figure 3).

## § 3. SHAPE OF THE CAVITY

In order to study the flow of water in detail as the sphere passes vertically downward, a series of fine air bubbles was produced beneath it. They issued under pressure from a fine glass capillary on the end of a tube which was pivoted above the surface and rocked to and fro in the meridian plane of the sphere as it was shot in. The upward speed of the bubbles was very small compared to the downward speed of the projectile.

A pair of arditron flash-lamps were arranged to discharge, one shortly after the other, when the sphere had reached a set depth. These time settings were fixed from a datum instant determined by the breaking of a carbon pencil in the arditron circuits just above the surface of the water as the sphere entered. This caused the double exposure of a photographic plate, exhibiting thus the relative movement of all the bubbles in the field of view and of the sphere itself. Some photographs were taken using aniline drops in place of air bubbles, but these were not suitable for analysis.

From such photographs, and from some very good ones lent to the author by a group of American photographers who used the Egerton stroboscope, the field of flow round the sphere was deduced.

The right-hand side of figure 4 shows by the length of the arrows the velocity field relative to the camera with, as a tentative approximation to the flow, the stream lines due to a source set one-quarter of the radius eccentric to the sphere in the direction of motion. On the left-hand side this flow is compounded with the velocity of the sphere to give, by the length of the arrows, the field relative to it. The potential due to

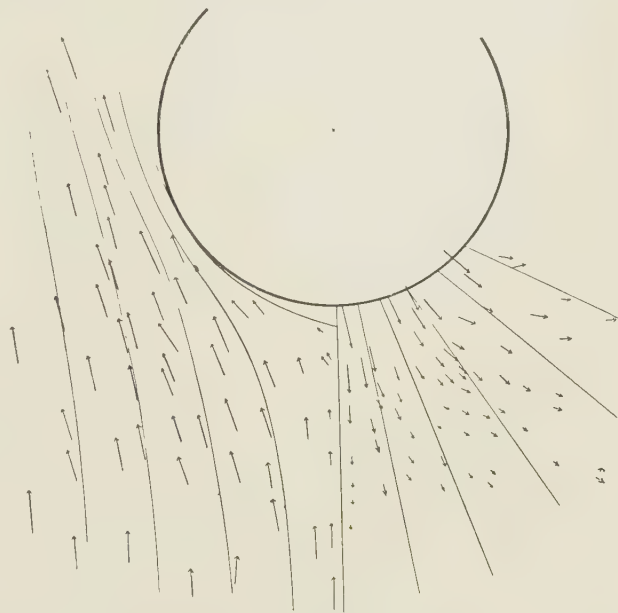


Figure 4. Experimental and assimilated theoretical flow round sphere.

a source may in fact be added to that of a uniform stream to give that at any point  $r, \theta$  (cf. Bauer 1926) with  $r$  measured from the source and  $\theta$  from the zenith  $\phi/V = a^2/r - r \cos \theta$ , whence the streamlines  $\psi/V = a^2 \cos \theta - \frac{1}{2} r^2 \sin^2 \theta$ . The streamline which divides to pass the obstacle is, however, given by  $a^2 = a^2 \cos \theta - \frac{1}{2} r^2 \sin^2 \theta$  or  $r = a \operatorname{cosec} \theta/2$ , so that the source cannot be set to make the dividing line conform to a sphere of radius  $a$ . In figure 4 it is set to give the observed value  $\theta_1$  for tangential secession from the surface, i.e.  $115^\circ$ .

After the liquid has been cleft by the passage of the sphere it reunites under the action of gravity, so nicking off the cavity behind the sphere. At the instant of closure one can represent the steady state of the cavity by a potential flow due to a source, as in figure 4, together with a linear sink of the same total strength stretching from the source vertically up to a point distant  $a$  from the closure. The corresponding stream function for a point distant  $r$  from the source and  $c$  from the upper end of the sink is  $\psi/V = a^2 \cos \theta - \frac{1}{2} r^2 \sin^2 \theta - a(r - c)$ .

In fact, the distance  $l$  from the centre of the sphere to the point of closure is a function of  $V$ , being given, for water, by  $V^2/gl = 10$  (see § 5).

It must be borne in mind that the assimilation to a potential flow is valid only for the steady state, and that in making this comparison we are ignoring the deceleration which the sphere is actually suffering. Nevertheless, as figure 4 shows, we can derive a good approximation to the field of flow by this method.

The liquids, other than water, which were used were: zinc chloride solution (specific gravity 1.75), petrol (specific gravity 0.71) and glycerine (specific gravity 1.26). It appears that  $\theta_1$  is independent of density. On the other hand, the time of closure is delayed beyond that given by the empirical formula just noted when the solid cleaves a very viscous liquid like glycerine.

Often another closure occurs at the surface (cf. figure 1) before the deep one to which the preceding discussion applies. This is due to the piling up of surface water at first impact, which causes faster closing of the lid of the cavity but, being evanescent, has little effect on the closure at depth. Surface tension forces are comparatively small at the speeds involved in this work, but may have important effects at low speeds, as Worthington and Bell have shown.

Failure to close first at the surface seems to be associated with the ability of the water to shoot up and out in a pronounced splash, and this is favoured by reduction of the atmospheric pressure (figure 2) or, at low speeds, of the surface tension (as in zinc chloride solution).

That the cavity still takes the same shape when the ball hits the water at supersonic speeds may be seen from photographs of Ramsauer and of McMillen (1945), who used rifles to fire shots into water.

#### § 4. PRESSURE IN THE CAVITY

An attempt has been made to measure the air pressure developed in the cavity during the under-water trajectory, since such information may help to elucidate the mechanism of cavity closure and disintegration. It is not to be expected that the pressure will deviate much from the atmospheric or the local hydrostatic value, so a sensitive recorder is necessary. For the trials a hollow cylindrical projectile with a heavy ogival nose was constructed. Let into the (plane) base, and flush with it, was a thin steel diaphragm (0.004 in. thick and 1.5 in. diameter) attached by a central boss to a D.V.L. scratch recorder carried inside the shell.

The recorder (Jones and Davies 1934) has a stylus moved by deflection of the diaphragm, which scratches a record of the pressure on a stainless steel ring, rotated by an electric motor. Another stylus inscribes a datum line and time marks (1,50 sec.), being actuated by a solenoid to which a current is supplied periodically by clockwork mechanism or by a standard tuning-fork. This time-marker was worked either by a battery carried in the shell or from the fork through "flying" leads. The calibration was effected by covering the base with a capsule to which air pressure, manometrically measured, could be introduced.

Figure 5 (plate II) shows the recorder with head and case removed.

It was necessary to ensure that the records in the cavity were not vitiated by the natural response of the mechanism, excited in seismograph fashion. Two tests were made: first, a drop into water was made with the capsule covering the base and hermetically sealed, when no change from atmospheric pressure could be perceived; secondly, the apparatus was dropped on the ground to record its reaction. This was a single peak which returned to zero without oscillation in about 1/100 sec. (figure 6(c)). It was therefore considered that the recorder was

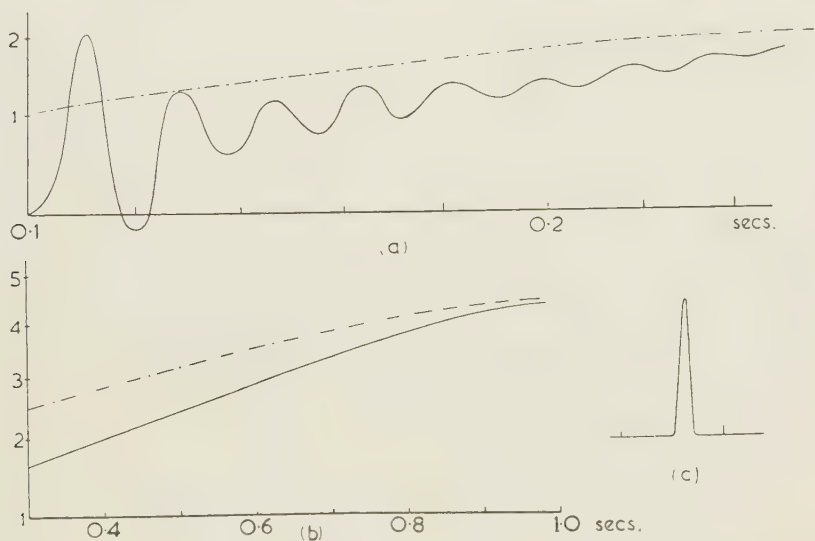


Figure 6. Cavity pressure records shown by continuous line with local hydrostatic pressure shown by chain line (a); continued at (b); record of drop on to ground (c).

sufficiently dead-beat to give a true record of pressure in the lesser deceleration experienced within the cavity when the projectile was dropped into water. The adoption of the ogival nose prevented any disturbance of the trace on hitting the water (Part II, §3). In order to mark "entry" on the records it was arranged that the time marker should come into action just as the nose touched the surface.

The apparatus was dropped nose-first into a large glass-sided tank 20 ft. deep. Ciné-photography at 200 frames/sec. enabled a depth-time record to be kept, and this was converted into one reading local hydrostatic pressure for comparison with the cavity pressure. A typical pair for entry at 20 ft/sec. is shown in figure 6 (a) and its continuation in 6 (b), beginning when the pressure in the cavity (shown by the continuous line) started to deviate from atmospheric. The chain line gives the hydrostatic pressure, calculated from the depth of the projectile.



The following features may be discerned from such records:

(i) The cavity pressure, at this comparatively low entry speed, remains nearly atmospheric until the cavity closes; (ii) as the cavity closes, large oscillations of frequency 20–80/sec. and initial amplitude up to  $1/20$  atm. supervene, but are rapidly damped and disappear in about  $\frac{1}{10}$  sec., rising in frequency as they do so, perhaps due to loss of air in smaller bubbles; (iii) the mean pressure on the diaphragm rises rapidly from this epoch as the projectile sinks, eventually catching up with the local hydrostatic pressure when the speed has dropped and the cavity mostly bubbled away.

The discovery of these acoustic vibrations seems to have completed Mallock's unfinished task. Their large decrement suggests that they are either "reverberations" of the cavity damped by turbulence, or pulsations of the shell of water surrounding the cavity, as oscillations of figure would be of lower frequency and would not change the internal pressure. On the whole the motions are suggestive of cavity resonance like those of a pop-gun. The decrement has a mean value of 2 per sec., rather more than that in Kirchhoff's theory for this case (which applies to small displacements) but of the same order as those recorded in a pipe of rigid walls by Lehmann (1934) at the corresponding frequency and amplitude.

These powerful but short-lived oscillations, as well as the significant difference (for the time being) between the internal and external pressure at the cavity, must be the cause of its breaking up into individual bubbles and final evanescence.

#### § 5. RESISTANCE IN CAVITY

If a sufficiently high frequency of photography is used it is possible to plot the displacement-time curve of the projectile after it has formed a cavity and so calculate its resistance in motion. At the entry speeds involved (4–40 m/sec.) the frictional resistance was the paramount force causing deceleration. If  $M$  is the mass of the projectile,  $d$  its diameter,  $V$  its speed,  $\rho$  the density of the liquid,

$$M\partial V/\partial t = Mg - C_D(\pi d^2/4)(\frac{1}{2}\rho V^2), \quad \dots\dots(1)$$

where  $C_D$  is a drag coefficient which relates the frictional force to the projected area of the projectile and the pressure at its front stagnation point in the conventional fashion.

This may be written, when  $\sigma$  is the specific gravity of the solid in terms of the liquid and  $s$  the path traced by the sphere,

$$\frac{1}{8}\pi d^3\sigma(g - V\partial V/\partial s) = C_D\pi d^2V^2/8.$$

When the speed and deceleration are such that the effect of gravity can be neglected, we have for the drag coefficient

$$C_D = 3.05(d\sigma/s)\log(V_0/V), \quad \dots\dots(2)$$

$V_0$  and  $V$  being the speeds at the two ends of the track  $s$ .

In the first experiments, 100 frames/sec. were used in the ciné-camera. This proved inadequate for measuring the drag, and later 200 frames/sec. or 2000 frames/sec. (the latter for shots at 40 m/sec.) were employed. Values of  $V$  were estimated by drawing slopes to the displacement-time curves at different points on the trajectory.

An analysis of the single shot at an entry speed of 650 m/sec. recorded by Ramsauer (1929) (using individual spark photographs) was also made and the drag for his sphere included with the present ones in table 1.

Table 1

Media	Steel in water	Steel in water (low press.)	Lead in water	Steel in zinc chloride	Steel in petrol	Steel in glycerine	Steel in water (Ramsauer);
Diameter (cm.)	1-2.5	1-2.5	7	1-2.5	1-2.5	1-2.5	1.1
$\sigma$	8	8	12	4.5	11	6.5	8
Mean Reynolds number } $C_D$	$3 \times 10^5$	$3 \times 10^5$	$10^6$	$3 \times 10^4$	$3 \times 10^5$	$3 \times 10^2$	$5 \times 10^3$
	0.30	0.30	0.28	0.30	0.34	0.50	0.32
$C_D$ for full immersion }	0.4	0.4	0.4	0.4	0.4	0.7	0.5

As one would expect, the values of  $C_D$  are less than those commonly associated with fully immersed spheres (quoted in the final row of the above table from *Modern Developments in Fluid Dynamics*) at these values of Reynolds number, and are unaffected by the approach to the velocity of sound (in Ramsauer's case), whereas at the Reynolds and Mach numbers corresponding to this (mean) speed the drag of a fully immersed sphere would have fallen considerably.

The motion of the projectile after entry appears to be unaffected by air pressure. Some of the experiments were repeated in a large chamber in which the air pressure could be reduced to one-fifth of atmospheric and the firing of the shot and running of the camera controlled from outside; the drag coefficient was unchanged from that at the same Reynolds number and atmospheric pressure.

It is of interest to relate this type of cavity formation due to impact on a free surface to the cavitation which ensues when a submerged body is moved through a liquid at such a speed that a vacuum or, more correctly speaking, a space saturated with the vapour of the liquid, is formed behind the projectile. As the speed increases, this vaporous cavity increases in size until it extends to a great distance in the rear of the body. Measurements in cavitation tunnels, i.e. water channels in which air-free water is circulated at high speed past a model held on a force balance, enable one to compare this type of cavitation, both as to cavity shape and resistance, with that due to impact on a free surface. If the cavitation number is defined as  $(p_1 - p_0) / \frac{1}{2} \rho V^2$ , where  $p_1$  is the actual pressure at the point on the solid where cavitation ensues and  $p_0$  is the saturation vapour pressure, then photographic comparison indicates that free-surface cavities correspond in shape to those having a zero-cavitation number. On plate II (figure 7 (a), (b)) are shown the cavity form of a disc at entry into water and in a cavitation tunnel, at a cavitation number of 0.66. Measurements of the resistance of a spherically-nosed model in the Haslar cavitation tank at a Reynolds number of  $3 \times 10^6$  and cavitation number 0.25, the lowest that can be reached therein, indicate that  $C_D = 0.2$  in the immersed model. This may be compared with the values of table 1. As closely as one can estimate from the Haslar photographs, the water secedes from the surface of a sphere in the tunnel at the same latitude ( $65^\circ$  from the pole) as in free-surface cavities.

A number of attempts have been made to calculate theoretically the drag coefficient of a sphere in a cavity. Most of these interpolate the angle just quoted. A working approximation to the experimental value of 0.3 may be derived by integrating the pressure distribution round a sphere, as observed in wind tunnels, from the pole to the latitude at which it becomes equal to the static pressure (about  $45^\circ$ ), then "stretching" this same distribution to make it cover a greater area of the surface to correspond to the wetted portion in the cavity, i. e. to a latitude of  $65^\circ$ . The value of  $C_D$  is in fact only 0.27 if the wind-tunnel distribution of pressure to an upper limit of  $45^\circ$  is taken, but becomes 0.37 if this limit is set to  $65^\circ$ .

One can also derive a value for  $C_D$  from the flow pattern of figure 4. An application of Bernoulli's theorem leads to the expression

$$(p - p_0)/\rho = \frac{1}{2} V^2 \{ (2a^2/r^2) \cos \theta + a^4/r^4 \},$$

where  $p$  is the pressure at any point  $r, \theta$  in the field and  $p_0$  the static pressure,

whence 
$$C_D = \int_{\pi}^{\theta_1} (4 \sin \theta \cos \theta + 2 \sin \theta) d\theta,$$

neglecting the discrepancy between the dividing streamline and the surface of the sphere. This gives 0.40 with  $\theta_1 = 115^\circ$ .

## § 6. BASIS OF SIMILARITY

For Reynolds numbers between  $10^3$  and  $5 \times 10^6$  it appears from (1) that the motion during cavity persistence is given by:

$$g - dV/dt = \frac{3}{4} C_D V^2 / d\sigma.$$

The specific gravity of the solid and the compressibility of gas and liquid (i. e. the imminence of the velocity of sound) have no great effect on the coefficient  $C_D$ . Now phenomena in which the forces are functions of  $V^2/d$ , such as the motion of ships, scale on a Froude basis, i. e. they are described in terms of the Froude number  $V^2/gd$ . Experiments made with spheres of different diameters at different speeds will experience the same forces and have identical cavity forms at corresponding times if the Froude number is the same.

A similarity based on  $V^2/(d \partial V / \partial t)$  does, however, neglect one factor, viz. the air pressure. In so far as these pressures in the cavity are functions of the depth below the free surface and the speed with which the air can enter, they are not scaled on a Froude basis. To the order of accuracy of these experiments, however, no change of drag coefficient with air pressure was detectable in a 1 : 5 variation of atmospheric pressure, as reported above.

## PART II. IMPACT FORCES

### § 1. THEORETICAL ASPECTS OF IMPACT ON LIQUIDS

There are two aspects from which one can regard the impact, both based on the idea of the "added mass" of liquid which the body sets in motion. On the older theory, it is supposed that when a body of mass  $M$  enters a liquid there is a sudden reduction of its velocity which is ascribed to an apparent addition to its mass by the mass of liquid  $m$  set instantaneously in motion. Thus if  $V_0$  is the velocity just before impact,  $V_1$  just after,

$$MV_0 = (M + m)V_1, \quad \dots\dots(3)$$



or if the volume of liquid is expressed as a fraction  $\mu$  of the volume of the solid and  $\sigma$  is the specific gravity of the solid relative to the liquid,

$$\sigma(V_0 - V_1) = \mu V_1 \quad \text{and} \quad \mu = \sigma(V_0/V_1 - 1). \quad \dots\dots(4)$$

Theoretical values of  $m$  are known for three shapes (cf. Lamb, *Hydrodynamics*, §§ 108, 92 and 71); the disc ( $8c^3/3$ ), the sphere ( $2\pi c^3/3$ ) and the plate of infinite aspect ratio ( $\pi c^2$  per unit length), where  $2c$  is the width. It will be noted that this conception makes the impact force infinite.

In von Kármán's and Wagner's adaptations (1932) of the "added mass" idea, it is assumed that  $m$  gradually increases during immersion and is at any instant equal to the mass of liquid contained in a hemisphere or hemi-cylinder erected on the wetted perimeter. Knowing how the latter depends on the depth of immersion and the instantaneous rate of immersion ( $V$ ), one can calculate the force-time curve for the impact in the form of  $\partial(mV)/\partial t$  against  $t$ .

## § 2. CALCULATION OF IMPACT FORCES

If an axially symmetrical body hits a liquid at a speed  $V_0$ , the force at any subsequent instant

$$F = -M \frac{\partial V}{\partial t} = \frac{\partial}{\partial t}(mV) = \frac{\partial}{\partial t}(\frac{2}{3}\pi c^3 \rho V) = \frac{2}{3}\pi c^3 \rho \frac{\partial V}{\partial t} + 2\pi c^2 \rho V^2 \frac{\partial c}{\partial h},$$

where  $h$  is the depth of immersion and  $c$  the radius of the wetted perimeter.

*Example 1.—Sphere.*

$$h = a - \sqrt{(a^2 - c^2)}, \quad \partial h/\partial c = c/\sqrt{(a^2 - c^2)},$$

whence

$$F = -mF/M + 2\pi c \sqrt{(a^2 - c^2)} \rho V^2,$$

or (with (3))

$$\frac{F}{\rho V_0^2} = \frac{2\pi c \sqrt{(a^2 - c^2)}}{(1 + m/M)^3}. \quad \dots\dots(5)$$

The maximum value of this when  $M$  is large compared to  $m$  occurs when  $c = a/\sqrt{2}$  and is then  $\pi c^2$ .

*Example 2.—Cone of semi-angle  $\gamma$ .*

$$\partial h/\partial c = \cot \gamma, \quad F/\rho V_0^2 = 2\pi c^2 \tan \gamma / (1 + m/M)^3.$$

The maximum value of this occurs when  $m = \frac{1}{2}M$  and is then  $0.86c^2 \tan \gamma$ .

It will be noticed that this theory would still make the impact force of a *disc* infinite, since it takes no account of the sideways escape of liquid to form a splash. Wagner modified the theory in this respect and applied it to obtuse-angled prisms, such as the hull of a sea-plane. The theory probably breaks down at the limit of very acute angles since the "displacement" of liquid by the volume of the immersed segment is then comparable with the added mass of the liquid set in motion.

Kreps (1943) introduced the resistance experienced by the body during immersion. The equation of motion then becomes, neglecting buoyancy, surface tension and compressibility,  $M\partial V/\partial t = -\partial(mV)/\partial t + Mg - C_D(\pi c^2)(\frac{1}{2}\rho V^2)$ .

When the velocity of impact is small, the last term is unimportant but the gravity term is not, *per contra* when the velocity is very large. In the latter case, the measured decelerations will deviate more from the theoretical as  $C_D$  is greater, i.e. for blunt-nosed projectiles.

Another method, due to Shiffman and Spencer (1947), of calculating the impact force on a sphere is derived from consideration of the flow past a lens. It leads to force-time curves of the same general type as those calculated from the Kármán-Wagner theory.

### § 3. SMALL-SCALE IMPACT FORCE EXPERIMENTS

Watanabe (1929, 1930, 1934) at the Okechi Research Laboratory used a piezoelectric gauge mounted on bodies of various shapes, viz. cone, cylinder, sphere and disc, which he dropped on to water. Connections led from the quartz to an amplifier and thence to a cathode-ray oscillograph, on which a force-time curve was inscribed as the body hit the water. Shortly after impact the deceleration reached a maximum whose value was proportional to the square of the impact velocity. He claims that the depth of immersion at which the maximum force is reached is proportional to the impact velocity for each shape, but the points on the graph by which this relationship is deduced are very scattered. When the maximum force was plotted against the weight of the falling body it was found that at

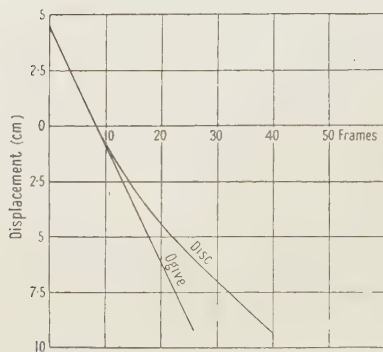


Figure 8. Displacement-time curves on water entry of disc and ogive.

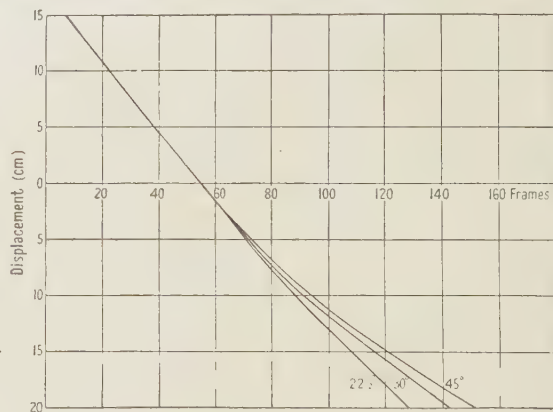


Figure 9. Displacement-time curves on water entry of cones of various semi-angles.

small weights this relationship was one of direct proportionality but subsequently fell away until, when the weight exceeded 3 kg., the impact force was nearly constant, a result which may be connected with the rigidity of the solid body.

At the Glen Fruin Research Station, two techniques have been employed by the author for measuring the change of velocity when the solid hits the water: (a) high-frequency cinematography, which is in most cases best applied to determine the "added mass" as a unique figure for each case, with small projectiles of less than 1 lb. in weight\*; (b) an impact-force gauge or decelerometer of high natural frequency applied to a larger hemisphere (20 in. diameter) and capable of delineating the force-time curve accurately.

(a) This series was carried out with a number of hollow ebonite projectiles ( $\sigma=0.7$ ), 3 in. diameter, dropped freely or fired at speeds up to 125 ft/sec. from a large rubber catapult mounted over a glass-sided tank of water ( $2\frac{1}{2}$  feet square in base and 5 ft. deep). Illumination was by searchlight from above and photography by Fastax or Kodak high-speed camera (*c.* 2000 pictures/sec.). The heads

\* Aoki (1926) and Kreps had already used this method, but even for slow entries up to 3 m/sec., such as they used, their picture frequency (60 per sec.) seems inadequate.

of the projectiles were in the shape of a flat disc, a hemisphere, a 1:1 ogive and cones of semi-angles  $22\frac{1}{2}^\circ$  and  $45^\circ$ . Spheres of wood and of duralumin were also used in the free-fall experiments. The catapult could produce vertical and oblique entries.

The films were analysed and plotted on graph paper as displacement-time curves. Typical curves are given on figures 8 and 9. In the first method of analysis we ignore—even when we can measure—the rate of change of velocity and draw two straight lines on the displacement-time curves to represent the velocities before and after impact. The main impact is felt when the nose is 1 cm. or more below the water level, depending on the shape of the head.

Table 2 summarizes these measurements;  $m$  is expressed both as a fraction of  $M$  and as  $\lambda c^3$ , where  $c$  is the radius of the cylindrical (or spherical) portion of the head. (Thus the theoretical values of  $\lambda$  are 2.66 for the disc and 2.1 for the hemisphere.)

Table 2

Model head	$M$ (gm.)	Specific gravity $\sigma$	$\beta_0$ (deg.)	$V_0/V_1$	$m$ (gm.)	$\lambda_{40}$	$\lambda_4$
Hemisphere	725	0.73	90	1.2	145	2.7	1.8
			64	1.25	180	3.4	—
			35	1.3	220	4.1	—
Disc	620	0.57	90	1.5	310	6.0	4.0
			64	1.4	250	4.7	—
			35	1.3	185	3.6	—
$22\frac{1}{2}^\circ$ cone	620	0.57	90	1.15	95	1.8	1.5
			64	1.15	95	1.8	—
			35	1.2	125	2.3	—
$45^\circ$ cone	550	0.60	90	1.3	165	3.2	3.0
			64	1.2	110	2.0	—
			35	1.15	85	1.6	—
1:1 ogive	710	0.75	90	1.0	0	0.0	0.0
			64	1.05	35	0.6	—
			35	1.1	70	1.3	—

$M$ =mass of model ;  $\sigma$ =specific gravity ;  $\beta_0$ =entry angle ;  $m$ =added mass ;  
 $\lambda_{40}=\lambda$  at 40 m/sec. ;  $\lambda_4=\lambda$  at 4 m/sec.

It will be noted that the derived values of added mass for vertical entry at high speed are greater than those at low. Examination of the photographs showed that this difference was reflected in the amount of water which was able to get away after impact in the splash. The flat disc, of course, produces a large splash and has a correspondingly high value (compared with theory) for  $\lambda$ .

Whether one regards this apparent variation of added mass with speed as significant depends on the attitude one adopts to this method of analysis. It must be again emphasized that "added mass" is rather an academic concept and, as figures 8 and 9 show, difficult to apply in practice, owing to the uncertainty in sighting the straight line which is to give the "velocity just after impact". It is indeed only on the basis of an insignificant drag that one can apply this idea.

It is rather surprising that the ogive enters vertically with inappreciable deceleration until drag begins to be felt.



Considering the results for cones it appears that, within the limits of experimental accuracy, a given cone experiences its impact at the same depth for all entry speeds. The greater the angle of the cone, the nearer to the vertex does this point occur.

(b) The projectile for this series of experiments was a hollow hemisphere of laminated plywood 20 in. in diameter (plate II, figure 10) with the impact gauge bolted rigidly to the inside. A lid prevented entry of water. The tare weight was 24 lb., but lead masses could be bolted to the inside to increase it to 46 lb. Calculation from (5) showed that the peak deceleration could be expected at an immersion of less than half an inch, equivalent to 5 msec. at 8 ft./sec. It was therefore necessary to use an accelerometer of quick response if the peak were to be truly recorded. After some early attempts with purely mechanical gauges, use was made of an electronic instrument developed by the Instrument Department of the Royal Aircraft Establishment from one described by Brookes-Smith and Colls (1939). This consists of a small electrical capacitor, one plate of which is rigidly attached to the structure while the other, in the form of a diaphragm, carries a free load and thus forms the spring + mass element of the accelerometer.

Accelerations produce relative changes in the separations of the plates, and the resulting change in capacitance is used to modulate an oscillatory circuit, which in turn causes movement of the electron spot on the screen of a cathode-ray oscillograph. The motion of the spot is recorded by a camera with continuously moving film.

The gauge had a natural frequency of about 900 c/sec., but filters could be incorporated to cut out the natural oscillations. At a preliminary trial the hemisphere was dropped from a small height three times in succession, the conditions of recording being (a) no filter, (b) filter partially applied, (c) oscillation just damped out. Figure 11 shows the corresponding records, on which the relative maxima of the smoothed curves are (a) 2.6, (b) 2.5, (c) 2.0. In order not to lose a considerable proportion of the true deflection, condition (b) was adopted throughout the remaining trials.

The characteristics of the filter were known. The cut-off was zero at 50 c/sec., and at 100 c/sec. had reached 20% with the full filter applied. It will be noticed in the force-time records (figures 12-14) that the peak was reached in 3.5 to 10 msec., corresponding to quarter-cycles of frequencies 60 to 25 c/sec. Over this range the correction for reduced response by the inclusion of the filter could be neglected.

Calibration was effected by noting the difference between the zero position of the spot on the film with the sphere at rest and that in free fall, set equal to 1g. and confirmed by the addition of known masses to the accelerometer diaphragm. Time marks were given by a 100 c/sec. fork.

The impact was photographed, as before, by Fastax camera.

The experimental records, whether by accelerometer or by camera, are obtained in terms of time and not depth of immersion, as in the theory. In order, then, to compare with theory, velocity-time curves are derived from the photographic records, and these are used to convert the time base of the oscillograph records into depths of immersion. This "correction for drag"—as it in fact amounts to—makes little difference to that value which one would have obtained by assuming the velocity had remained  $V_0$  up to the instant of maximum force. Thereafter drag causes a progressive discrepancy between the actual and the theoretical force-time curves.

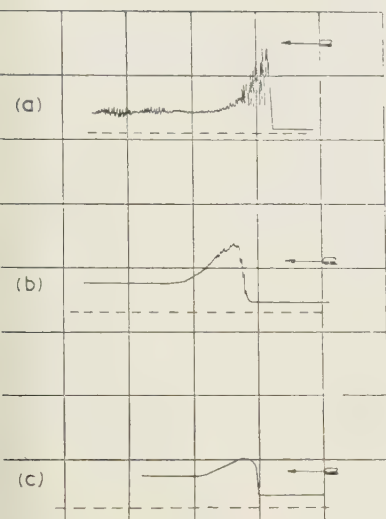


Figure 11. Trial deceleration records under three conditions: no filter (a); partial filter (b); critically damped (c).

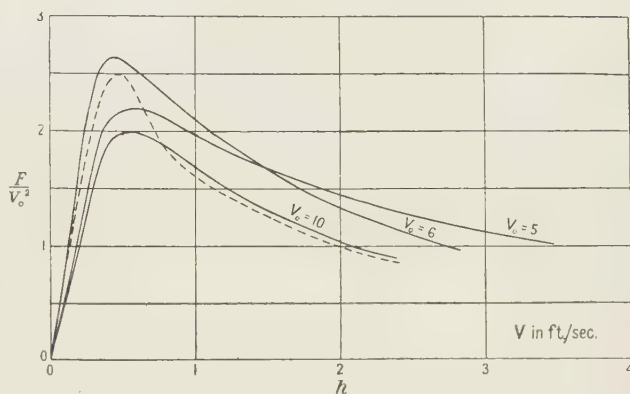


Figure 12. Impact of hemisphere (mass 24 lb.): force for unit entry velocity plotted against depth of immersion.

Typical curves for the 24-lb. mass when dropped from 6 in., 12 in. and 24 in. are shown in figure 12 and for the 46-lb. mass in figure 13. By comparing these with those derived from (5) (which are shown by broken lines) it appears that the von Kármán hypothesis gives good agreement with practice at least up to the instant of maximum impact.

As the ciné-camera was provided with a time base it is possible to derive acceleration-time records. The accuracy of this alternative method depends in the main on the frequency of the pictures in relation to the maximum deceleration. In figure 14 are shown two of the drops as interpreted from the camera records at 2000 frames/sec. To get a film record comparable in accuracy with the gauge record a picture frequency of double this would have been desirable.

The sphere involves a comparatively gentle rise to the maximum force, and with such shapes and a convenient picture frequency the photographic method is

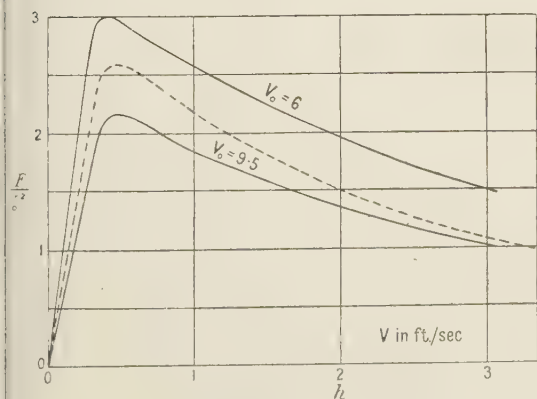


Figure 13. Impact of hemisphere (mass 46 lb.): force for unit entry velocity plotted against depth of immersion.

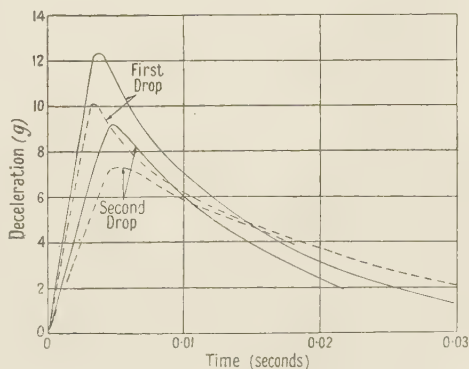


Figure 14. Impact of hemisphere (mass 24 lb.): comparison of camera record (full lines) and decelerometer record (broken lines).

suited to the deduction of impact forces. For sharp impacts the requisite rapidity is at present unattainable. Attempts to analyse the photographs of the impact of a disc in this way failed. At the other extreme of a finely pointed body, as already noted, the deceleration is too small to detect.

#### § 4. RICOCHET OF A SPHERE

In order to study the mechanism of ricochet and the form of cavity associated with entry at glancing angles a number of shots were made by firing 3 in. ebonite and duralumin spheres from the catapult, and 1 in. steel spheres from a gun, into the Glen Fruin tank. This permitted a water trajectory of about 20 ft. which could be photographed in two sections by ciné-cameras running at a speed of 200 pictures per second. Entry speeds ranged up to 360 ft/sec. The trajectories and displacement-time curves were plotted, and entry and exit angles ( $\beta_0, \beta_1$  radians) and velocities ( $V_0, V_1$ ), if ricochet occurred, were noted and the mean drag and lift coefficients between make-and-break contact over the path  $s$  were calculated using the formulae

$$C_D = (3.05\sigma d/s) \log(V_0/V_1), \quad \dots\dots(7)$$

$$C_D = 1.33\sigma d(\beta_0 + \beta_1)/s. \quad \dots\dots(8)$$

In another experiment the 20 in. wooden hemisphere, with its electrical accelerometer attached, was allowed to "glide" on to the water in order that the

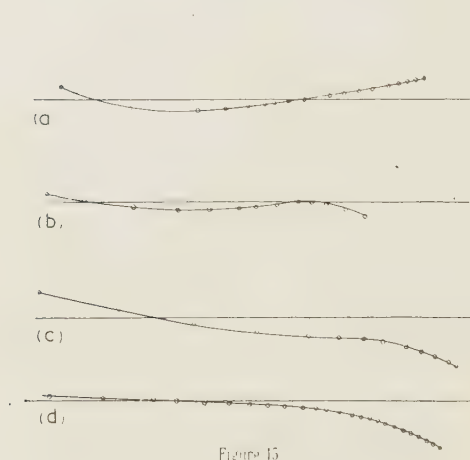


Figure 15.

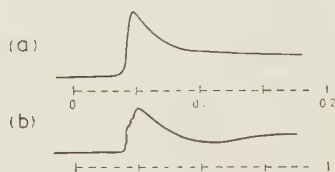


Figure 17.

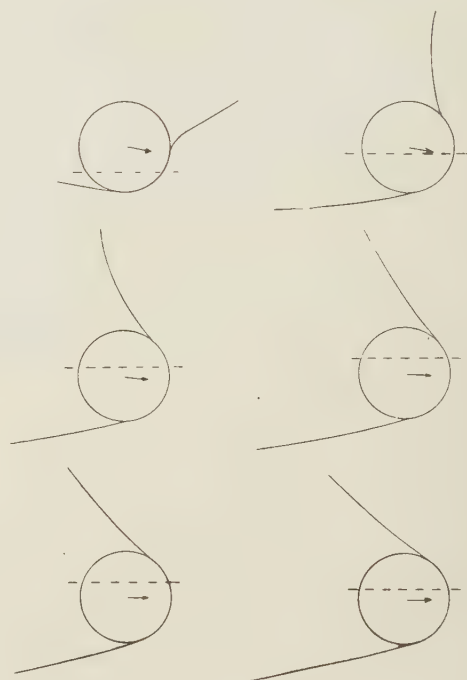


Figure 16.

Figure 15. Types of trajectory at glancing entry, the circles showing successive positions of the solid.

Figure 16. Water-surface shapes round spheres at glancing entry, the dotted lines indicating water level before being disturbed.

Figure 17. Decelerometer records, entry at  $90^\circ$  (a), at  $28^\circ$  (b) to horizon.



vertical component of force on a sphere entering obliquely could be measured. This entry was also photographed.

From all the photographs the shape of the splash and the wetted areas at different epochs were noted.

One may distinguish four types of trajectory as the entry angle is increased. Examples of these are shown in figure 15: (a) definite ricochet with angle of exit somewhat less than angle of entry; (b) break-surface often followed shortly by re-entry; (c) flattening-out and continuing on a straight path for a certain distance; (d) continuing straight ahead, then diving. (In the figure the dots represent positions on successive frames of the film, and so enable the deceleration to be judged.) The data for those shots which were capable of analysis are set out in table 3.

Table 3

No.	Sphere, <i>d</i> and $\sigma$	Velocity in path, (ft./sec.)		Angle to water surface (deg.)		Path length (in.)	Max. depth (diam.)	$C_D$	Mean $C_L$
	Dural	$V_0$	$V_1$	$\beta_0$	$\beta_1$	$S$			
1	3'', 2.7	100	50	7½	4½	50	0.5	0.15	0.045
2	"	120	33	10	6	60	0.5	0.23	0.055
3	"	100	53	9½	4	35	0.75	0.20	0.076
4	"	130	65	7½	6	55	0.75	0.14	0.042
6	"	100	65	7	5	42	—	0.11	0.052
15	"	147	52	9	10½	84	0.75	0.13	0.048
16	"	120	30	5½	4½	120	1.0	0.12	0.015
17	"	100	25	6	9	90	1.0	0.17	0.028
23	"	135	67*	8½	(0)*	60*	3.5	0.12	0.027
	Steel								
32	1'', 7.8	205	55*	7	(0)*	72*	2.0	0.19	0.013
36	"	210	140	8	4	66*	1.0	0.06	0.033
37	"	310	140	7½	4	60	0.5	0.14	0.035
38	"	330	140	6½	5	30	0.75	0.30	0.062
39	"	150	50*	11½	—	54*	—	0.21	—
40	"	270	80*	6½	(0)*	100*	1.8	0.13	0.012
42	"	300	65*	6	—	72*	1.5	0.22	—
43	"	360	55*	5	(0)*	76*	1.5	0.25	0.012
	Ebonite								
29	3'', 1.1	135	35	12½	10	160	1.25	0.04	0.011
47	"	155	58	17	11	55	1.25	0.08	0.036
48	"	155	37	14	14	48	1.5	0.13	0.043
61	"	142	56	11½	3½	42	0.7	0.10	0.027
70	"	135	16	6	6	54	0.8	0.17	0.018
67	"	142	—	12	—	—	—	—	—
69	"	140	—	12½	—	—	—	—	—

\* Notes: Shot 23 flattened in 60''; 32 flattened in 72''; 39 straightened out; 40 flattened in 100''; 42 straightened out; 43 flattened in 76''; 67 and 69 broke surface and re-entered.

Besides the shots which were photographed and completely analysed, some other visual observations of shots at various entry angles were made, merely to see whether the projectile broke surface or remained submerged. By grouping these observations, the following values of the critical angles for ricochet (which did not vary significantly with speed) were deduced: steel ( $\sigma=7.8$ ) 6°, dural ( $\sigma=2.7$ ) 9°, ebonite ( $\sigma=1.1$ ) 15°.

These results agree with some early observations of de Jonquières (1883) on steel spheres in that the product of the critical angle and the square root of the specific gravity is approximately constant.

From the photographs a series of tracings of the shape of the water surface at equal steps along the water path have been made. Figure 16 shows a typical set. It will be noted that the wetted perimeter forms a circle whose plane is inclined at less than  $90^\circ$  to the direction of motion, so that the reaction of the water has a component producing the lift. The water is able to do this provided the cavity does not reach its ultimate "submerged" shape, with the plane of wetting normal to the trajectory, before the sphere loses speed.

One might try to apply Newton's hypothesis to predict the resistance coefficients in the cavity stage by integrating  $\cos^2 \phi \cdot \delta S$  over the wetted surface ( $\delta S$  being an element of the surface whose normal makes an angle  $\phi$  to the trajectory) and resolving the resistance into components parallel and perpendicular to the direction of motion, but, as one would expect, such deduced values of  $C_D$  and  $C_L$  are much higher than the mean values calculated from (7) and (8); (0.45 and 0.045 in place of 0.12 and 0.027 respectively). Naturally, the drag coefficients deduced from the trajectory in oblique entry fall below that (0.34) appropriate to vertical entry of the sphere.

Figure 17(b) shows a decelerometer record for the entry of the 20-in. wooden hemisphere at  $28^\circ$  to the water surface with a vertical component of velocity ( $V_0$ ) of 6 ft/sec. The maximum values of  $F/V_0^2$  in the vertical and inclined entries were 2.25 and 1.5 respectively. While the rise to the peak is less sharp in the glide, the deceleration falls off at about the same rate in the two cases. Apparently forward momentum produces a "cushioning" of the water and a lifting force even in the short time that elapses before the maximum impact (in a vertical drop) is reached.

## § 5. FULL-SCALE APPLICATIONS OF IMPACT EXPERIMENTS

Fundamental experimental work on the impact of solids on water has two principal applications: (i) in ballistics, to the passage of projectiles from air into water; (ii) in aeronautics, to the landing of seaplanes.

The work described herein had principally the first application in view. Although the speeds and sizes of projectiles in practice are mostly greater than those employed in these experiments, the considerable range of these variables covered has indicated, for the sphere, that a model to full-scale conversion may be applied on a Froude number basis, where air-to-water ballistics is concerned. The underwater trajectory of longer projectiles which, in the cavity stage, involves moments set up by tail forces is another problem to which much research has been devoted.

The slow motion of the large hemisphere into water is more concerned with the second application. The theories of von Kármán and Wagner were in fact devised with this object in view, the keel of the boat being idealized into a shallow wedge for this purpose. Although it should be possible, using high-speed ciné-photography, to study impact forces on full-sized seaplanes dropped on to water, as far as the author knows this has never been done. The seaplane designer is more concerned with the local stresses set up at the touch-down, and these have been studied up to the present by observing pressure gauges let into various places on the

keel and flush with its surface. Two reports by Jones *et al.* (1934, 1937) describe measurements of this type using mechanical gauges. Recently these have been repeated using the electronic gauge as applied to the hemisphere in the present work.

#### ACKNOWLEDGMENTS

The author thanks the Director of the Royal Aircraft Establishment for permission to publish this work. He also acknowledges his indebtedness to a number of colleagues of the R.A.E. for their willing assistance, in particular to Mr. D. D. Hardy, laboratory assistant at Farnborough, and to Mr. F. P. Mayo, technical assistant at Glen Fruin.

#### REFERENCES

- AOKI, T., 1922, *J. Coll. of Engng., Tokyo*, **11**, 10 ; 1926, *Ibid.*, **16**, 4, **17**, 4.  
 BAUER, W., 1926, *Ann. Phys., Lpz.*, **82**, 1014.  
 BELL, G. E., 1924, *Phil. Mag.*, **48**, 753.  
 BROOKES-SMITH, C. H. W., and COLLS, J. A., 1939, *J. Sci. Instrum.*, **16**, 361.  
 VON KÁRMÁN, TH., 1930, *N.A.C.A. Tech. Note* 32.  
 KREPS, R. L., 1943, *N.A.C.A. Tech. Mem.* 1046.  
 JONES, E. T., and DAVIES, W. H., 1934, *Aero. Res. Commn. R. and M.* 1638.  
 JONES, E. T., DOUGLAS, G., STAFFORD, C. E., and CUSHING, R. K., 1937, *Aero. Res. Commn. R. and M.* 1807.  
 DE JONQUIÈRES, E., 1883, *C.R. Acad. Sci., Paris*, **97**, 1278.  
 LEHMANN, K. O., 1934, *Ann. Phys., Lpz.*, **21**, 533.  
 McMILLEN, J. H., 1945, *Phys. Rev.*, **68**, 198.  
 MALLOCK, A., 1918, *Proc. Roy. Soc. A*, **95**, 138.  
 PABST, W., 1931, *Z. Flugtechnik*, **22**, 193.  
 RAMSAUER, C. (and DOBKE, G.), 1927, *Ann. Phys., Lpz.*, **84**, 697.  
 SCHIFFMAN, M., and SPENCER, D. C., 1947, *Quart. Appl. Maths.*, **5**, 270.  
 TREY, F., 1933, *Phys. Z.*, **34**, 494.  
 WAGNER, H., 1932, *Z. angew. Math. Mech.*, **12**, 193.  
 WATANABE, S., 1929, *Sci. Pap. Inst. Phys. Chem. Res., Tokyo*, **12**, 251 ; 1930, *Ibid.*, **14**, 153 ; 1934, *Ibid.*, **23**, 118, 202, 249.  
 WORTHINGTON, A. M., 1877, *Proc. Roy. Soc.*, **25**, 261 ; 1897, *Philos. Trans. A*, **189**, 137.

## A Correction in Viscometry due to Varying Hydrostatic Head

By J. E. CAFFYN\*

The National Institute for Research in Dairying, University of Reading

\* Now Lecturer in Physics in The Durham Colleges, The University of Durham

**ABSTRACT.** The varying hydrostatic head in viscometers gives rise to a correction to the viscosity if the latter is calculated from the applied pressure only. This has been worked out in general and the special cases of viscometers with cylindrical and biconical bulbs and cylindrical bulbs with conical ends have been considered in detail.

### § 1. INTRODUCTION

THE author was led to consider this problem when designing a viscometer for the determination of the viscosity temperature coefficient of milk. v. Mises (1911) gives a correction for variable head for the Engler viscometer which takes account of the kinetic energy of the outflowing liquid.



Simeon (1914) calculates a correction for the Ostwald type viscometer involving the logarithm of the initial and final liquid head driving the fluid through the capillary of the viscometer. Bingham, Schlesinger and Coleman (1916) give a similar treatment for the simple case of a capillary tube connected to two cylindrical bulbs and extend it to the case where each bulb is made up of two cylinders of different radii. Lidstone (1922a, b, c) deduces a correction for the case considered by Bingham *et al.*, but takes into account the kinetic energy of the liquid. This leads to a formula for the viscosity which can only be evaluated by succession approximation. Bridgman (1927) deduces a similar result, but points out that it is only necessary to use the correction to the pressure due to variable head, and in so far as the latter affects the kinetic energy correction, it is a correction to a correction and can be neglected.

Barr (1924), in discussing Lidstone's viscometer, gives a correction to the pressure arising from variable head for the case of spherical reservoirs without giving the derivation.

Barr (1935) has also given equations for the variable head correction in viscometry and the expansion of the logarithmic correction factors for certain cases. He considered the sphere discharging into air, a pair of opposed cones, a biconical bulb discharging into a cylinder and a cylindrical bulb with conical ends discharging into a cylinder for special values of the parameters.

It appears that no attempt has been made to consider the general case of variable head. It is proposed, therefore, to investigate the case of a viscometer whose bulbs are volumes of revolution. The kinetic energy correction will be neglected in this treatment.

## § 2. GENERAL CASE

Consider a viscometer shown diagrammatically in figure 1. Let the bulbs A and A' be connected by a capillary tube of radius  $R$  cm. and length  $L$  cm. Let a liquid of viscosity  $\eta$  and density  $\rho$  be driven from A to A' by an applied pressure  $p_0$ . The liquid level at any instant in A is  $h$  cm. from an arbitrary

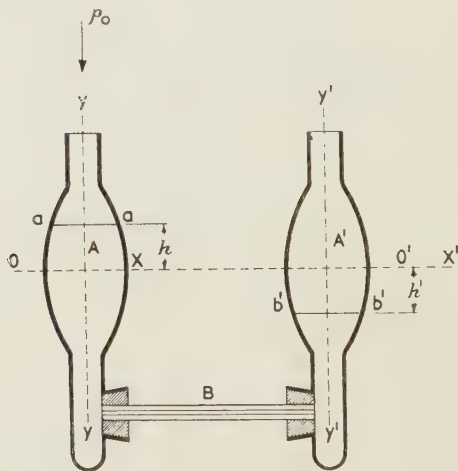


Figure 1.  
aa, b'b': initial liquid level.

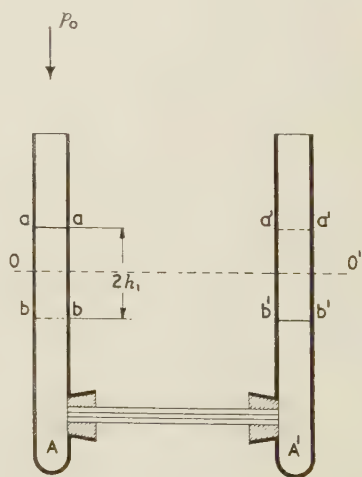


Figure 2.  
aa, b'b': initial liquid level.  
bb, a'a': final liquid level.

level  $OO'$  and the corresponding height of the liquid level in  $A'$  is  $h'$ . Let the viscometer bulbs  $A$  and  $A'$  be volumes of revolution generated by rotating the curves  $x=f(h)$  and  $x'=f'(h')$  about the axes  $YY$  and  $Y'Y'$  respectively.  $f(h)$  and  $f'(h')$  need not necessarily be the same functions of  $h$  and  $h'$ .

Then if we apply Poiseuille's law in its differentiated form to the liquid flowing through the capillary tube  $B$ ,

$$dV(h)/dt = \pi R^4 p(h) / 8\eta L ; \quad \dots\dots (1)$$

$V(h)$ , the volume of liquid flowing through  $B$ , and  $p(h)$ , the pressure, driving the liquid through  $B$ , are both functions of  $h$ .

If the liquid level in the bulb  $A$  falls  $dh$  in time  $dt$ , then

$$dV(h) = \pi [f(h)]^2 dh. \quad \dots\dots (2)$$

Therefore, writing (1) in the form

$$(dV(h)/dh) \cdot (dh/dt) = \pi R^4 p(h) / 8\eta L, \quad \dots\dots (3)$$

and substituting from (2), we have

$$\pi [f(h)]^2 (dh/dt) = \pi R^4 p(h) / 8\eta L. \quad \dots\dots (4)$$

The function of  $p(h)$  is given in terms of  $h$  and  $h'$  by

$$p(h) = p_0 + g\rho(h - h'). \quad \dots\dots (5)$$

Substituting from (5) in (4), rearranging and integrating from  $h=h_i$ , the initial liquid level in  $A$ , to  $h=h_f$ , the final liquid level in  $A$ , we have

$$\int_{h_i}^{h_f} \frac{\pi [f(h)]^2 dh}{h_i p_0 + g\rho(h - h')} = \int_0^t \frac{\pi R^4 dt}{8\eta L}. \quad \dots\dots (6)$$

To solve (6) explicitly for the viscosity  $\eta$ , we must specify  $f(h)$  and know  $h'$  in terms of  $h$ . The latter can be determined from the fact that the volume of fluid leaving  $A$  must enter  $A'$ . Hence

$$\pi \int_{h_0}^h [f(h)]^2 dh = \pi \int_{h'}^{h'_0} [f'(h')]^2 dh', \quad \dots\dots (7)$$

where  $h_0$  and  $h'_0$  are convenient corresponding liquid levels in  $A$  and  $A'$ . The shape of the viscometer will determine the functions  $f(h)$  and  $f'(h')$ . Then with the specification of the initial and final liquid levels in the bulbs  $A$  and  $A'$ , the equations (6) and (7) give the solution to the problem.

### § 3. A VISCOMETER WITH CYLINDRICAL BULBS

A viscometer of this type is shown diagrammatically in figure 2. The bulbs have the same radius  $r$  cm. Since the initial and final liquid levels are equally displaced about  $OO'$ , equation (7) gives on integration  $h = -h'$ . Therefore equation (6) becomes

$$\pi r^2 \int_{-h_1}^{+h_1} \frac{dh}{-h_1 p_0 + 2g\rho h} = \frac{\pi R^4}{8\eta L} \int_0^t dt, \quad \dots\dots (8)$$

which on integration gives

$$\eta = \frac{\pi R^4 t p_1}{8LV \ln(p_0 + p_1)/(p_0 - p_1)}, \quad \dots\dots (9)$$

where  $p_1$  is the hydrostatic pressure due to a column of the liquid  $2h_1$  cm. high and  $V$  is the total volume of liquid passing through the capillary.

Expanding the logarithm in (9), we have

$$\eta[1 + c_1^2/3 + c_1^4/5 \dots] = \pi R^4 t p_0 / 8LV, \quad \dots\dots(10)$$

where  $c_1 = p_1/p_0$ . This shows the effective correction to the applied pressure due to the variable hydrostatic head. This result expressed as in equation (9) is the same as Bingham's. It is not difficult to modify this treatment for the case where the initial liquid level "aa" in A is not at the same horizontal level as the final liquid level "a'a'" in A'.

#### § 4. A VISCOMETER WITH BICONICAL BULBS

A viscometer of this type is shown diagrammatically in figure 3. The viscometer is filled so that the liquid level is bb and b'b' in the bulbs A and A'

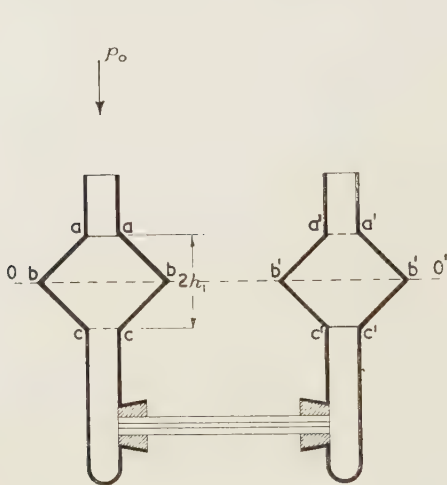


Figure 3.  
aa, c'c': initial liquid level.  
cc, a'a': final liquid level.

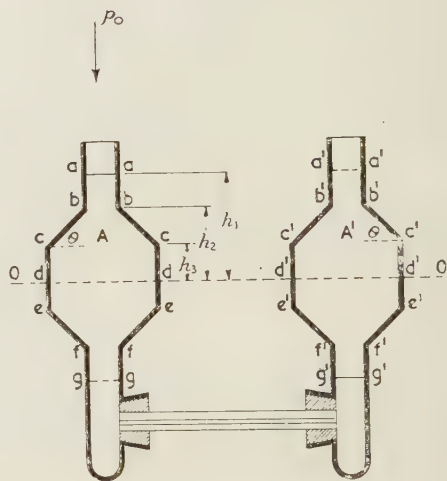


Figure 4.  
aa, g'g': initial liquid level.  
gg, a'a': final liquid level.

respectively, the bulbs being identical in all respects. The function  $f(h) = f'(h')$  takes slightly different forms for positive  $h$  and negative  $h$ , and is given by

$$f(h) = r_2 - h \tan \theta, \quad h \text{ positive}; \quad f(h) = r_2 + h \tan \theta, \quad h \text{ negative},$$

where  $r_2$  is the radius of the bulb at bb and  $\theta$  is the angle cb makes with the horizontal. To integrate (6) we must divide up the range of integration, and we get

$$\pi \int_0^{+h_1} \frac{(r_2 - h \tan \theta)^2 dh}{p_0 + g\rho(h - h')} + \pi \int_{-h_1}^0 \frac{(r_2 + h \tan \theta)^2 dh}{p_0 + g\rho(h - h')} = \frac{\pi R^4}{8\eta L} \int_0^t dt. \quad \dots\dots(11)$$

Since the bulbs are identical, equation (7) will give  $h = -h'$  for all values of  $h$ . Therefore equation (11) becomes

$$\pi \int_0^{+h_1} \frac{(r_2 - h \tan \theta)^2 dh}{p_0 + 2g\rho h} + \pi \int_{-h_1}^0 \frac{(r_2 + h \tan \theta)^2 dh}{p_0 + 2g\rho h} = \frac{\pi R^4}{8\eta L} \int_0^t dt.$$



On carrying out the integrations and making some algebraic simplification, we have

$$\left[ \frac{\pi r_2^2}{2g\rho} + \frac{\pi p_0^2(r_2 - r_1)^2}{8g^3\rho^3 h_1^2} \right] \ln \frac{p_0 + 2g\rho h_1}{p_0 - 2g\rho h_1} + \frac{\pi r_2(r_2 - r_1)p_0}{2g^2\rho^2 h_1} \ln \frac{p_0^2 - 4g^2\rho^2 h_1^2}{p_0^2} \\ + \frac{\pi p_0(r_2 - r_1)^2}{2g^2\rho^2 h_1} = \frac{\pi R^4 t}{8\eta L},$$

where  $r_1$  is radius of the bulb at aa, etc.

Treating this in the same way as previously, we have

$$\frac{\pi R^4 p_0 t}{8VL} = \eta \left[ 1 + \frac{c_1^2}{10} \left( \frac{1 + 3w + 6w^2}{1 + w + w^2} \right) + \text{terms in } c_1 \text{ of higher powers than the second} \right], \quad \dots\dots(12)$$

where  $w$  is ratio of the radius of the bulb at "aa" to the radius at "bb" and  $c_1$  has its usual meaning. As in the previous case, suitable modification of the treatment will give the solution for the case when the centres of the bulbs "bb" and "b'b'" do not lie in the same horizontal plane.

#### § 5. A VISCOMETER CONSISTING OF CYLINDRICAL BULBS WITH CONICAL ENDS

This shape of bulb is shown diagrammatically in figure 4 and is approximately similar to many industrial viscometer bulbs. As previously, we will consider the case of identical bulbs, i.e.  $f(h) = f'(h')$ , and hence  $h = -h'$  for all values of  $h$ . The function  $f(h)$  is defined in the ranges as follows:

$$f(h) = r_1, \quad h_2 < h < h_1; \quad f(h) = r_2, \quad -h_3 < h < h_3; \quad f(h) = r_1, \quad -h_2 < h < -h_1$$

$$f(h) = r_1 + (h_2 - h) \tan \theta, \quad h_3 < h < h_2; \quad f(h) = r_1 + (h_2 + h) \tan \theta, \quad -h_3 < h < -h_2,$$

where  $r_1$  and  $r_2$  are the radii of the bulbs at "aa" and "dd" respectively. Splitting up the range of integration, substituting the appropriate values of  $f(h)$  in equation (6) and integrating, we have

$$\frac{\pi R^4 t}{8\eta L} = \frac{\pi r_1^2}{2g\rho} \ln \left[ \frac{p_0 + p_1}{p_0 + p_2} \cdot \frac{p_0 - p_2}{p_0 - p_1} \right] + \frac{\pi r_2^2}{2g\rho} \ln \frac{p_0 + p_3}{p_0 - p_3} \\ + \frac{\pi(r_1 + h_2 \tan \theta)^2}{2g\rho} \ln \left[ \frac{p_0 + p_2}{p_0 + p_3} \cdot \frac{p_0 - p_3}{p_0 - p_2} \right] \\ + \frac{\pi p_0 \tan \theta (r_1 + h_2 \tan \theta)}{2g^2\rho^2} \ln \left[ \frac{p_0 + p_2}{p_0 + p_3} \cdot \frac{p_0 - p_2}{p_0 - p_3} \right] \\ + \frac{p_0^2 \pi \tan^2 \theta}{8g^3\rho^3} \ln \left[ \frac{p_0 + p_2}{p_0 + p_3} \cdot \frac{p_0 - p_3}{p_0 - p_2} \right] - \frac{\pi p_0 \tan^2 \theta (h_2 - h_3)}{2g^2\rho^2}, \quad \dots\dots(13)$$

where  $p_1$ ,  $p_2$  and  $p_3$  are the pressures due to liquid columns  $2h_1$ ,  $2h_2$  and  $2h_3$  cm. high respectively.

If we expand the logarithms in equation (13) and rearrange, we can write equation (13) in the form

$$\eta \left[ 1 + \frac{V_1}{V} (c_1^2 + c_1 c_2 + c_2^2) + \frac{V_3}{3V} (c_3^2) + \frac{V_2}{10V} \left\{ \frac{(6c_3^2 + 3c_3 c_2 + c_2^2) + w(3c_3^2 + 4c_3 c_2 + 3c_2^2) + w^2(6c_2^2 + 3c_2 c_3 + c_3^2)}{1 + w + w^2} \right\} + \text{higher terms} \right] = \frac{\pi R^4 p_0 t}{8VL}, \quad \dots (14)$$

where  $V_1$  is the volume "aabb" + "ffgg",  $V_2$ , the volume "bbcc" + "eeff",  $V_3$ , the volume "ccce",  $c_1 = p_1/p_0$ ,  $c_2 = p_2/p_0$ ,  $c_3 = p_3/p_0$ ;  $V = V_1 + V_2 + V_3$ , and the other symbols have the same meaning as previously. Equations (14) and (12) reduce to equation (10) on substituting  $w = 1$ ,  $V_1$  in terms of  $h_1$ , etc.; this provides a convenient check on the algebra.

## § 6. DISCUSSION

In the table the correction to the viscosity, as calculated from the applied pressure only, is tabulated against  $c_1$  for the three types of viscometer considered above with suitable arbitrary values of the constants. The value of  $c_1$  must always be less than one, otherwise the logarithmic expansion would not be justified. This means physically that the applied pressure must be greater than the maximum hydrostatic head, which is necessary if the experiment is to end in a finite time.

### Correction factors to $\eta$

$c_1$		0.200	0.100	0.050	0.033	0.025
Correction factor	{	1.0133	1.0033	1.0008	1.0004	1.0002
for viscometer		1.0020	1.0005	1.0001	< 1.0000	< 1.0000
shown in		1.0052	1.0013	1.0003	1.0002	1.0001

Values for viscometer constants used in determining the corrections above:  $w = 2/5$ ;  $c_2 = 11c_1/12$ ;  $c_3 = 2c_1/3$ ;  $V_1/V = 1/30$ ;  $V_2/V = 1/5$ ;  $V_3/V = 1/10$  and  $\theta = 45^\circ$ .

## ACKNOWLEDGMENT

The work described above was part of a research programme carried out at the National Institute for Research in Dairying under a grant from the Agricultural Research Council.

## REFERENCES

- BARR, G., 1924, *J. Soc. Chem. Ind.*, **43**, 29; 1935, *J. Chem. Soc.*, **17**, 94.  
 BINGHAM, E. C., SCHLESINGER, H. I., and COLEMAN, A. B., 1916, *J. Amer. Chem. Soc.*, **38**, 27.  
 BRIDGEMAN, P. W., 1927, *Proc. Amer. Acad. Arts Sci.*, **62**, No. 8, 187.  
 LIDSTONE, F. M., 1922 a, *Phil. Mag.*, **43**, 354; 1922 b, *Ibid.*, **43**, 1024; 1922 c, *Ibid.*, **44**, 553.  
 V. MISES, F., 1911, *Phys. Z.*, **12**, 812.  
 SIMEON, F., 1914, *Phil. Mag.*, **27**, 38.

# The Radial Variation of the Earth's Magnetic Field

By S. K. RUNCORN

The Physical Laboratories, The University of Manchester;

With an Appendix by S. CHAPMAN

The Queen's College, Oxford

*Communicated by P. M. S. Blackett; MS. received 30 April, 1948*

**ABSTRACT.** It is shown that Core and Distributed theories of the Earth's Magnetic Field predict different variations of field intensity with depth. Whereas on core theories both the horizontal and vertical intensities increase with depth according to an inverse cube law, on a distributed theory such as the one recently put forward by Blackett we find, with reasonable assumptions, that while the vertical intensity should increase for small depths as an inverse cube law, the horizontal intensity should decrease. The difference between the theories is even more marked deep inside the Earth. It is also suggested that if the variation with depth experiments gives a positive result in favour of distributed theories, then experiments on the magnetic effect of gorges in the Earth's surface might throw further light on the mechanism of the phenomena.

## § 1. INTRODUCTION AND SUMMARY

THE theories of the main magnetic field of the Earth may be divided roughly into two groups.

(i) *Core theories*—those which attribute the field to processes taking place in or properties possessed by the central core of the earth and

(ii) *Distributed theories*—those which attribute the field to a process or property associated with the whole volume of the Earth. Such a distributed theory is that due to Blackett (1947) who, by noting the proportionality of magnetic moment and angular momentum for the Earth, the Sun and a star (78 Virginis), has lately revived an old idea of Schuster and H. A. Wilson and tentatively postulates the Earth's main magnetic field to be an example of a universal property of rotating matter. Bullard pointed out that it might be possible to decide between the core theories and a distributed theory as their laws of variation of field with depth would be different. This paper develops this idea and compares the law of variation with depth for the two groups of theories.

## § 2. CORE THEORIES OF THE EARTH'S MAIN MAGNETIC FIELD

The theories which have been put forward at various times to explain the Earth's magnetism have been summarized by Chapman and Bartels (1940), by J. A. Fleming and others (1940), and more recently by Blackett (1947).

Seismological evidence shows that the Earth consists of a solid crust and a liquid core of diameter about 2000 miles. The mean density of the liquid core (12) is the density that iron and nickel would have at the pressures obtaining in the core. Thus it is thought that the core might consist of iron or iron-nickel. As the effect of very high pressure on the Curie point of iron is not known the hypothesis that the Earth's core is permanently magnetized to an intensity of about 0.6 gauss cannot be excluded completely. (If the whole of the Sun was uniformly magnetized the intensity of magnetization required to explain its observed field would have to be about 12 gauss). Nippoldt and Bartels (see Fleming 1940) have suggested that the entire field has its origin in ferromagnetism



of the outer crust down to the point where the temperature has increased to the Curie point for iron. This involves attributing an average intensity of magnetization of the crust of between 1 and 6 gauss. If this occurs it must lie below the depths normally accessible to observation and hence the theory would give the same variation with depth as a core theory.

The field of the Earth has also been attributed to electric conduction currents. However, Lamb showed that the decay of such currents in the earth would be far too rapid to attribute them to a primeval field. But there are no known mechanical motions or chemical reactions in the outer crust of the Earth which would maintain such currents, hence Elsasser (1939, 1941) and Frenkel (1945) have postulated processes in the central core of the Earth resulting from its fluid state, e.g. convective motions leading to thermoelectric E.M.F.s which might maintain currents sufficient to explain the Earth's magnetic field.

### § 3. THE RADIAL VARIATION FOR CORE THEORIES

If the magnetic field originated in the central core of the earth or below the deepest point at which our measurements can reach, as in the theories listed in § 2, the field would vary inversely with the cube of the distance from the centre of the Earth.

If  $R$  is the radius of the Earth,  $H^0$  is the horizontal intensity,  $H^r$  is the vertical intensity, suffix  $d$  refers to measurements at depth  $d$  and suffix 0 to measurements at the surface, we have at co-latitude  $\theta$

$$H_d^r = H_0^r(1 + 3d/R); \quad H_d^0 = H_0^0(1 + 3d/R) \text{ for small } d/R.$$

Thus in Great Britain we would expect the horizontal intensity to increase by  $12\gamma$  ( $1\gamma = 10^{-5}$  gauss) and the vertical intensity by  $26\gamma$  at a depth of 4000 ft. (which is the depth of the deepest mine in this country). All measurements at depth are assumed to be made in filamentous cavities parallel to the component of the field being measured, to avoid the effects due to the susceptibility of the surrounding rocks, which usually lies between  $10^{-6}$  and  $10^{-3}$  gauss.

### § 4. THE DISTRIBUTED THEORIES OF THE EARTH'S MAIN MAGNETIC FIELD

The simplest distributed theory is to assume that the Earth possesses a uniform negative volume charge of  $4 \times 10^{-4}$  E.S.U./cm<sup>3</sup> or a surface charge of  $5.1 \times 10^4$  E.S.U./cm<sup>2</sup>. However, these involve enormously strong electric fields at the surface of the Earth of the order of  $10^8$  volt/cm. Moreover, as Schuster (1912) points out, such a theory would give a field radically different from that of a dipole for an observer on the Earth's surface. Sutherland (1900) overcame both of these objections by suggesting that the Earth might possess a negative surface charge and a positive volume charge sufficient to neutralize the external electric field. Such a theory involves an electric field of  $10^8$  volt/cm. inside the Earth. Sutherland (1903) then proceeded to show that if the charge separation took place at the atomic or molecular level rather than macroscopically it would be necessary to assume that the atomic charges separate by amounts of the order of  $10^{-8}$  cm. Schlomka (1933) and Haalck (1937, 1938) work out theories on these lines, making assumptions as to the cause of the charge separation.

Blackett (1947), on the basis of the most recent measurements of the field of the Sun and 78 Virginis, tentatively puts forward the view that all massive

rotating bodies have associated with them a magnetic field which he assumes in the case of a spherical body to be, externally to the body, the field of a dipole situated at the centre directed along the axis of rotation of moment

$$P = -\beta U G^{\frac{1}{2}} / 2c, \quad \dots\dots(1)$$

where  $G$  is the gravitational constant,  $U$  the angular momentum,  $c$  the velocity of light, and  $\beta$  a constant of order unity. Such a theory implies that each particle of matter in the body makes a contribution to the magnetic field. And Blackett argues that owing to the failure of all classical attempts to provide an explanation of the formula, the law (1) may imply some new fundamental relation between electromagnetism and gravitation.

In addition to Blackett's hypothesis, a complete explanation of geomagnetism would have to postulate certain secondary mechanisms which would give rise to declination and secular variation in addition to the field components of higher harmonic orders (Elsasser 1941, Bullard, unpublished). In this paper such secondary effects will be ignored.

#### § 5. RADIAL VARIATION FOR DISTRIBUTED THEORIES

Since the deepest mines in the world are 6000 ft. deep, bore holes reach 14000 ft. in depth and the greatest depths in the oceans are of the order of 34000 ft., the determinations of the variation of the Earth's field with depth may only be carried out at depths small compared to the radius of the Earth. Let the magnetic moment of the Earth be  $P$  and let  $P_d$  be the magnetic moment of the surface shell  $S$  of thickness  $d$  inside which measurements are made. It will be assumed that the magnetic effects of concentric shells of the Earth are additive for distributed theories, and hence as the main magnetic field is that of a dipole the field of the shell  $S$  alone would be that of a dipole outside the sphere.

The potential of the isolated rotating shell for  $r > R$  would be

$$\begin{aligned} \phi_0 &= P_d \cos \theta / r^2, \text{ where } \theta \text{ is the co-latitude angle,} \\ &= (P_d / r^2) P_1 (\cos \theta), \text{ where } P_1 \text{ is the first zonal harmonic. } \dots\dots(2) \end{aligned}$$

Now the field within and without the shell may be represented by scalar potentials expanded in the form of series of zonal harmonic terms in their rôle as solutions of Laplace's equation:

$$\begin{aligned} \phi_1 &= I_n(r/R) P_n(\cos \theta) \text{ for } r < R, \\ \phi_0 &= E_n(R/r)^2 P_n(\cos \theta) \text{ for } r > R, \end{aligned}$$

where  $E_n$  and  $I_n$  are coefficients independent of  $r$  and  $\theta$ . Hence  $E_n = P_d/R^2$  for  $n=1$ , and  $E_n=0$  for  $n>1$ .

To determine the coefficients  $I_n$  it is necessary to insert a boundary condition. On classical magnetostatic theory there are two alternatives, the shell is to be regarded (A) as a virtual surface distribution of current in which case the radial magnetic induction passes continuously through the shell (Stratton 1941, §4.12) or (B) as a surface distribution of magnetic moment. In the absence of an explanation of formula (1) it is finally necessary to rely on the experimental determination of the variation of the components of the Earth's magnetic field with depth to determine the nature of the boundary condition. In this paper we will assume that (A) is the right boundary condition to use. Thus

$$I_1 P_1(\cos \theta) / R = -2(P_d / R) P_1(\cos \theta) \text{ and } I_n = 0 \text{ for } n > 1.$$

Thus we obtain the scalar potential inside a thin shell of matter of moment  $P_d$

$$\phi_i = -2(P_d/R)rP_1(\cos\theta). \quad \dots\dots(3)$$

Now the field intensities at the surface of the sphere which would remain if the outer shells were removed are

$$H^r = + \frac{2(P - P_d)}{(R - d)^3} \cos\theta \quad \text{and} \quad H^\theta = + \frac{(P - P_d)}{(R - d)^3} \sin\theta.$$

Now for small values of  $d/R$  the radial component of the field is continuous through the shell, hence the vertical field at depth  $d$  is  $H_d^r = H_0^r(1 + 3d/R)$  where  $H_d$  and  $H_0$  denote the field intensities at depth  $d$  and the surface of the Earth respectively.

Just inside the shell  $S$  the horizontal field  $H^\theta$  due to the shell is given by  $H^\theta = [(1/r)(\partial\phi_i/\partial\theta)]_{r=R} = 2P_d/R^3 \sin\theta$  and just outside the shell by

$$H^\theta = [(1/r)(\partial\phi_0/\partial\theta)]_{r=R} = -(P_d/R^3) \sin\theta.$$

Summing the field components we find that the horizontal component at depth  $d$  below the surface of the Earth is  $H_d^\theta = H_0^\theta(1 + 3d/R - 3P_d/P)$ . Measurements of the variation of the horizontal component with depth gives a direct measurement of the magnetic moment of the shell  $S$ .

## § 6. RADIAL VARIATION FOR BLACKETT'S FUNDAMENTAL THEORY

By the use of law (1) and boundary condition (A) the variation of the magnetic field throughout the Earth may be calculated.

We begin by assuming that the contribution ( $dP$ ) made to the total dipole by a shell of matter at radius  $a$  in the sphere may be obtained by differentiating the expression for  $P$

$$dP = \beta \frac{G^{\frac{1}{2}}}{2c} dU = \frac{4\pi}{3} \beta \frac{G^{\frac{1}{2}}}{c} \rho a^4 \omega da, \quad \dots\dots(4)$$

where  $da$  is the radial thickness of the shell. As relation (1) is an empirical one it is impossible to decide whether the value of  $\rho$  which enters into equation (4) is the mean density of the shell or not. In order to make the analysis quite general let it be the density of the shell weighted by a certain factor  $g(a)$  which depends on some property of the whole configuration, for example if the magnetic effect of a shell depend upon the gravitational field at that shell we find

$$dP = \frac{4\pi}{3} \beta \frac{G^{\frac{1}{2}}}{c} \rho(a)g(a)a^4 \omega da. \quad \dots\dots(5)$$

Thus relation (1) now becomes

$$P = \frac{4\pi}{15} \beta \frac{G^{\frac{1}{2}}}{c} R^5 \omega D(R), \quad \dots\dots(6)$$

where  $D(R) = \int_0^R \rho(a)g(a)a^4 da / \int_0^R a^4 da$ , a mean density weighted by the factor  $g(a)$ . By placing  $g(a) = 1$  we obtain the relation

$$P = \frac{4\pi}{15} \beta \frac{G^{\frac{1}{2}}}{c} kR^5 \omega \rho_m, \quad \dots\dots(7)$$

where  $k = I/I_0$  where  $I$  is the moment of inertia of a given centrally condensed sphere and  $I_0$  that of a sphere of the same radius and angular velocity and of



uniform density equal to the mean density of the centrally condensed sphere. The quantity on the right hand of equation (6) is a constant  $\beta G^{\frac{1}{2}} 2\mathbf{c}$  multiplied by the angular momentum of the sphere, and Blackett obtains values for  $\beta$  as given in table 1 for different astronomical bodies using experimental values of  $P$  and  $U$  and an assumed value for  $k$ . The uncertainties in the values of  $R$ ,  $\omega$  and  $P$  for the Sun and 78 Virginis do not allow us to decide exactly how density should enter into the formula (1), i.e. to determine the function  $g(a)$ , as the range of densities between the three bodies is rather small.

It is possible that the magnetic effect of the shell at radius  $a$  may depend upon the gravitational field at that shell, in which case the  $\rho$  in formula (3) will have to be replaced by a quantity dependent partly on the density of the shell itself and partly on the average density of the matter within the shell.

Table 1

	Average $\rho$	Values of $\beta$	
		Assuming uniform density	Inserting constant $k$
Earth	5.53	0.26	0.30
Sun	1.39	0.18	1.14
78 Virginis	0.4	0.19	1.16

Though we cannot assume that on a distributed theory the magnetic field is irrotational within the matter of the rotating body, we can assume that outside the shell of matter the magnetic field may be represented by a scalar potential. In order to calculate the field components at depth  $d$  we imagine the Earth divided into a thick shell bounded by the surfaces  $r=R$  and  $r=R-d$  and a sphere of radius  $R-d$ , the two being separated by an infinitesimal spherical shell free of matter. The part of the field components at depth  $d$  due to the sphere may be written down from (6) and the part due to the thick shell may be obtained by differentiating within the spherical shell free of matter the scalar potential at depth  $d$  due to the thick shell which is obtained by integrating the contributions from such elementary shells.

The potential at  $(r, \theta)$  for  $r < R-d$  due to a shell extending from  $r=R-d$  to  $r=R$  will be

$$-\frac{8\pi}{3} \beta \frac{G^{\frac{1}{2}}}{\mathbf{c}} \omega r \cos \theta \int_{R-d}^R \rho(a) g(a) a da,$$

where the integral will depend on the density of the surface rocks.

The field intensities at depth  $d$  may now be derived.

The radial component  $H_d^r = [\partial \phi_d / \partial r]_{r=R-d} - 2[P(R-d)/(R-d)^3] \cos \theta$ , where  $P(R-d)$  is the magnetic moment of the sphere radius  $R-d$  is

$$H_d^r = H_0^r \left[ \frac{D(R-d)}{D(R)} \left( 1 - \frac{d}{R} \right)^2 + \frac{5}{2} \frac{\Delta(d)}{D(R)} \left( 2 \frac{d}{R} - \frac{d^2}{R^2} \right) \right], \quad \dots \dots (8)$$

where  $\Delta(d) = \int_{R-d}^R \rho(a) g(a) a da / \int_{R-d}^R a da$ , a weighted surface density.

Similarly the horizontal component of the magnetic field at depth  $d$  is

$$\begin{aligned} H_d^\theta &= [\partial \phi_d / r \partial \theta]_{r=R-d} - P(R-d) \sin \theta / (R-d)^3 \\ &= H_0^\theta \left[ \frac{D(R-d)}{D(R)} \left( 1 - \frac{d}{R} \right)^2 - 5 \frac{\Delta(d)}{D(R)} \left( 2 \frac{d}{R} - \frac{d^2}{R^2} \right) \right]. \quad \dots \dots (9) \end{aligned}$$

For a density distribution not differing greatly from a uniform one

$$D(R-d) = D(R) = \rho_m \quad \text{and} \quad \Delta(d) = \rho_s,$$

where  $\rho_m$  and  $\rho_s$  are respectively the mean density of the Earth and the density of the surface rocks.

Equation (9) then becomes

$$H_d^0 = H_0^0 \{1 - (2 + 10 \rho_s/\rho_m)(d/R)\}, \quad \dots\dots(10)$$

which is the formula obtained by the author, communicated to and quoted by Hales and Gough (1947). It fits the case of the Earth reasonably well down to depths of 1 mile under land. As might be expected for a theory which assumes that the whole of the Earth is contributing to the magnetism,  $H^0$  should decrease with depth, while on the core theories it should increase with depth. Thus there emerges the possibility of being able to determine by variation with depth experiments which theory of the Earth's magnetism is true.

In Great Britain the various differences would be

$$\left. \begin{aligned} H_d^r - H_0^r &= +25 \gamma \text{ per } 4000 \text{ ft.} \\ H_d^0 - H_0^0 &= +11 \gamma \text{ per } 4000 \text{ ft.} \end{aligned} \right\} \text{core theory,}$$

$$\left. \begin{aligned} H_d^r - H_0^r &= +25 \gamma \text{ per } 4000 \text{ ft.} \\ H_d^0 - H_0^0 &= -23 \gamma \text{ per } 4000 \text{ ft.} \end{aligned} \right\} \text{distributed theory.}$$

Some preliminary measurements have been made by Hales and Gough (1947) on the suggestion of Dr. E. C. Bullard in South Africa and by Benson, Goldsack and Runcorn (see Chapman 1948) in Lancashire. These appear to support the distributed theory.

Let us now examine the exact formula of the field variation for  $g(a)=1$  for small depths.

In this case  $D(R) = \int_0^R \rho(a)a^4 da / \int_0^R a^4 da = k\rho_m$ , and for small  $d/R$ ,

$$\begin{aligned} \frac{1}{5} R^5 D(R) &= \int_0^{R-d} \rho(a)a^4 da + \frac{1}{5} \rho_s \{R^5 - (R-d)^5\} \\ R^5 D(R) &= (R-d)^5 D(R-d) + \rho_s \{R^5 - (R-d)^5\}. \end{aligned}$$

Then

$$\begin{aligned} H_d^r &= H_0^r \left[ \left(1 + \frac{3d}{R}\right) \left(1 - \frac{5d}{R} \frac{\rho_s}{k\rho_m}\right) + \frac{5}{k} \frac{\rho_s}{\rho_m} \frac{d}{R} \right] \\ &= H_0^r [1 + 3d/R] \text{ for small } d/R \end{aligned} \quad \dots\dots(11)$$

and

$$\begin{aligned} H_d^0 &= H_0^0 \left[ \left(1 + \frac{3d}{R}\right) \left(1 - \frac{5d\rho_s}{Rk\rho_m}\right) - \frac{10\rho_s}{k\rho_m} \frac{R}{d} \right] \\ &= H_0^0 [1 + 3d/R - 15\rho_s/k\rho_m(d/R)] \text{ for small } d/R, \end{aligned} \quad \dots\dots(12)$$

which is the formula given by Chapman (Chapman and Runcorn 1948). Thus  $H^0$  decreases under land on the Earth according to the formula

$$H_d^0 = H_0^0 [1 - 6.5d/R] \text{ assuming } \rho_s = 3,$$

and under sea according to the formula

$$H_d^0 = H_0^0 [1 - 0.2d/R].$$

If  $g(a)$  is appreciably different from 1 this should be detectable experimentally and might be of importance in explaining relation (1).

The variation in  $H^\theta$  and  $H^r$  within the Earth may be computed from formulae (8) and (9) using the density distribution inside the Earth known from seismological data. In figure 1 the density distribution is taken from the mean of the two

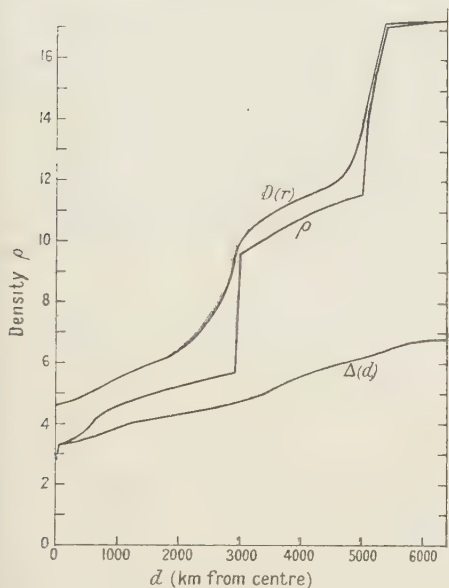
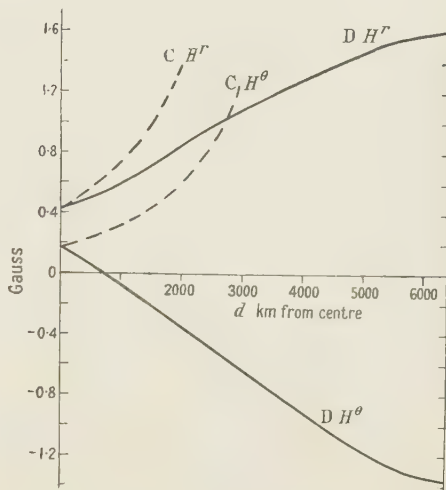


Figure 1. Variation of densities within the Earth.



C=Core theory. D=Distributed theory.

Figure 2. Variation of  $H^r$  and  $H^\theta$  within the Earth for  $H_0^\theta=0.18$  gauss;  $H_0^r=0.42$  gauss.

sets given by Bullen (1947, p. 218). In formulae (8) and (9),  $g(a)$  is taken equal to 1 for simplicity. The results are plotted in figure 2. It will be seen that  $H^\theta$  reverses at a depth of about 700 miles below the surface.

#### § 7. A PROPOSED FURTHER INVESTIGATION OF MASS AS VIRTUAL CURRENT FLOW

If the measurements of the Earth's field at depth finally give a positive result in favour of a distributed theory such as Blackett's, it is important to make further investigations as to the magnetic effect of the matter in the surface shell S.

The boundary condition selected to derive the variation of depth formula from relation (1) implies that the shell must resemble a flow of electric current, and it is important to decide if this is so. Consider an elementary spherical shell: we have shown in § 5 that there is a discontinuity of potential at the shell—this implies that the latter is equivalent to a magnetic shell of moment  $M$  per unit area where

$$4\pi M = (4G^{\frac{1}{2}}/3\mathbf{c})\pi\beta\omega\rho a^2 da \cos\theta + (16G^{\frac{1}{2}}/3\mathbf{c})\pi\beta\omega\rho a^2 da \cos\theta,$$

$$M = \beta(G^{\frac{1}{2}}/\mathbf{c})\omega\rho a^2 \cos\theta da.$$

Suppose each ring of matter in the shell is equivalent to a magnetic shell of strength  $m$  per unit cross-section of ring (Chapman and Bartels 1940, chap. 17). Then the shell may be taken over the cap of the shell on the side remote from the north pole and bounded by the ring at co-latitude  $\theta$ .



Hence the moment per unit area  $M = \int_0^\theta mad \, d\theta$ , and

$$m = -\beta G^{\frac{1}{2}} \omega \rho a \sin \theta / c = -\beta G^{\frac{1}{2}} \rho v / c \quad \dots\dots(13)$$

is the peripheral velocity of the ring.

This is equivalent to H. A. Wilson's hypothesis that a mass element  $m$  gm. when moving with a velocity  $v$  gives at a distance  $r$  a magnetic field

$$H = -\beta(G^{\frac{1}{2}}m/cr^3)\mathbf{v} \wedge \mathbf{r}$$

which he postulated to explain a relation similar to (1).

Wilson (1923) disproved this hypothesis by experiment for linear motion and Blackett (1947) showed that it was untenable on theoretical grounds. However, Blackett suggests that by replacing  $v$  by  $\omega \wedge R$  it may be possible to retain Wilson's hypothesis for rotational motion but not for translational motion (cf. equation (13)).

In any case if the boundary condition selected in §3 which leads to the derivation of equations (8) and (9) is correct we should expect a large and sufficiently long mountain range or deep gorge running E-W to produce a magnetic field of a similar type to that of a linear current. A calculation based on equation (12) using the value of  $\beta$  for the Earth given in table 1 shows that a gorge 4000 ft. (1.3 km.) deep and 3 km. wide will produce a peak field of about  $13\gamma$  at its edge (figure 3).

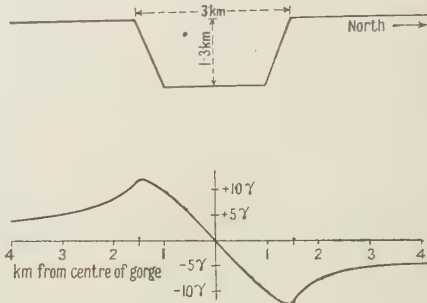


Figure 3. Magnetic effect of gorges on vertical component of full intensity.

In the Northern Hemisphere the vertical component of the Earth's field would be increased by  $13\gamma$  on the south side of the gorge and decreased by  $13\gamma$  on the north side. The effect will fall off inversely as the distance from the centre of the gorge. To make such an experiment with success the rock round the gorge would have to be of low susceptibility (about  $10^{-5}$  gauss) and the strata should lie horizontal. This would exclude most natural features except those gorges formed by erosion in sedimentary rock. It might well be that airborne magnetometers would be very useful in investigations of this effect.

#### ACKNOWLEDGMENTS

The author is indebted to Professor L. Rosenfeld for initial checking of the calculations, to Professors E. C. Bullard and S. Chapman for valuable discussion, to the latter for contributing an Appendix to this paper and to Professor P. M. S. Blackett for much encouragement and help.

#### REFERENCES

- BLACKETT, P. M. S., 1947, *Nature, Lond.*, **159**, 658.  
 BULLARD, E. C., unpublished.  
 BULLEN, K. E., 1947, *Introduction to the Theory of Seismology* (Cambridge : University Press).  
 CHAPMAN, S., 1948, *Nature, Lond.*, **161**, 462.  
 CHAPMAN, S., and BARTELS, J., 1940, *Geomagnetism* (Oxford : Clarendon Press).

- CHAPMAN, S., and RUNCORN, S. K., 1948, *Nature, Lond.*, **161**, 52.  
 ELSASSER, W. M., 1939, *Phys. Rev.*, **55**, 489 ; 1941, *Ibid.*, **60**, 876.  
 FLEMING, J. A. (Ed.), 1940, *Terrestrial Magnetism and Electricity* (London and New York : McGraw Hill).  
 FRENKEL, J., 1945, *C.R. Acad. Sci. U.S.S.R.*, **49**, 98.  
 HAALCK, H., 1937, *Z. Phys.*, **105**, 81 ; 1938, *Gerlands Beitr. Geophys.*, **52**, 243.  
 HALES, A. L., and GOUGH, D. I., 1947, *Nature, Lond.*, **160**, 746.  
 SCHLOMKA, T., 1933, *Gerlands Beitr. Geophys.*, **38**, 357.  
 SCHUSTER, A., 1912, *Proc. Phys. Soc.*, **24**, 121.  
 STRATTON, J. A., 1941, *Electromagnetic Theory* (London and New York : McGraw Hill).  
 SUTHERLAND, W., 1900, *Terr. Magn. Atmos. Elect.*, **5**, 73 ; 1903, *Ibid.*, **8**, 49.  
 WILSON, H. A., 1923, *Proc. Roy. Soc. A*, **104**, 451.

## APPENDIX

By SYDNEY CHAPMAN

Mr. Runcorn has kindly invited me to append my deduction of the formula quoted in his § 6 and by Chapman and Runcorn (1948, equation (3)); this is briefly as follows. I hope to communicate to *Annales de Géophysique* a fuller treatment of this and other questions related to the Blackett hypothesis of the earth's magnetic field.

(a) From general electromagnetic theory we know that the field of magnetic induction (this and the field of magnetic intensity will here be denoted by  $b$  and  $h$ , and  $b = h + 4\pi I$ ) for a body magnetized with uniform intensity  $I$  is the same as the field of magnetic intensity  $H$  of a distribution of current of surface intensity  $I \wedge n$  over the boundary of the body (here  $n$  denotes the outward normal unit vector at the surface point considered, and  $\wedge$  denotes the vector product sign).

For such a body of spherical form, with radius  $R$ , the field  $b$  at inside points is  $(8/3)\pi I$ , and at outside points it is  $-\text{grad } V$ , where  $V = M \cos \theta / r^2$  at a point whose polar coordinates are  $r, \theta$ , where  $M = (4/3)\pi R^3 I$ . This is therefore the field  $H$  of a surface current of intensity  $I \sin \theta$  flowing round the parallels of magnetic latitude.

(b) Blackett in effect supposes that, in a solid of revolution a rotatory flow of mass has the magnetic effect of a proportional electric current flow. This current flow, in a sphere of radius  $a$  rotating with angular speed  $\omega$ , and with density  $\rho$  dependent only on  $R$ , is  $K\rho\omega R \sin \theta$  at radius  $R$ , where  $K$  is a constant written by Blackett in the form  $\beta G^{3/2}/2c$ .

Such a volume current distribution can be supposed subdivided into thin shells (of radii  $R, R + dR$ ). Such a shell can be treated as a surface current flow of density  $K\rho\omega R \sin \theta dR$  over the sphere of radius  $R$ ; its magnetic field  $dh$  is the same as the  $b$  field of this sphere uniformly magnetized with intensity  $I = K\rho\omega R dR$ , parallel to the axis of rotation. To obtain the whole field  $H$  it is necessary to integrate the  $b$  fields for all such contributions. At a point at radius  $r$  within the sphere,  $H$  is the integral of  $b$  according to the formula  $(8/3)\pi I$  for all the shells of radius  $0 \leq R \leq r$ , and according to the second formula in (a), for  $r \leq R \leq a$ .

It is convenient to express the results by the vertical (radial) and horizontal components  $H^r, H^\theta$ , as follows:

$$H^r = (8/3)\pi K\omega \cos \theta \left\{ \int_0^r \rho R^4 dR / r^3 + \int_r^a \rho R dR \right\},$$

$$H^\theta = (4/3)\pi K\omega \sin \theta \left\{ \int_0^r \rho R^4 dR / r^3 - 2 \int_r^a \rho R dR \right\}.$$

(c) At the surface  $r=a$  (here indicated by the suffix 0) these components have the values indicated by

$$H_0^r = 2H_0^\theta \cot \theta,$$

$$H_0^\theta = (4/3)\pi K\omega \sin \theta \int_0^a \rho R^4 dR / a^3 = \frac{1}{2}K\omega(I/a^3) \sin \theta,$$

where  $I$  denotes the moment of inertia of the sphere. Taking this moment to be  $kI_0$ , where  $I_0$  denotes the moment ( $8\pi ka^5\rho_m/15$ ) for a uniform sphere of radius  $a$  and the same mean density  $\rho_m$ ,

$$H_0^\theta = (4/15)\pi kK\omega a^2\rho_m \sin \theta.$$

(d) The rates of radial variation of  $H^r$  and  $H^\theta$  are obtained by differentiating the expressions given in (b) with respect to  $r$ . The results are specially simple at the surface  $r=a$  (again indicated by suffix 0), as follows:

$$\begin{aligned} \left(\frac{dH^r}{dr}\right)_0 &= -\frac{8\pi K\omega \cos \theta}{a^4} \int_0^a \rho R^4 dR = -3 \frac{H_0^r}{a} \\ \left(\frac{dH^\theta}{dr}\right)_0 &= \frac{4}{3} \pi K\omega \sin \theta \left\{ 3\rho_s a - \frac{3}{a^4} \int_0^a \rho R^4 dR \right\} \\ &= -3 \frac{H_0^\theta}{a} \left( \frac{5\rho_s}{k\rho_m} - 1 \right), \end{aligned}$$

where  $\rho_s$  denotes the surface density.

The first of these two equations indicates that at the surface the rate of variation of the vertical component with respect to radius (or depth) is the same as for a core theory; the second equation is equivalent to my equation (3) in the article by Chapman and Runcorn (1947).

## A Numerical Fourier-analysis Method for the Correction of Widths and Shapes of Lines on X-ray Powder Photographs

By A. R. STOKES

Wheatstone Physics Laboratory, King's College, University of London\*

*Communicated by J. T. Randall ; MS. received 15 April 1948*

**ABSTRACT.** A method is derived, using Fourier analysis, for finding the corrected distribution of intensity across an x-ray diffraction line, and the procedure is illustrated by a numerical example. The method may also be of use in spectrum analysis and statistical problems.

### § 1. INTRODUCTION

A STUDY of the widths of the lines on x-ray (Debye-Scherrer) powder photographs can yield valuable information as to the particle size, state of strain, or "mistake structure" in a specimen (see for instance Jones (1938), Edwards, Lipson and Wilson (1942), Megaw and Stokes (1945), and Birks and Friedman (1946)). But the line widths obtained by photometry

\* An account of work done mainly at the Cavendish Laboratory, Cambridge.



are not of much value until allowance has been made for the additional broadening inherent in the method of photography, due mainly to the specimen size and to the slight spread of wavelengths (including the  $K\alpha$  doublet) in the incident radiation. This "instrumental" broadening is very seldom negligible.

Kochendörfer (1937) and Jones (1938) have described corrections for instrumental broadening; the former calculated the broadening to be expected from the apparatus while the latter observed the broadening actually obtained from the apparatus when a specimen of powdered metal, having strain-free crystals large enough to contribute no broadening to the lines, was used.

Both these methods, however, involve some assumption as to the intensity distribution across the lines which the specimen would give if instrumental broadening were absent. Kochendörfer used a theoretical line shape derived by Laue, which is not necessarily appropriate in all cases; in Jones' method a certain amount of trial and error is needed before the right line profile can be obtained. It seems desirable, therefore, to devise a direct method whereby the line profile which would be obtained in the absence of any instrumental broadening can be deduced from the experimental line profiles. Further, the methods referred to above give only the corrected line *breadths*, whereas useful information may often be obtained from line *shapes*. The breadth of a line (whether it be the half-peak width, the "integral breadth", or some other measure) is in fact only *one* parameter (though often a very valuable one) defining the distribution of x-ray intensity across the line.

## §2. MATHEMATICAL BASIS OF THE METHOD

The observed distribution of x-ray intensity across a line is related to the distribution due to instrumental broadening and that due to small particle size etc., in the specimen, by the equation

$$h(x) = \int_{-\infty}^{\infty} f(y)g(x-y)dy \quad \dots\dots(1)$$

where  $f(x)$  is the intensity which would be recorded, at a point distance  $x$  measured along the film from some fixed point, in the absence of instrumental broadening,  $g(x)$  is similarly the intensity recorded at  $x$  from a specimen giving negligible broadening in itself, so that all broadening is instrumental, and  $h(x)$  is the intensity actually observed, when the broadening is due to both causes. This relation is proved by Jones (1938). The functions  $h(x)$  and  $g(x)$  are known (being given in numerical form from intensity measurements) while  $f(x)$  is an unknown function, which Jones found by trial and error, but which we want to deduce from  $g$  and  $h$ .

In practice we generally measure  $g$  and  $h$  at discrete intervals (say at every 0.1 mm. of film) instead of as continuous functions, and it is therefore convenient to replace the integral in (1) by a summation

$$h(x) = \Sigma f(y)g(x-y)\delta y \quad \dots\dots(2)$$

where  $\delta y = 0.1$  mm.: this is very nearly equivalent to the integral form (1). We see that the relation in this form constitutes a set of linear simultaneous equations, one equation for each value of  $x$  for which  $h(x)$  is measured, with the values of  $f(x)$  as the unknowns. As there are in general about 20 to 50 of these equations, it would be too laborious to solve them by the ordinary method of

elimination. An iteration method (e.g. Whittaker and Robinson 1944 a) might be applied, but as Shull (1946) has pointed out, one can use Fourier analysis to obtain the solution. We take a range of values of  $x$  from  $-a/2$  to  $+a/2$  outside which  $g(x)$  and  $h(x)$  are zero (that is, outside which the intensity can be considered to have fallen to its background value), and we obtain Fourier series for  $g(x)$ ,  $h(x)$  and  $f(x)$  in this range :

$$\left. \begin{aligned} f(x) &= \sum_{-\infty}^{\infty} F(t) \exp(-2\pi ixt/a) \\ g(x) &= \sum G(t) \exp(-2\pi ixt/a) \\ h(x) &= \sum H(t) \exp(-2\pi ixt/a) \end{aligned} \right\} \dots\dots(3)$$

where  $t=0, \pm 1, \pm 2$  etc., and  $F, G$ , and  $H$ , are complex coefficients whose values are given by equations

$$F(t) = \frac{1}{a} \int_{-a/2}^{a/2} f(x) \cdot \exp(2\pi ixt/a) dx \text{ etc.} \dots\dots(4)$$

We now substitute the expressions for  $f$  and  $g$  given by equation (3) into equation (1), and alter the limits of integration to  $-a/2$  and  $+a/2$  (for  $f$  and  $g$  are zero outside these limits) and we obtain

$$\begin{aligned} h(x) &= \int_{-a/2}^{a/2} f(y) g(x-y) dy \\ &= \int_t \sum_t \sum_{t'} F(t) G(t') \exp(-2\pi iyt/a) \exp\{-2\pi i(x-y)t'/a\} dy \\ &= \sum_t \sum_{t'} F(t) G(t') \int_{-a/2}^{a/2} \exp\{-2\pi iy(t-t')/a\} \exp(-2\pi ixt'/a) dy. \end{aligned}$$

The integral of  $\exp\{-2\pi iy(t-t')/a\}$  is zero if  $t \neq t'$  and equal to  $a$  if  $t=t'$ ; thus the only terms left in the summation are those with  $t=t'$ , and the series reduces to

$$h(x) = a \sum_t F(t) G(t) \exp\{-2\pi ixt/a\}.$$

Comparing this with the third equation of (3), we obtain

$$H(t) = a F(t) G(t)$$

or

$$F(t) = H(t)/aG(t). \dots\dots(5)$$

By substituting this in the first of equations (3) we obtain

$$f(x) = \sum_t \frac{H(t)}{aG(t)} \exp\{(-2\pi ixt)/a\}. \dots\dots(6)$$

In practice we omit the factor  $1/a$  since it is a constant and does not affect the shape of the resulting curve, but only its height. We can therefore express the procedure for finding  $f(x)$  as follows. Find the Fourier components of the distributions of intensity  $h(x)$  and  $g(x)$  of the observed broad line and sharp line respectively : divide each Fourier component of  $h(x)$  by the corresponding component of  $g(x)$ , and use the resulting quotients in a Fourier synthesis to find  $f(x)$ . It should perhaps be pointed out that this procedure eliminates broadening due to  $K\alpha$  doubling as well as other forms of broadening; there is no need to deal separately with  $K\alpha$  doubling as in Jones' method. The Fourier components are, of course,

complex numbers, and the method of dealing numerically with these complex quantities will be explained subsequently. The expression (1) for  $h$  in terms of  $f$  and  $g$  is known to mathematicians as the "fold" of  $f$  and  $g$ ; it seems therefore appropriate to call  $f$  the "unfold" of  $h$  by  $g$ , and to call the process by which  $f$  is obtained, "unfolding".

Shull (1946) has used equation (6) to show that, if  $h(x)$  and  $g(x)$  are fitted to certain functions made up of Gaussian error functions, then the unfold can be found in terms of similar functions, and its breadth can be found in terms of certain parameters of the original functions.

This procedure evidently gives us a fairly rapid method of obtaining reasonably reliable values of the corrected breadths, but it seems somewhat undesirable to fit the observed intensity curves to Gaussian error functions, partly because in so doing one introduces an element of arbitrary rigidity into the treatment which may lead to a deceptive appearance of certainty about the results, and partly because theory does not give functions of this form for the intensity distributions, at any rate from small crystals (Stokes and Wilson 1942, 1944). Also it appears that difficulties would be encountered when  $K\alpha$  doubling causes appreciable asymmetry in the line profiles, since the functions that Shull uses are all symmetrical. In view of the existence of Lipson-Beevers strips (Lipson and Beevers 1936) and other devices for enabling Fourier analyses to be done rapidly (e.g. Hägg and Laurent 1946) it is not a very formidable task to evaluate the functions  $f(x)$  numerically from equations (4) and (6).

### § 3. EXPERIMENTAL MATERIAL AND METHOD OF COMPUTATION

The method was applied to investigate the shapes and breadths of reflections from cold-worked copper. A specimen of copper filings in a sealed thin-walled silica tube was photographed in a high-temperature x-ray powder camera at room temperature; the temperature was then raised to about 400° C. for an hour to anneal the copper filings, and the specimen was again photographed at room temperature, giving a set of lines whose breadths were due almost entirely to instrumental broadening. The photographs were microphotometered, and the functions  $h(x)$  and  $g(x)$  were obtained, for each line, from the microphotometer readings for the respective photographs, by subtracting the background intensity from the observed readings of intensity. The microphotometer gave readings of density at intervals of 0.1 mm. Corrections were made where necessary for any departure from a linear density-intensity relation, as shown by a step-wedge calibration.

The Fourier components  $H(t)$  and  $G(t)$  of the functions  $h(x)$  and  $g(x)$  were obtained by the use of Lipson-Beevers strips. On these are tabulated values of  $A \cos nx$  and  $B \sin nx$  for  $A$  and  $B$  equal to integers from  $-99$  to  $+99$ ,  $n=0, 1, 2, \dots, 20$ , and  $x=0^\circ, 6^\circ, 12^\circ, \dots, 90^\circ$ , or  $0, 1, 2, \dots, 15 \times 2\pi/60$  radians. Thus they facilitate the evaluation of sums like  $\sum_x g(x) \cos 2\pi xt/60$  and  $\sum_x g(x) \sin 2\pi xt/60$ , where  $g(x)$  is given at  $x=0, \pm 1, \pm 2, \dots$  (in arbitrary units of length) and  $t=0, 1, 2, \dots$

If  $G_r(t)$  and  $G_i(t)$  are the real and imaginary parts of  $G(t)$ , then from equation (4)

$$G_r(t) = \frac{1}{a} \int_{-a/2}^{a/2} g(x) \cos(2\pi xt/a) dx \quad \text{and} \quad G_i(t) = \frac{1}{a} \int_{-a/2}^{a/2} g(x) \sin(2\pi xt/a) dx.$$



To evaluate these integrals numerically we divide the range  $-a/2$  to  $a/2$  into 60 intervals, and sum the integrands at these intervals. For convenience we let our unit of length be such that  $a = 60$  units, so that  $x$  is taken at unit intervals.

Then

$$G_r(t) = \frac{1}{60} \sum_{-30}^{30} g(x) \cos 2\pi xt/60, \quad \text{and} \quad G_i(t) = \frac{1}{60} \sum_{-30}^{30} g(x) \sin 2\pi xt/60, \quad \dots\dots(7)$$

which may be evaluated by means of Lipson-Beevers strips as described above. The validity of this change from an integral to a sum depends upon whether the intervals chosen are small enough compared with the scale of the detail in the  $g(x)$  curve; we shall return to this point later.

Having obtained  $G_r(t)$ ,  $G_i(t)$ , and similarly  $H_r(t)$ ,  $H_i(t)$ , we now have

$$F(t) = \frac{H(t)}{G(t)} = \frac{H_r(t) + iH_i(t)}{G_r(t) + iG_i(t)} = \frac{(H_r + iH_i) \cdot (G_r - iG_i)}{G_r^2 + G_i^2};$$

hence

$$F_r = \frac{H_r G_r + H_i G_i}{G_r^2 + G_i^2}; \quad F_i = \frac{H_i G_r - H_r G_i}{G_r^2 + G_i^2},$$

from which we can calculate  $F_r(t)$  and  $F_i(t)$ . Alternatively, a complex-number slide-rule \* (Du Mond 1924) might be used.

Finally, we have

$$\begin{aligned} f(x) &= \sum_t F(t) \exp [2\pi ixt/a] \\ &= \sum_t \{F_r(t) + iF_i(t)\} (\cos 2\pi xt/60 - i \sin 2\pi xt/60) \\ &= \sum_t F_r(t) \cos 2\pi xt/60 + \sum_t F_i(t) \sin 2\pi xt/60, \end{aligned}$$

the other terms vanishing since  $F(-t)$  is the conjugate complex of  $F(t)$ , and therefore  $F_r(-t) = F_r(t)$ , and  $F_i(-t) = -F_i(t)$ .

The procedure is illustrated by the process of unfolding one of the lines from the photographs of cold-worked and annealed copper, given in tables 1 to 4.

Table 1.  $h(x)$

$x$	$h(x)$	$x$	$h(x)$	$x$	$h(x)$	$x$	$h(x)$
-20	3	-10	33	0	277	10	29
-19	4	-9	42	1	243	11	26
-18	5	-8	50	2	233	12	21
-17	7	-7	60	3	208	13	18
-16	9	-6	82	4	177	14	16
-15	11	-5	102	5	147	15	14
-14	13	-4	140	6	125	16	12
-13	18	-3	194	7	83	17	10
-12	22	-2	237	8	70	18	8
-11	27	-1	267	9	39	19	7
						20	7

( $x$  in tenth-millimetres.)

Each value of  $h(x)$  as given here was subsequently multiplied by 0.2 for convenience in using Lipson-Beevers strips.

\* The general principle of this slide-rule is that, just as real numbers can be multiplied by the addition of their logarithms plotted on a one-dimensional scale, so complex numbers may be multiplied by the vector addition of their logarithms plotted on a two-dimensional sheet. The logarithms are evaluated from the formula

$$\ln(x + iy) = \frac{1}{2} \ln(x^2 + y^2) + i \tan^{-1}(y/x).$$

The real part of this is plotted as abscissa and the imaginary part as ordinate; division can then be effected by subtracting the vectors found by joining points on this plot to the origin.

Table 2.  $g(x)$ 

$x$	$g(x)$	$x$	$g(x)$	$x$	$g(x)$	$x$	$g(x)$
-13	0	-7	9	0	475	7	60
-12	0	-6	12	1	371	8	19
-11	0	-5	17	2	174	9	12
-10	2	-4	21	3	151	10	8
-9	4	-3	51	4	227	11	5
-8	6	-2	161	5	260	12	3
		-1	369	6	160	13	1

(x in tenth-millimetres.)

Each value of  $g(x)$  as given here was subsequently multiplied by 0.1 for convenience in using Lipson-Beevers strips.

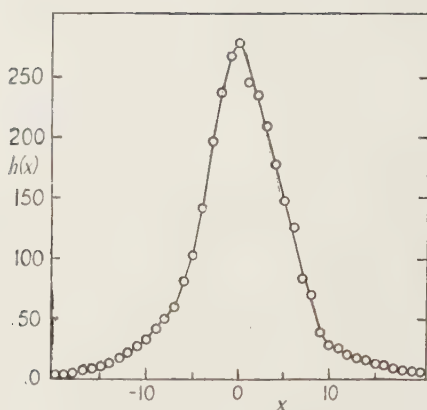
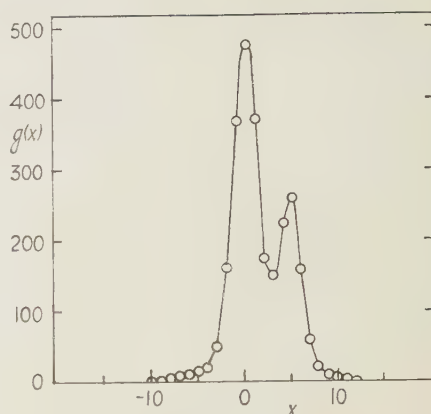
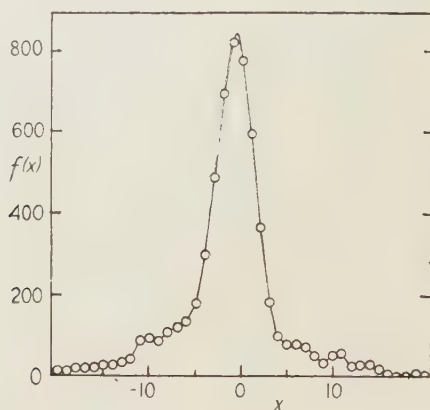
Table 3. Fourier components of  $h(x)$ ,  $g(x)$ , and  $f(x)$ 

$t$	$H_r(t)$	$H_i(t)$	$G_r(t)$	$G_i(t)$	$F_r(t)$	$F_i(t)$
0	619	0	259	0	2.40	0
1	517	16	243	37	2.10	-0.25
2	334	30	203	63	1.55	-0.35
3	205	30	152	70	1.20	-0.35
4	125	22	102	61	1.00	-0.38
5	63	7	69	36	0.75	-0.30
6	33	-10	53	7	0.60	-0.30
7	18	-22	50	-18	0.48	-0.28
8	10	-23	55	-33	0.35	-0.25
9	12	-17	61	-37	0.28	-0.18
10	6	-11	67	-32	0.15	-0.10
11	2	-5	66	-21	0.05	-0.05
12	2	-4	62	-9	0.05	-0.05
13	-4	-5	51	1	—	—
14	-2	-7	39	8	—	—
15			24	10		
16			14	7		
17			7	3		
18			5	2		
19			2	0		
20			4	0		

Each value of  $F_r(t)$  and  $F_i(t)$  was subsequently multiplied by 40 for convenience in using Lipson-Beevers strips.

Table 4.  $f(x)$ , from synthesis of  $F_r(t)$  and  $F_i(t)$ 

$x$	$f(x)$	$x$	$f(x)$	$x$	$f(x)$	$x$	$f(x)$
-20	15	-10	93	0	780	10	53
-19	13	-9	85	1	599	11	59
-18	18	-8	107	2	369	12	26
-17	19	-7	121	3	185	13	29
-16	23	-6	135	4	100	14	29
-15	28	-5	178	5	80	15	20
-14	29	-4	298	6	79	16	7
-13	35	-3	489	7	73	17	1
-12	40	-2	697	8	53	18	4
-11	87	-1	821	9	33	19	9
						20	7

Figure 1.  $h(x)$ .Figure 2.  $g(x)$ .Figure 3.  $f(x)$ .

The shapes of the curves  $h(x)$ ,  $g(x)$ , and  $f(x)$  are shown in figures 1, 2 and 3.

We can investigate the validity of replacing the integrals in (4) by summations in (7) as follows. We have  $g(x) = \sum_i G(t) \exp(-2\pi ixt/a)$ , by (3), and we wish to

find how well  $G'(t) \equiv a^{-1} \sum_{-a/2}^{a/2} g(x) \exp(2\pi ixt/a)$  approximates to

$$G(t) \equiv a^{-1} \int_{-a/2}^{a/2} g(x) \exp(2\pi ixt/a) dx,$$

$x$  being taken at unit intervals in the summation. By (3) we have

$$\begin{aligned} G'(t) &= a^{-1} \sum_{x, t'} G(t') \exp(-2\pi ixt'/a) \exp(2\pi ixt/a) \\ &= a^{-1} \sum_{t'} G(t') \left[ \sum_x \exp(2\pi ix(t-t')/a) \right]. \end{aligned}$$

The sum within the square brackets is the sum of a geometric series, which is zero if  $(t-t')/a$  is not an integer, and equal to  $a$  if  $(t-t')/a$  is an integer. Thus  $G'(t)$  is equal to the sum of all the values of  $G(t')$  for  $t-t'$  equal to an integral multiple of  $a$ , that is,

$$\begin{aligned} G'(t) &= G(t) + G(t+a) + G(t+2a) + \dots \\ &\quad + G(t-a) + G(t-2a) + \dots \end{aligned} \quad \dots\dots\dots (8)$$



We see from the numerical example that  $H$  and  $G$  fall to zero (apart from small fluctuations due to experimental error) as  $t$  increases. Now if  $G(t)$  is zero for *all* values of  $t$  outside the range  $-a/2$  to  $+a/2$ , then not more than one term of the series in equation (8) can be non-zero at once, and therefore  $G'(t) = G(t)$  in the range  $-a/2 < t < a/2$ .

The condition that the summations (7) should be good representations of the Fourier components is therefore that  $G(t)$  should fall sensibly to zero for values of  $t$  outside a range not larger than the range  $-a/2$  to  $+a/2$ . In the numerical example above,  $H(t)$  and  $G(t)$  become nearly zero at  $t=12$  and  $t=18$  respectively. Since  $a=60$ , these values of  $t$  fall within the required range,  $-30$  to  $+30$ , and therefore the values obtained by summation are the same as the true values which would be obtained by integration over the whole range of  $t$  in which we are interested. If this were not so, we should have to use a greater number of divisions. From the above reasoning, the number of divisions must always exceed twice the value of  $t$  for the Fourier component of lowest frequency which is sensibly zero.

#### § 4. EFFECT OF EXPERIMENTAL ERRORS

In any set of microphotometry readings the measurements of density are subject to errors. We shall investigate here how the errors in the unfolded curves depend on those of the observed curves.

We assume (a) that the probable error of any one photometer reading is the same as that of any other, and (b) that the errors of any two readings, even adjacent ones, are independent. This may be taken as true when the grain-size of the film (which is the main cause of error in microphotometry) is small compared with the 0.1 mm. distance between successive readings.

The probable errors in the Fourier components  $G(t)$  and  $H(t)$  can be obtained as follows. If  $\Delta g(x)$  is the error in  $g(x)$ , then the error in  $G(t)$  is

$$\Delta G(t) = a^{-1} \sum_x \Delta g(x) \exp(2\pi ixt)$$

and the probable error of  $G(t)$  can be assessed from the mean square value of the modulus of the error :

$$\begin{aligned} |\overline{\Delta G(t)}|^2 &= \overline{\Delta G(t) \Delta G(t)^*} \\ &= a^{-2} \sum_x \Delta g(x) \exp(2\pi ixt/a) \sum_x \Delta g(x) \exp(-2\pi ixt/a) \\ &= a^{-2} \sum_{x_1, x_2} \overline{\Delta g(x_1) \Delta g(x_2)} \exp(2\pi i(x_1 - x_2)t/a), \end{aligned}$$

the "bar" above an expression denoting that the mean value of that expression is to be taken. But by our assumptions (a) and (b) above  $\overline{\Delta g(x_1) \Delta g(x_2)} = 0$  for  $x_1$  and  $x_2$  different, and  $\overline{\Delta g(x_1)^2} = \text{const.} = \Delta^2$ , say. Hence

$$|\overline{\Delta G(t)}|^2 = a^{-2} \sum_x \Delta g(x)^2 = a^{-2} \cdot a \Delta^2 = \Delta^2/a$$

(Whittaker and Robinson 1944 b), since  $a$  is the number of readings over which the summation is taken. The mean square error in  $F(t)$  is given by

$$\begin{aligned} |\overline{\Delta F(t)}|^2 &= |\overline{\Delta(H/G)}|^2 = \overline{(G\Delta H - H\Delta G)^2/G^2} \\ &= (G^2\overline{\Delta H^2} + H^2\overline{\Delta G^2})/G^4 = \{(G^2 + H^2)/G^4\} \cdot (\Delta^2/a). \end{aligned}$$

Since  $G^4$  occurs in the denominator of this expression, the probable error of  $F(t)$  increases rapidly as  $G(t)$  becomes smaller. Reference to the values of  $G(t)$  given in table 2 will show that  $|G(t)|$  decreases as  $t$  increases; hence the error in  $F(t)$  will increase as  $t$  increases. This increase is not serious, however, provided  $H(t)$  has fallen sensibly to zero before  $G(t)$  has decreased very much from its maximum value, so that terms in which  $G(t)$  is smaller may be neglected in the final synthesis. In the example given, the synthesis has been taken only to the  $t = 12$  term for this reason.

The effect of these errors in  $F(t)$  will be to make the values of  $F$  for large values of  $t$  more uncertain than those for  $t$  small. These erroneous values of  $F$  for large  $t$  will introduce spurious sinusoidal components of short wavelength into the final synthesis, so that local variations will be of little significance: the large-scale picture of  $f(x)$  will be more or less correct, but the details will be unreliable.

In general a broad line gives Fourier components falling off more rapidly with increasing  $t$  than those for a narrow line. (This is illustrated by the values of  $H(t)$  and  $G(t)$  in tables 1 and 2.) We want  $H(t)$  to fall off rapidly to zero compared with  $G(t)$  so that we can neglect components which are divided by small values of  $G(t)$  and are therefore subject to large errors. Therefore we want  $g(x)$  to be narrow compared with  $h(x)$ . Thus we reach quite generally the conclusion (already noted by various writers in particular cases) that the standardizing lines, which give the "instrumental" broadening, must be as narrow as possible compared with the broadened lines of the specimen under examination, if we are to deduce reliable values for the corrected breadths and shapes of the lines.

#### § 5. A CHECK ON THE NUMERICAL VALUES OF $f(x)$

The numerical values of  $f(x)$  were checked by folding  $f(x)$  and  $g(x)$  numerically and comparing the result with  $h(x)$ . This may be done readily by taking the sum of products  $f(y)g(x-y)$ , as in equation (2); the values thus obtained were divided by 4800 to allow for the various factors introduced during the unfolding process and for the fact that the factor  $1/a$  was omitted from equation (6) as

Table 5. Fold of  $f(x)$  and  $g(x)$ , for comparison with  $h(x)$

$x$	Fold	$h(x)$	$x$	Fold	$h(x)$	$x$	Fold	$h(x)$
-20	3	3	-6	79	82	8	62	70
-19	5	4	-5	103	102	9	45	39
-18	6	5	-4	140	140	10	37	29
-17	7	7	-3	191	194	11	32	26
-16	9	9	-2	236	237	12	26	21
-15	12	11	-1	267	267	13	18	18
-14	14	13	0	272	277	14	16	16
-13	17	18	1	253	243	15	13	14
-12	21	22	2	227	233	16	9	12
-11	32	27	3	201	208	17	8	10
-10	38	33	4	177	177	18	3	8
-9	45	42	5	152	147	19	2	7
-8	51	50	6	120	125	20	1	7
-7	62	60	7	89	83			

explained in the text. Values of the fold thus obtained are given in table 5, with the original values of  $h(x)$  for comparison. The values agree for the most part to within 2-3% of the largest value of  $h(x)$ ; this is about the accuracy to be expected, since each of the several processes involved in unfolding, and the process of folding, have been carried out with an accuracy not exceeding about 1%.

## § 6. CONCLUSION

From the numerical example we see that, given a rapid means of summing Fourier series, the unfolding process can be applied to give a purely deductive method of obtaining corrected line shapes of x-ray diffraction lines. The same process might well have other applications, such as the deduction of corrected line widths in optical spectroscopy, and in statistical analysis of fluctuations in a case in which we know the frequency distribution of fluctuations due to a cause A acting alone, and due to causes A and B acting simultaneously, and wish to find the distribution for B alone (Whittaker and Robinson 1944 c).

## ACKNOWLEDGMENTS

My thanks are due to Dr. H. Lipson and to Mr. M. A. Jaswon for several helpful discussions.

## REFERENCES

- BIRKS, L. S., and FRIEDMAN, H., 1946, *J. Appl. Phys.*, **17**, 687.  
 DU MOND, J. W. M., 1924, Paper presented at the Pacific Coast Convention of the A.I.E.E., Pasadena, California, U.S.A., 13-17 Oct. 1924.  
 EDWARDS, O. S., LIPSON, H., and WILSON, A. J. C., 1942, *Proc. Roy. Soc. A*, **180**, 268, 277.  
 HÄGG, G., and LAURENT, T., 1946, *J. Sci. Instrum.*, **23**, 155. (References to several other Fourier-analysis machines given.)  
 JONES, F. W., 1938, *Proc. Roy. Soc. A*, **166**, 16.  
 KOCHENDÖRFER, A., 1937, *Z. Kristallogr.*, **97**, 469.  
 LIPSON H., and BEEVERS, C. A., 1936, *Proc. Phys. Soc.*, **48**, 772.  
 MEGAW, H. D., and STOKES, A. R., 1945, *J. Inst. Metals*, **12**, 279.  
 SHULL, C. G., 1946, *Phys. Rev.*, **70**, 679.  
 STOKES, A. R., and WILSON, A. J. C., 1942, *Proc. Camb. Phil. Soc.*, **38**, 313; 1944, *Ibid.*, **40**, 197.  
 WHITTAKER, E. T., and ROBINSON, G., 1944 a, *The Calculus of Observations* (London: Blackie, 4th edn.), p. 255; 1944 b, *Ibid.*, p. 280; 1944 c, *Ibid.*, p. 168.

## LETTERS TO THE EDITOR

A Note on the  $\Delta E$  Effect in Alnico

In this short communication we wish to draw attention to some experiments which have recently been made on the change in Young's modulus of a ferromagnetic accompanying magnetization, known as the  $\Delta E$  effect. Up to the present, no results have been recorded for the high coercivity alloys, and in this note are given the results of an investigation of one particular permanent magnet material—alnico. The approximate percentage composition of the material was Al 10, Ni 18, Co 12, Cu 6, Fe 54, and specimens were prepared by casting in the form of rods of length 30 cm. and diameter 0.65 cm. Two such rods were available, one as cast or untreated, and the other heat-treated by maintaining it at a temperature of 1250° C. for 20 minutes, allowing it to cool at the rate of about 2° C. per sec., and then annealing it at 600° C. for about two hours, i.e. it was hardened and tempered. These rods were kindly supplied by Dr. K. Hoselitz.

The method used for the measurements, in which the resonant frequencies of longitudinal oscillation of the rods were observed, was the same as that already described by Street (1948). The rods were made to oscillate at their third harmonic at a frequency of approximately 25 kc/s. The maximum magnetic field intensity produced by the solenoid surrounding the specimen was 800 oersteds, and this gave intensities of magnetization of about 700 gauss in both the alnico rods.



It was found for both rods that the value of the resonant frequency when the specimen was magnetized to the maximum available intensity was only slightly greater than the corresponding value for the demagnetized material. Before the change in Young's modulus could be calculated it was necessary to determine the magnetostrictive change in the length of the rod. This was done by observing the system of Newton's rings set up between a plane glass disc attached to one end of the rod and a lens rigidly held near it. The value of the coefficient of magnetostriction for the available change in magnetization was found to be  $+1 \times 10^{-5}$  approximately.

For both specimens the modulus increased steadily with intensity of magnetization and the maximum observed increase was 0.02%. From the form of the ( $I, H$ ) curves it appeared that the specimens were reasonably close to technical saturation for the maximum applied field of 800 oersteds. Thus 0.02% represents a fair approximation to the maximum possible change in Young's modulus of the materials from the demagnetized to the saturated states. The corresponding figures for annealed nickel and cobalt specimens are 7.0 and 0.7% respectively. The values of Young's modulus for the two alnico specimens were equal within the limits of experimental error, the mean value being  $17.0 \times 10^{11}$  dyne/cm<sup>2</sup>.

The decrements of longitudinal oscillations in the rods were determined from observations of the widths of the resonance curves obtained by variation of the frequency of the exciting current. The mean value of the decrement in each case was very small,  $2.5 \times 10^{-4}$  for the untreated specimen; only small variations about this mean were observed. In comparison, Ni and Co show large variations in decrement, the range for Ni being  $10^{-3}$  to  $5 \times 10^{-2}$  and for Co  $2 \times 10^{-4}$  to  $10^{-3}$ . There was some evidence to show that the mean decrement for the heat-treated rod was greater than that for the untreated rod. No great significance can be placed on the latter observation, however, since for such low decrements slight errors in the alignment of the rods within the apparatus may have appreciable influence on the result.

For any ferromagnetic specimen examined by the method used here there are certain ranges of the virgin curve and the hysteresis cycle over which the E.M.F. induced in the detecting coil is practically zero, and this behaviour was observed with the rods of alnico. Starting from the demagnetized state, no appreciable E.M.F. was induced until  $I$  was 100 gauss. For the hysteresis cycle the induced E.M.F. again approached zero over ranges of the intensity of magnetization approximately 200 gauss wide, around the coercive force points. Near these points, where the induced E.M.F. was small, the latter showed a pronounced time-lag in attaining a steady value following any change in the external field. No similar time variations of E.M.F. were observed over other regions of the magnetization curve, and the effect has not been noticed with the large number of other specimens already examined in this laboratory. The magnitude of the time-lag was larger for the untreated alnico specimen than for the heat-treated one. We have found by magnetometer methods that this variation of E.M.F. with time is associated with corresponding time changes in the intensity of magnetization.

It would appear from these results that rods of alnico, and possibly other high coercivity alloys, may be used with advantage in magnetostriction oscillator and filter circuits.

The University, Nottingham.  
26th July, 1948.

R. STREET.  
J. C. WOOLLEY.



# CONSTANT "C.V." VOLTAGE

(TRADE MARK)

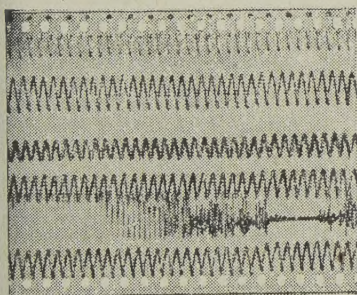
*means constant efficiency*

FOR METER CALIBRATION — PRECISION PHOTOGRAPHY — X-RAY EQUIPMENT — ELECTRONIC DEVICES and ALL LABORATORY AND RESEARCH EQUIPMENT.

Eleven standard sizes, 12.5 VA to 5 kVA, or designed to your requirement. We are particularly interested in problems concerning the incorporation of "C.V.s" as part of your equipment.



**FOSTER TRANSFORMERS & SWITCHGEAR LTD**  
 (INCORPORATING FOSTER ENGINEERING COMPANY) SOUTH WIMBLEDON, LONDON, S.W. 19



13112B

## TRANSIENT EVENTS ARRESTED

The first Avimo Oscillograph Recorder was a specially built Camera designed to provide records of Cathode Ray Traces to a scale which permitted accurate measurement, side by side on continuous film, so that precise relationships could be determined.

Success in this specialised field led to demands for Cameras to record other kinds of transient events, so that within the Avimo range listed below there are, today, instruments to meet nearly any requirement of the Research or Laboratory worker.

The wide experience gained in the course of this development is at your disposal and Avimo engineers will be glad to submit suggestions if you will state your problem.

GROUP	FUNCTION
A. Continuous Recording	For recording oscillograph traces on 35 mm. or 70 mm. film.
B. Single Shot	For use where phenomena are constant.
C. Combined Continuous and Single Shot	Provides the functions of Groups A or B as desired.
D. Drum	For high speed drum recording of high-frequency phenomena on 35 mm. film.
E. Multi-Channel Recorders	With built-in Cathode Ray tubes for continuous recording of up to 15 traces.
F. Instrumentation Ciné	Provides a pictorial record of several variants over a period of time.

There is no reasonable limit to the film speeds which may be provided, and recorders of Groups A, B, C and D may be used in conjunction with any standard oscillograph.

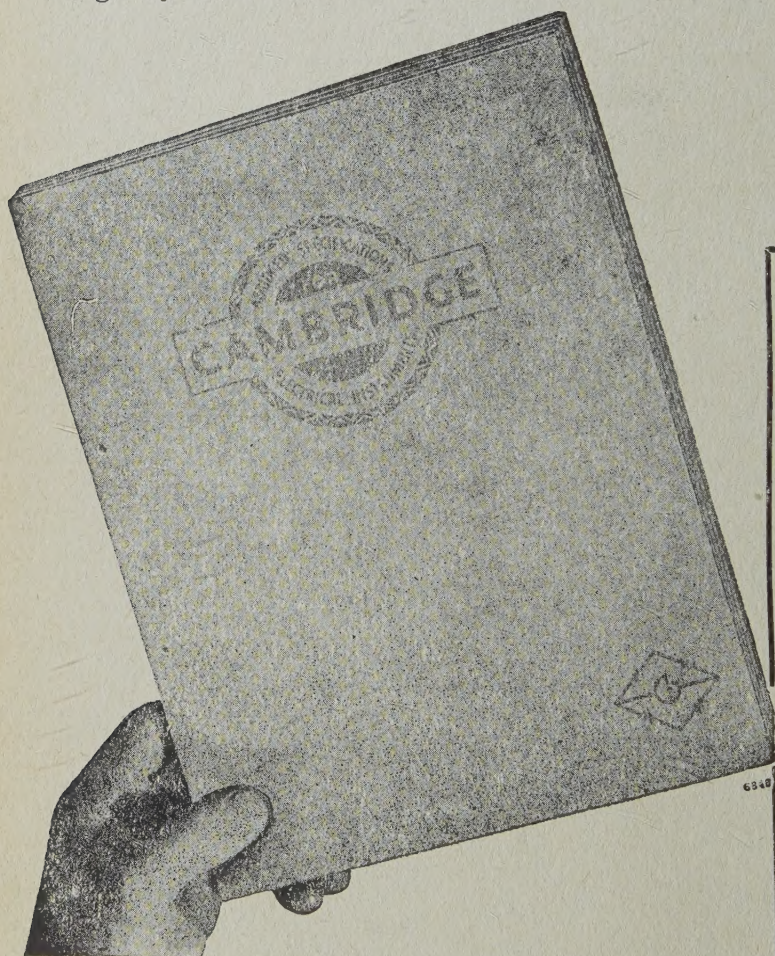


AVIMO LIMITED,  
 TAUNTON, (Som.), ENG.



# CAMBRIDGE ELECTRICAL INSTRUMENTS

THIS COMPREHENSIVE CATALOGUE contains sensitivity data and performance of nearly 400 electrical instruments arranged in convenient tabular form. From the wide range, selection may be made to satisfy practically every electrical measuring or recording requirement, in research, education, or industry. It forms a valuable book of reference, and will be gladly sent free on request.



WRITE FOR  
**LIST 163-L**

D.C. GALVANOMETERS  
A.C. GALVANOMETERS  
VALVE VOLTMETERS  
ELECTROSTATIC  
VOLTMETERS  
ELECTRODYNAMIC AM-  
METERS, MILLIAMMETERS,  
VOLTMETERS, WATT-  
METERS, TEST SETS, etc.  
ELECTROMETERS  
OSCILLOGRAPHS  
POTENTIOMETERS  
BRIDGES  
INDUCTANCES  
RESISTANCES  
CONDENSERS  
A.C. SOURCES  
TEST SETS  
RECORDERS, etc.

**CAMBRIDGE INSTRUMENT COMPANY LTD.**  
13, GROSVENOR PLACE, LONDON, S.W.1.  
WORKS: LONDON & CAMBRIDGE.